Jiaxin Yu

Understanding the impact of stress release on sandstone using sound waves: rock physics, applications and code

NTNU
Norwegian University of
Science and Technology

Jiaxin Yu

Understanding the impact of stress release on sandstone using sound waves: rock physics, applications and code

Thesis for the Degree of Philosophiae Doctor

Trondheim, March 2024

Norwegian University of Science and Technology
Faculty of Engineering
Department of Geoscience and Petroleum

NTNU
Norwegian University of
Science and Technology

ABSTRACT

The acoustic and elastic responses of sandstones vary with changes in effective stress. Laboratory measurements have indicated that among different types of sandstones, velocities and elastic moduli of weakly cemented sandstone show asymmetrically much more sensitivity to effective stress increases than effective stress decreases. Numerous sandstone rock physics models available in the literature are proposed based on the assumption of perfect linear elasticity, which limits the applicability of most models to explain the behavior of weakly cemented sandstone upon effective stress release. Effective stress imposed on a rock is typically defined as the difference between the overburden stress and the pore pressure when the stress coefficient is assumed to be unity. Effective stress release scenarios in practice often involve an increase in pore pressure within reservoir rock due to injection, as well as a reduction in overburden stress caused by uplift and erosion of the rock. However, there is a scarcity of quantitative studies in the literature examining the impact of stress release on various aspects, such as estimating uplift in overconsolidated rock and utilizing 4D seismic monitoring for fluid injection. Compared to high porosity weakly cemented sandstone, unconsolidated sands are more extensively studied. Laboratory experiments and well-log data have demonstrated that the acoustic and petrophysical properties of mechanically compacted overconsolidated sands differ from those of normally consolidated sands. However, there is currently no documented research exploring the similarities and differences between these two types of sandstone in an overconsolidated state. This understanding is crucial both from an academic standpoint and in practical applications.

i

This dissertation addresses the above questions in a sequential manner. Moreover, in order to promote ongoing research on stress release and encourage innovation in rock physics, the models and knowledge gained during the completion of this dissertation have been incorporated into an open-source Python library. This library serves as a valuable resource for the scientific community, providing access to the developed models and facilitating further exploration and advancements in the field of rock physics.

This thesis is submitted to the Norwegian University of Science and Technology (NTNU) for partial fulfillment of the requirements for the degree of Philosophiae Doctor. The Ph.D. thesis is carried out at the Department of Geoscience and Petroleum, NTNU, with Professor Alexey Stovas as a supervisor, Dr. Kenneth Duffaut formerly at NTNU as a supervisor, and Dr. Per Avseth as a cosupervisor. The PhD project was funded by the GAMES (Geophysical and Applied Mathematics for Exploration and Safe Production) consortium at NTNU.

I would like to express my heartfelt gratitude to my former main supervisor, Dr. Kenneth Duffaut, for his invaluable advice and guidance throughout the research process. Working with Kenneth not only helped me navigate through difficulties but also facilitated my personal growth and development. His sincerity, kindness, and willingness to share his authentic self made him the most endearing person I have ever encountered.

I extend my sincere thanks to my co-supervisor, Dr. Per Avseth, who has been a guiding light throughout this adventurous journey. I deeply admire Per's open-mindedness and inclusive nature. Per provided me with crucial support during the initial challenging stages of the project, and together, we overcame numerous obstacles. Our fruitful discussions and his divine inspiration have made a significant contribution to my research and the completion of my Ph.D.

I am also grateful to Professor Alexey Stovas, who took over as my main supervisor after Kenneth returned to Equinor to pursue his passion. Although Alexey's expertise lies not primarily in rock physics, he granted me maximum freedom and support, allowing me to follow my path. Alexey served as a role model, exemplifying the purity of scientific pursuit, which has been a constant motivation for my studies at NTNU.

A special word of thanks goes to Professor Martin Landrø for his unwavering support as a solid pillar. His guidance has been instrumental in shaping my Ph. D study.

"One can travel this world and see nothing. To achieve understanding it is necessary not to see many things, but to look hard at what you do see."

— Giorgio Morandi

Contents

x

CHAPTER 1

GENERAL INTRODUCTION

1.1 Motivations

The acoustic and elastic responses of sandstones exhibit variations in changes in applied effective stress. Recent experimental studies indicate that the elastic properties of weakly cemented sandstone display a notable asymmetric sensitivity, with a more pronounced response to decreases in effective stress compared to increases. In contrast, acoustic properties, such as porosity, do not exhibit such marked differences. Despite the existence of various rock physics models in the literature, few of them address the heightened stress sensitivity observed in the elastic properties of weakly cemented sandstone during stress release. The underlying mechanism responsible for this phenomenon has not been thoroughly explored in the rock physics literature, thereby limiting the applicability of most published models in elucidating the behavior of weakly cemented sandstone under stress release conditions.

Effective stress imposed on a rock is typically defined as the difference between the overburden stress and the pore pressure when the stress coefficient is assumed to be unity. Scenarios involving the release of effective stress are commonly encountered in practice. A representative example is the reduction in effective stress caused by exhumation, which involves a decrease in overburden stress due to the uplift and erosion of the rock. An intriguing question arises regarding how stress

release influences the estimation of exhumation using velocity compaction trends. While there are studies in the literature attempting to estimate exhumation and understand its impact on source and reservoir rock compaction from a rock physics perspective, most of these studies are built on the assumption of irreversible compaction. This assumption implies that the porosity and velocity of the exhumed rock will remain the same as acquired at its maximum burial. However, the observation of the asymmetric sensitivity challenges the assumption. Besides stress, various parameters play a role in sandstone diagenesis. To comprehensively understand and model the property variations of sandstone during burial and uplift, and thereby accurately estimate the magnitude of exhumation, it is critical to consider the entire stress and diagenetic histories of the sandstone. To date, few studies have considered the asymmetrical stress sensitivity of sandstone in the workflow and investigated how it can interact with sandstone diagenesis, jointly affecting the evolution of rock properties.

Continuous stress increase leads to normal consolidation of rock, while stress release causes overconsolidation of rock. Models and workflows used in quantitative seismic interpretation often by default assume rocks are normally consolidated. However, recent studies have highlighted that overconsolidated sands, when subjected to stress release, exhibit distinct variations in acoustic and elastic properties compared to normally consolidated sands undergoing stress increase. Similar investigations for more common reservoir analogs, such as weakly cemented sandstones, are lacking. Moreover, there is a notable absence of discussion regarding the differences and similarities in the effects of overconsolidation and stress direction on the properties of unconsolidated sands and weakly cemented sandstone. Furthermore, there is a lack of assessment of these impacts on existing seismic interpretation, monitoring, and rock physics modeling approaches applied to both media.

This thesis comprises four papers, with the first three addressing the aforemen-

tioned research questions and knowledge gap. The fourth paper introduces an open-source Python library for rock physics modeling, the newly proposed model and workflow in this thesis are also included in the library. The thesis begins by introducing various theories and concepts, providing essential theoretical background for the subsequent papers. Following the introduction, each paper is presented in separate chapters. The final chapter of the thesis provides concluding remarks along with a future outlook.

1.2   Theoretical Background

1.2.1   Fundamentals of effective stress

The concept of effective stress was first proposed by Terzaghi on an empirical basis and has since been widely used to describe soil consolidation and failure behavior. Following Terzaghi (1939, 1965), effective stress is defined as the difference between the total applied stress and the pore pressure, assuming that the soil particles are incompressible and that their internal friction is equal to zero.

$$\sigma'_{ij} = \sigma_{ij} - \delta_{ij} p_f \tag{1.1}$$

The effective stress was refined later by researchers (Biot and Willis, 1957; Skempton, 1960; Bishop, 1973; Zoback and Byerlee, 1975; Zimmerman, 1991; Kwon et al., 2001; Coussy, 2004), especially regarding the fraction of the pore pressure.

According to the amended Biot law (Biot and Willis, 1957), the effective stress for a general stress state is expressed as follows:

$$\sigma'_{ij} = \sigma_{ij} - \alpha \delta_{ij} p_f \tag{1.2}$$

Where δ_{ij} is Kronecker's delta, and α is called the Biot-Willis coefficient, Biot coefficient, or effective stress coefficient (Jaeger et al., 2007).

For a porous granular medium, the Biot coefficient is related to the frame modulus of the rock, K_{fr}, and the grain material, K_0, as follows:

$$\alpha = 1 - K_{fr}/K_0 \tag{1.3}$$

The frame bulk modulus K_{fr} of a simple porous rock saturated with fluid is bounded by lower and upper elastic bounds. The lower bound $K_{fr} = 0$ is given by Reuss average and the upper bound $K_{fr} = (1 - \phi)K_0$ is given by the Voigt average. Therefore, the Biot coefficient varies within the range of $(\phi, 1]$ (Fjær et al., 2008).

The Biot poroelastic theory suggests that for weak or unconsolidated rock, α approaches 1. The weakly cemented glass bead and sandstone studied in paper 1 have a biot coefficient very close to 1. Comparing equation 1.1 to equation 1.2, it can be observed that an effective stress coefficient $\alpha = 1$ is implicitly assumed in Terzaghi's law (Terzaghi, 1923; Terzaghi, 1936). However, for consolidated rocks, $\alpha = 1$ is not a satisfactory assumption. Laboratory measurements have shown that for underground rock, the value of Biot coefficient is inversely proportional to the magnitude of the effective stress, and it decreases with porosity and varies among different lithologies (Bouteca and Sarda, 1995; Wang and Zeng, 2011; Cosenza et al., 2002). Empirical formulations for the Biot coefficient can be found in studies by Krief et al. (1990), Jizba (1991), and Zimmerman et al. (1986). Civan (2021) provides an extensive review of correlations for the Biot-Willis poroelastic coefficient. In addition to the empirical relations, the dynamic Biot coefficient can be also estimated from shear well logs expressed as the following (Zhang, 2019):

$$\tilde{\alpha} = 1 - \frac{G^*}{G_{mat}} = 1 - \frac{\rho_b V_S^{*2}}{\rho_{mat} V_{Smat}^2} \tag{1.4}$$

where V_S^{*2} and V_{Smat} are the shear wave measurements of the formation and the

matrix, respectively. Assuming a quartz matrix, the Biot coefficients calculated using equation 1.4 for the sandstone dataset in paper 2 also reveal a decline with decreasing porosity (increasing burial depth). In the Norwegian Sea dataset, the calculated Biot coefficient remains stable at around 0.9 up to a burial depth of 1600m, followed by a gradual decrease from 0.9 to 0.7 between 1600 and 3000m. The Barents Sea sandstone, on the other hand, exhibits an overall depth trend with smaller values. For depths ranging from 0 to 1500m, the Biot coefficient is approximately 0.8-0.85, followed by a decrease from 0.8 to 0.5 between 1500 and 3000m.

Estimation of effective stress

The complete description of the stress state within a formation buried underground involves stresses oriented in three orthogonal directions (Fjær et al., 2008). However, it is common to assume a vertical principle stress σ_v and a uniaxial strain condition ($\sigma_{hx} = \sigma_{hy} = \sigma_h$) for underground rocks (Zhang, 2019) carrying weight from overburden formations. The vertical effective stress σ_v' is expressed as

$$\sigma_v' = \sigma_z - \alpha_v p_f \tag{1.5}$$

where the vertical overburden stress σ_z is a function of the density and buried depth and can be calculated by integrating the bulk density profile of the overburden formations and water columns:

$$\sigma_z = \int_0^Z \rho(z)gzdz \tag{1.6}$$

In practical scenarios where density well-logs are usually absent for shallow depths shaly formations, there are pragmatic approaches to estimate the overburden stress for the sedimentary column (zhang, 2019). One common practice is to estimate the bulk density of shallow formations by using empirical mechanical compaction

functions. One such compaction function for shales was proposed by Athy (1930):

$$\rho_b^*(z) = \rho_0 + 1.3 \left(1 - e^{-bZ}\right) \tag{1.7}$$

where $\rho_b^*(z)$ represents the compacted bulk density at a specific depth z, ρ_0 is the bulk density at sea floor, b is the compaction factor. By fitting the density curve to Equation 1.7 using available bulk density data at certain depths, it is possible to obtain the shallow density ρ_0 and the compaction factor b. Subsequently, the missing values of the shaly sections can be estimated by extrapolating the fitted compaction function. Depending on the research area and type of shale, site-specific compaction functions can be used to do the interpolation and extrapolation. This approach allows for the generation of composite density profiles in the absence of direct measurements, enabling the calculation of overburden stresses for the sedimentary column. Note that in paper 2, this approach is employed to construct the well log dataset, wherein density logs are either intermittent or absent in shaly intervals near the sea floor.

Similar to the calculation of vertical overburden stress, the pore fluid pressure at any given depth can be determined by integrating fluid density from sea level to the depth of interest as:

$$p_f(z) = \int_0^Z g\rho_f(z)dz \tag{1.8}$$

where $\rho_f(z)$ is a profile of fluid density along the vertical depth.

Equation 1.2 indicates that the principle of effective stress applies to normal stresses including the horizontal effective stress σ_h' acting on the rock frame. It is commonly expressed the horizontal effective stress as a proportion of the vertical effective stress:

$$\sigma_h' = \tilde{K}\sigma_v' \tag{1.9}$$

When the stress ratio $\tilde{K}=1$, the horizontal effective stress σ'_h becomes equal to the vertical effective stress i.e., $\sigma'_h = \sigma'_v$, resulting in a hydrostatic stress state. The value of $\tilde{K}$ can vary greatly with burial depth and is sensitive to diagenesis (Bjørlykke and Høeg, 1997). If the formation deforms under uniaxial strain condition without lateral deformation, and the stress-strain curves follow linear elastic Hooke's law, the ratio $\tilde{K}$ becomes equivalent to the stress path coefficient K_0 used in laboratory uniaxial strain tests (fjær et al., 2008).

Since effective stress is imposed on the rock frame and the fluid carries the residual stress, the effective stress is also called intergranular stress (Bjørlykke and Jahren, 2010) or grain-grain net stress (fjær et al., 2008). In laboratory experiments under drained conditions, as reported in paper 1, the axial effective stresses equal the magnitude of the applied normal stresses.

1.2.2   Release of effective stress

The thesis aims to enhance the current understanding of the elastic properties of porous sandstone when subjected to the release of effective stress. Below, we provide an overview of different effective stress release scenarios that can be encountered either in controlled lab experiments or in the field.

Exhumation

The combined process of uplift and erosion, which leads to the elevation of previously buried rocks, is referred to as exhumation (Corcoran and Doré, 2005). Sedimentary basins can undergo multiple cycles of elevation and subsidence due to large-scale changes in regional stress fields. These changes can be driven by different mechanisms such as orogeny, faulting, and isostatic deglaciation rebound (Chemenda et al., 1995; Fayon et al., 2001; Warren, 2013). Figure 1.1 displays petroleum basins worldwide that have undergone exhumation.

The reduction of burial depth and the removal of overburden lead to a decrease

Figure 1.1: World map of some well-known uplifted petroliferous basins (Data modified from Henrikson et al., 2011)

in the vertical total stress. The typical overburden density ranges from 1.8 to 2.2 g/cm^3, while the water gradient falls within 1.03 to 1.07 g/cm^3 (Fjær et al., 2008). If the pore pressure gradient remains normal (i.e. also referred to as water gradient in the literature) during uplift, the effective stress imposed on precompacted rocks will also be diminished.

On the other hand, rapid uplift and erosion processes can lead to abnormally high pore pressure (Burov et al., 2001). This occurs because there isn't enough time for the pore pressure to dissipate and reach equilibrium with the surrounding rocks. Consequently, the pore pressure in these elevated formations exceeds that of neighboring formations that are normally buried. Equation 1.5 demonstrates that in the case of pore pressure buildup, the effective stress is significantly decreased, even more so than the variation in pore pressure based on the water gradient. It is worth mentioning that uplift-induced overpressure is typically transient and diminishes rapidly as the pore fluid is expelled through various secondary pathways. In practice, uplifted basins often exhibit features such as excessive cap rock failure, underfilled reservoirs, and regional faulting (Doré and Corcoran, 2002).

These observations are believed to be closely linked to uplift and erosion.

Overpressure

Equation 1.5 indicates that if the pore pressure increases while the overburden stress remains unchanged, the effective stress is reduced. This can be caused by in situ stress unloading due to overpressure. Abnormally high pore pressure can result in abnormally low effective stress of a reservoir. A good example is the Gullfaks field in the North Sea. The top of the reservoir is approximately 1850 meters deep (Fjær et al., 2008). A typical number of the effective stress gradient is 10 MPa per kilometer. Therefore, if the pore pressure in the Gullfaks field is hydrostatic, the effective stress imposed on the reservoir rock would be around 20 MPa. However, overpressuring in the post-Jurassic mudrocks in the Gullfaks area leads to elevated pore pressure (Wensaas et al., 1994; Nordgård Bolås et al., 2004), and the effective stress at Gullfaks is reduced to about 6 MPa.

Overpressure is commonly observed in shale formations and can be attributed to various mechanisms such as shale dehydration, compaction disequilibrium, and aqua-thermal effects (Osborne and Swarbrick, 1997). In addition to the authigenic origin of overpressure in low permeability formations, reservoir rocks can be artificially pressurized through fluid injection. It is worth mentioning that the pore pressure can also be increased under certain stress paths for reservoir depletion according to the simulation done by Holt et al. (2018). An interesting topic is the variation of pore pressure caused by CO_2 injection. During injection, it is expected that the increase in pore pressure remains small to avoid exceeding stress limitations. Real data have indicated that overpressure is likely to appear in the vicinity of the injector (Saul and Lumney, 2015), and tends to dissipate with time after the injection shutdown (Vilarrasa and Carrera, 2015). Careful pressure monitoring and maintenance usually can help to mitigate the overpressure issue induced by CO_2 injection (Vilarrasa and Carrera, 2015). The Sleipner field serves

as a good example where pressures have remained relatively uniform throughout its lifecycle (Chadwick, 2013). However, pressure buildup can occur due to factors such as complex geology, heterogeneity, and constrained reservoir volume (Lumley, 2019). For instance, A history-matched model of average pore pressures in the megatonne storage site at Weyburn oil field showed that CO_2 injection has increased pore pressures from hydrostatic (≈ 15Mpa) to 20 MPa (Verdon, et al., 2013). Several seismic events occurred during the initial stages of injection, and the seismicity rate increased when the injection rate was raised. Verdon et al. (2013) point out that the pressure variations can be attributed to the complex pressure history of the reservoir and the simultaneous occurrence of injection and production activities, leading to pore pressure variations across the field.

Even greater pressure variations can occur, as seen in the In-Salah project (Verdon, et al., 2013). In-Salah is a commercial-scale onshore CO_2 sequestration site where CO_2 extracted from natural gas is injected into deep saline aquifers. To enhance injectivity into low-permeability sands, CO_2 is injected through three horizontal wells. Modeled pore pressures at the injection points have substantially increased from initial conditions of around 18 MPa to approximately 30 MPa. Induced seismicity is significant in this region, and the analysis of pressure versus injection rate indicates that pressures in all three wells have likely exceeded the fracture pressure of the injection horizon for limited periods of time (Bissell et al., 2011).

Coring

Retrieving core samples from deep boreholes also involves effective stress release that occurs within a significantly shorter time frame compared to the geological timescale required for exhumation. Such rapid stress release can severely impact the mechanical properties of the core. Let's consider the simplest scenario where the core is obtained from a reservoir rock through a vertical borehole, and the in situ stress field consists of vertical principal stress, σ_v, and equal horizontal
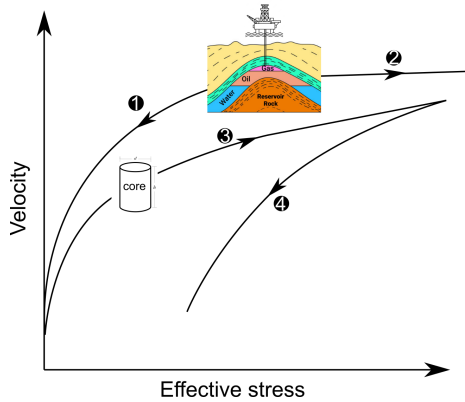
Figure 1.2: Schematic of different stress paths and the representative events for underground rocks. Stress path 1 represents the stress release/ that can be caused by exhumation, coring and fluid injection. Stress path 2 represents the stress increase caused by reservoir compaction or depletion. Stress paths 3 and 4 represent the stress loading and unloading respectively, experienced by core samples during laboratory tests.

stresses, σ_h, with $\sigma_v > \sigma_h$. The vertical stress is reduced first as the core is drilled. The horizontal stress diminishes as the core enters the core barrel. Consequently, there is a period during which the horizontal stress may exceed the vertical stress significantly. This situation can potentially lead to core failure. The coring damage has been extensively studied in the literature through laboratory experiments and numerical simulations (Santarelli and Dusseault, 1991; Holt et al., 1992; Holt et al., 2000; Corthésy and Leite, 2008; Bahrani et al., 2015). Additionally, rapid cooling and changes in pore pressure also contribute to the deterioration of the core sample (Kern et al., 2001).

Stress unloading lab test

Rock samples can undergo stress unloading in laboratory measurements for various purposes. For instance, cyclic loading experiments can be conducted to investigate stress sensitivity under normal and overconsolidated states (Zimmer, 2003). During cyclic loading, rock samples are subjected to repeated stress applications and releases. It is commonly observed that rock exhibits an unloading path that differs

from the loading path, this effect is known as hysteresis (Fjær et al., 2008). When samples undergo cyclic loading and unloading, a certain amount of irreversible deformation may occur in each cycle, which can eventually lead to material failure (Fjær et al., 2008). This phenomenon is referred to as fatigue (Suresh, 1998). The cyclic loading test is the most common approach to studying the hysteresis and fatigue hehavior of rock samples. In cases where hysteresis is undesirable, cyclic loading and unloading can also be used as an aging treatment to reduce or eliminate its effect (Bernabe, 1872; Warpinski et al., 1989; Warplnski and Teufel, 1992).

Moreover, apart from being part of the cyclic loading path, the unloading test per se serves as an important method to investigate rock failures (Huang et al., 2001; Zhu and Huang, 2019). As introduced in the content about coring, for rock cores retrieved from deep depths, the dominant recent stress history is the unloading process that occurs during and after coring. To replicate the coring effect in the laboratory, stress unloading is conducted. It is worth mentioning that reloading the core to in situ stress conditions is also a common practice to study the coring effect. This approach involves subjecting the real core to stress conditions that mimic its original state in the field. The corresponding stress path is schematically illustrated in Figure 1.2. Coring activities create cracks and reduce the elastic stiffness of the core. When the core is subjected to sufficient stress during laboratory reloading, these cracks tend to close, resulting in increased velocities. However, laboratory tests have demonstrated the irreversibility of the core damage caused by coring i.e., despite efforts to restore the stress conditions, cores may still exhibit residual damage that cannot be fully compensated for by reloading (Seto et al., 1999).

1.2.3   From sand to sandstone

The thesis aims to understand, model, and eventually predict the elastic responses of sandstone under various stress release scenarios. To achieve this, it is critical to consider the entire stress history including the stress history prior to stress release, which also influences the evolution of acoustic and elastic properties of the sandstone. Moreover, as with any other type of sedimentary rock, loose sand sediment transforms into lithified sandstone through a complex process referred to as diagenesis (Athy, 1930; Hedberg, 1936; Graham and Williams, 1985; Johnston, 1987; Mondol et al., 2007). Typical processes such as deposition, compaction, and cementation shall also be considered. Diagenesis encompasses the physical and chemical changes that take place after sediment deposition and before metamorphism (Worden and Burley, 2003). In paper 2, an integrated rock physics-diagenetic modeling scheme is implemented to elucidate the impact of stress release associated with exhumation. The modeling scheme considers the interplay of diagenesis and stress evolution, However, as famously stated, "all models are wrong," and accurately modeling all factors influencing rock property evolution during burial and uplift, as well as reconstructing the complete stress profile before any stress unloading of underground rocks, remains extremely challenging (Zoback and Kohli, 2019). Two common methods are often employed to address the challenges. Firstly, by carefully selecting the study area, refining the data collection process, and preprocessing to exclude as many interfering factors as possible. Secondly, simplification and modular description of sandstone diagenesis. Paper 2 provides a detailed description of the collection and processing of research data along with the underlying logic. It also discusses how sandstone diagenesis influences the evolution of rock acoustic and elastic properties, therefore same contents won't be repeated here. Instead, we'll delve into explaining the simplifications and assumptions we've made regarding sandstone diagenesis in the modeling process. This additional information is intended to facilitate a smoother understanding of

sandstone rock physics modeling presented in the subsequent chapters.

In a nutshell, the most fundamental assumption made in the rock physics literature related to sandstone is that sandstone diagenesis mainly consists of mechanical and chemical compaction and different processes prevail and predominate at different depths. This fundamental assumption involves several simplifications regarding the diagenesis of sandstone. A detailed explanation is as follows.

Mechanical compaction

The first simplification often made is that mechanical compaction prevails from the time of sand deposition until the temperature rises to a range where chemical compaction begins to take place.

Right after deposition, loose sand sediments will first undergo so-called mechanical compaction as the vertical compressive stress increases. As indicated by the equation 1.5. The effective stress or grain-to-grain net stress increases with burial depth, causing loose sand grains to approach, rearrange, and connect to form grain contacts and a rock framework. This is accompanied by alterations in packing. Figure 1.3 illustrates the evolution of grain contacts that commonly to be observed in real rocks at different burial stages. Mechanical compaction leads to a significant reduction of intergranular space and increases in density and frame modulus. Normally compacted loose sand sediments will usually obey an exponential decay compaction function, equation 1.7, proposed by Athy (1930) is a representative example. Note that, different types of sands can experience different degrees of mechanical compaction depending on texture, sorting, grain size and mineralogical composition (Bjørlykke and Jahren, 2010). These factors mutually constrain and influence each other. For instance, experimental findings indicate that the degree of mechanical compaction in well-sorted, dry, pure sand samples is primarily governed by grain size, which also primarily controls depositional porosity. On the other hand, the rate of porosity reduction in poorly-sorted samples during

compaction is less than that in well-sorted samples (Zadeh et al., 2016). Existing contact-based rock physics models are commonly used to interpret the influence of the aforementioned geological factors on laboratory experiments or geophysical data collected (Mavko et al. 2020). However, relying solely on rock physics models to describe the combined effects of multiple factors is not sufficient; it also requires integration with other diagenetic models (Lehocki and Avseth, 2020). For instance, altering the critical porosity in a contact-based rock physics model can depict the influence of depositional porosity on the velocity evolution of clean sandstone, implicitly reflecting the impact of grain size. However, the rock physics model itself cannot elucidate the effect of grain size on cementation. In contrast, grain size can serve as input parameters for specific diagenetic sandstone models that control the cementation process. In Paper 2, we adopted the approach proposed by Avseth et al. (2020) to combine rock physics with a kinematic sandstone diagenesis model to better align the model with geological realities.
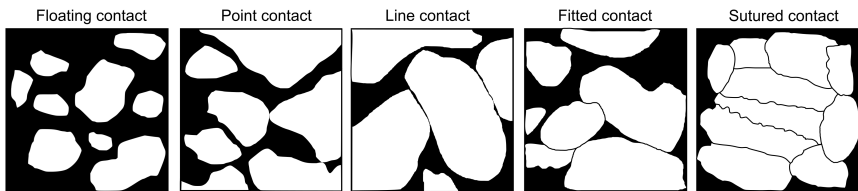
Figure 1.3: Different types of grain contact. Modified from Al-Awwad and Pomar (2015). Floating, point, and line contacts form as a result of early deposition, whereas fitted and sutured contacts indicate a higher degree of compaction.

Chemical compaction and cementation

The second simplification is that as the burial depth increases, chemical processes begin to dominate the diagenesis, particularly cementation. Cementation refers to the precipitation of new materials in pore spaces, fostering the growth of minerals and the enlargement of existing crystals (Ulmer-Scholle et al., 2014). Cementation can occur at any stage from deposition through burial to uplift and re-exposure and it predominates the mesogenetic stage (burial stage) of sandstone diagene-

sis (Ulmer-Scholle et al., 2014). In comparison to carbonate rocks which have extensive syndepositional cementation with various cement morphologies (Scholle and Ulmer-Scholle, 2003), significant cementation of sandstone during the early burial stage (from the syndepositional to eogenetic stage in sedimentology) is rare. One of the primary cement types in sandstone is quartz cementation, appearing mostly as quartz overgrowth. Extensive quartz cementation is less likely to occur at high burial depth temperatures as the solubility of quartz gently increases with temperature (Mackenzie and Bricker, 1971). These characteristics indicate that quartz cementation's influence on sandstone is primarily limited to a certain depth range, which has led to the oversight of cementation modeling during mechanical compaction in the existing literature (Lander and Walderhaug, 1999; Taylor et al., 2010; Lehocki and Avseth, 2020).

The term chemical compaction is used in many literature to encompass all the chemical processes in diagenesis including cementation. However, the strict definition of chemical compaction does not include cementation (Houseknecht, 1987). Chemical compaction refers to the pressure dissolution of existing grains and the solid-state replacement of existing minerals by new minerals. The sutured grain contact and stylolite, as illustrated in Figure 1.3, is an indication of pressure dissolution.

For simplicity, the effect of grain penetration during sandstone diagenesis on the elastic properties of sandstone is disregarded in this thesis. However, it is worth mentioning that there exist models that describe the pressure dissolution of granular aggregates under static conditions (e.g., Stephenson et al., 1992; Yasuhara et al., 2003). Dræge et al. (2006) also perform porosity modeling that considers the pressure dissolution on an empirical basis. However, at the current stage, there is still limited application of the pressure dissolution models in describing and predicting the acoustic and elastic properties of sandstone. Some early exploratory work and related studies (Bjorkum, 1996; Florez-Niño, 2004 Vanorio, 2014) may

provide inspiration and ideas for future research in this area.

Type of cement

Before delving into the simplification of cement types in the simulation, let's provide a brief overview of the common types of sandstone cement. Siliceous sandstone exhibits a range of complex cement types (Scholle, 1979), with the most predominant being various silica cement, carbonates, and clay minerals that make up the bulk of the cement volume.

As mentioned earlier, quartz cementation typically occurs during the burial stage, initiating at around 70°C, and is crucial as the primary authigenic mineral for sandstone in the Norwegian offshore (Lander and Walderhaug, 1999; Maast et al., 2011; Ogebule et al., 2020). Besides quartz cement, unstable silica minerals such as amorphous silica (opal A) and microcrystalline quartz (opal CT) can form at earlier burial stages. opal-A tends to transform into opal-CT which could eventually transform into quartz with increasing burial depth and temperature (Williams et al., 1985). However, kinetic experiments reveal that the opal-A to opal-CT transformation is rate-dependent, with a significant decrease in rate at lower temperatures (Kastner and Gieskes, 1983). The transformation of opal A to CT can significantly impact the acoustic and elastic properties of the rock. Within the transition zone, porosity can significantly decrease (Wrona et al., 2017). Opal A, being a hydrous, amorphous form of silica, loses water molecules during the transition to CT, which can cause the stiffening of the rock (Thyberg et al., 2009). However, because the transformation is more commonly observed in shale (Thyberg et al., 2009) and happens during shallow burial, it is rarely considered in sandstone diagenetic modeling.

Carbonate cement is present at different burial stages. Sandstone can form calcite concretions from syndepositional to early diagenetic stages (Walderhaug and Bjørkum, 1998), often concurrent with mechanical compaction (Mozley and Burns,

1993). However, much of the early calcite will be dissolved due to its unstable nature, thus seldom considered in the modeling. Calcite cement is more prevalent during the mesogenetic stage of sandstone, where dolomite and siderite can locally play significant roles in siliciclastic deposits (Scholle, 1979). Late mesogenetic stage calcite cements are usually postdated quartz overgrowths and authigenic clays due to decreased calcite solubility at higher temperatures (Mackenzie and Bricker, 1971). In Norwegian offshore sandstone, calcite cement occasionally appears as thin stringers with very low porosity and unusually high velocity. The layer containing calcite can be excluded from well-log data through quality control processes using rock physics diagnostics (Avseth et al., 2020).

Clay cementation is also commonly seen in sandstone (Blatt, 1979). The common morphologies of clay cement are clay coating and pore-filling clay. Clay coating can inhibit quartz overgrowth and preserve porosity reduction caused by subsequent quartz cementation (Walderhaug, 1996). Extensive illitic grain coating has been reported to significantly contribute to preserving porosities in deeply buried sandstone reservoirs, such as in the Stø Formation (burial larger than 2.6 km) in the Barents Sea (Hansen et al., 2017; Løvstad et al., 2022) and the Jurassic Garn Formation (burial larger than 4.5 km) in the Norwegian Sea (Storvoll et al., 2022). Clay coating is an important input parameter in kinematic diagenetic sandstone modeling (Walderhaug, 1996) as it determines the available surface area for quartz cementation. Pore filling clays depending on the volume fraction in the sand shale mixture influence the compaction and properties evolution to different extent (Marion, 1990). Heuristic rock physics models have been proposed to describe the porosity and velocity evolutions in both sandy-shale and shaly-sand mixtures (Yin, 1992; Dvorkin and Gutierrez, 2002). However, these models are based on the assumption that porosity is destroyed only by pore-filling clays. while cementation and other factors are ignored, making the models less applicable in modeling cement-bearing sandstone. In practice, by filtering the clay-rich data,

sandstone with a tiny amount of clay can be treated as clay-free sandstone when performing rock physics modeling.

A frequently employed simplification in the diagenetic modeling of sandstone involves assuming only one type of cement. This cement may be monophasic, like quartz cement, occurring within the cementation window. Alternatively, it can be treated as an effective cement by volume averaging more than one phase (e.g., quartz and clay). However, the reality is far more complex than these assumptions. Figure 1.4 depicts the diagenetic evolution sequence of a sandstone reservoir in the Ordos Basin (Hu et al., 2022). It illustrates that the actual diagenetic control of sandstone is more diverse and involves various cement types and timing, extending beyond the depth of the cementation window. Furthermore, it is common in diagenetic modeling workflows to assume a continuous occupation of the pore space (Dræge et al., 2006; Lehocki and Avseth, 2020), neglecting the detailed morphology, location (intra- or intergranular), and generations of cement (primary or secondary). These aspects are not typically considered in the modeling due to the limitations of the current models available.

As research and technology progress, it is essential to strive towards incorporating these complexities into diagenetic models to better capture the intricate nature of sandstone cementation. Indeed, no model can capture all the complexities of real-world systems, and the diagenetic models used in the papers included in this thesis will likely inherit the limitations mentioned earlier.

1.2.4 Rock physics theories

In Chapters 2-5, we present descriptions, applications, and extensions of various rock physics models. For the sake of completeness, we provide additional explanations of fundamental concepts and theories crucial for understanding the subsequent work. The emphasis is on elucidating how rocks respond to stress.
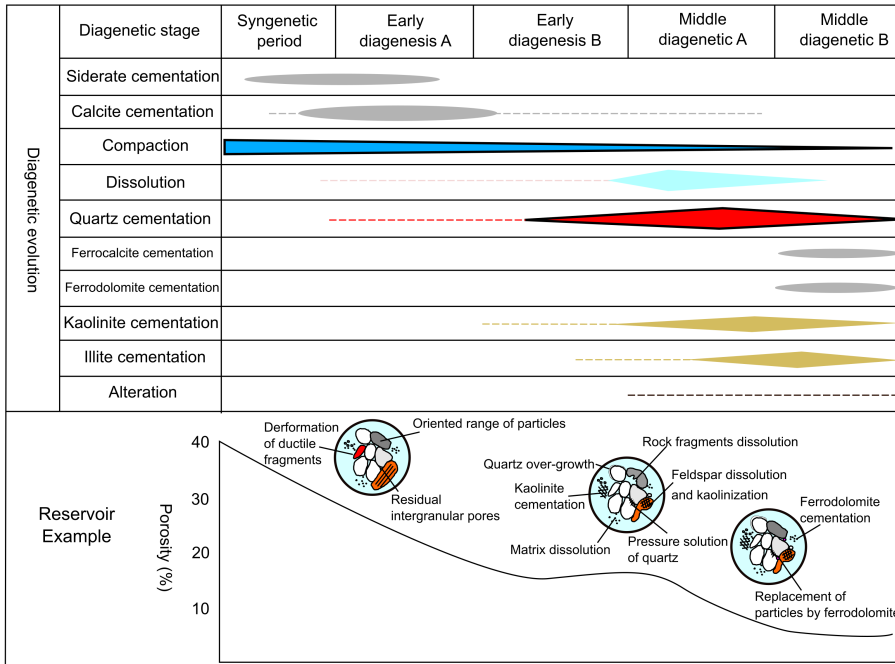
Figure 1.4: Diagenetic controls and pore evolution of a sandstone reservoir in Ordos Basin. Modified from Hu et al. (2022). Different types of carbonate cement are colored grey and clay cements are colored yellowish brown. The diagenetic processes considered in most diagenetic modeling i.e., quartz cementation and compaction are highlighted with a black border.

Normal consolidation and overconsolidation

Continuous stress increase leads to normal consolidation of rock, while stress release causes overconsolidation of rock. As illustrated by Figure 1.5, normally consolidated rock sits always at its peak level of stress, while in contrast, overconsolidated rock sits at a level of stress lower than the maximum stress level it has been subjected to (Fjær, et al., 2008). The maximum stress is commonly referred to as the preconsolidation stress in soil mechanics (Schmertmann, 1955).

When quantifying the degree of overconsolidation, the overconsolidation ratio (OCR) is commonly utilized. OCR is defined as the ratio between the difference between the past maximum effective vertical stress (max) and the present
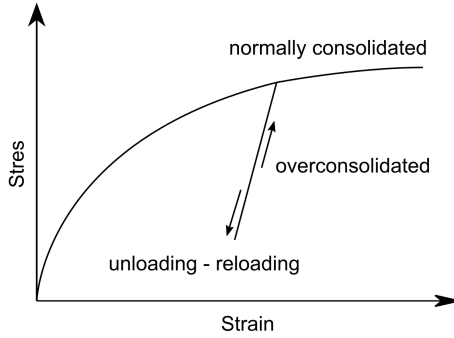
Figure 1.5: Schematic illustration of normal consolidation and overconsolidation, modified from Fjær, et al. (2008).

effective vertical stress (Casagrande, 1936):

$$OCR = \frac{\sigma'_{max}}{\sigma'} \tag{1.10}$$

Note that the diluting factor α^* introduced in paper 1 can be rewritten in terms of the overconsolidation ratio as:

$$\alpha^* = (1 - OCR^{-1})^m \tag{1.11}$$

Linear elasticity

Contact-based rock physics models are typically based on isotropic linear elasticity. The stress-strain curve of a linear elastic material follows a linear pattern, as depicted in Figure 1.6. Young's modulus of the material is equal to the gradient of this linear function. However, in reality, rocks are rarely linear elastic materials, and their behavior exhibits non-linearity resulting in a nonlinear stress-strain relationship. Porous sedimentary rocks, in particular, often exhibit hysteresis as depicted in Figure 1.6. If the strain vanishes when the stress returns to zero, the material is considered elastic. This means that it undergoes temporary deformation under loading but returns to its original state once the stress is removed.

However, if the strain does not fully recover to zero, as shown in Figure 1.6, the material has undergone permanent deformation (Fjær, et al., 2008). The hysteresis commonly observed in reality can be understood as a combination of both elastic hysteresis and permanent deformation. The corresponding illustration is shown in Figure 1.6. The hysteresis loop indicates the regions of dissipated and retained energy. In materials behaving like this, the work done during loading is not entirely released during unloading. A portion of the strain energy dissipates within the material resulting in hysteresis. Tutuncu et al. (1998) demonstrated through laboratory experiments that hysteresis in sandstones can be attributed to grain contact adhesion hysteresis and stick-slip sliding mechanisms. Grain contact adhesion hysteresis arises from mechanical instability due to asperities at the grain surface. On the other hand, stick-slip sliding mechanisms involve frictional sliding at grain contacts. The theory by Tutuncu et al. (1998) is based on the idea that grains are interlocked through grain contacts, and the separation at the contact points due to asperities can be lubricated by a water film. However, if the grain contacts are cemented, they do not significantly contribute to the total hysteresis behavior of the rock.
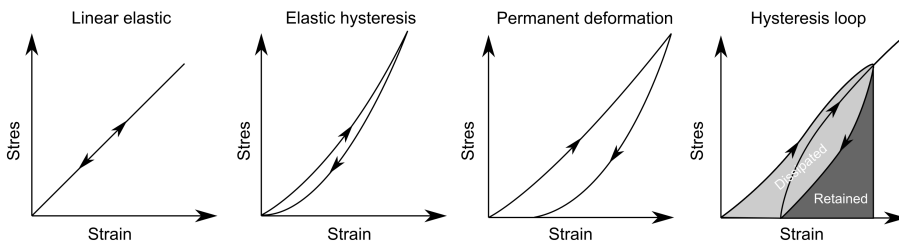
Figure 1.6: Schematic illustration of stress-strain relations of different materials. Modified from Fjær et al. (2008) and Leveille et al. (2017).

Stress dependence of rock frame

Rock physics models provide links between stress and the elastic properties of sand packs. The stress sensitivity of loose sand packs can be mathematically described by Hertz-Mindlin contact theory (Hertz, 1881; Mindlin, 1949). The Hertzian

contact law predicts a stress-dependent elastic modulus with a stress sensitivity of $K_{eff} \approx \sigma'^{1/3}$.

One limitation of the Hertz-Mindlin theory is that it yields stress sensitivity of loose sand packs at a fixed packing porosity. Various heuristic extensions of the Hertz-Mindlin theory have been proposed in the literature to account for the intricate diagenesis process of sandstone. E.g., friable model sand model (Avseth et al., 2010) is introduced to account for the porosity variation resulting from the sorting effect in sandstone.

When it comes to describing cementation in sandstone, the Contact Cement (CC) model (Dvorkin and Nur, 1996) characterizes the stiffnesses of cemented grain contacts in loose sand packs. In the CC model, the porosity is assumed to be reduced solely by cement. And cement can be deposited in two ways: grain contact cement (scheme 1) or grain coating cement (scheme 2), as illustrated in Figure 1.7. Hybrid cement schemes have also been discussed and modeled in the literature, e.g. by Allo (2019).

Although the CC model has proven to be useful in various practical cases (Dvorkin and Nur, 1996; Avseth et al., 2010), it has several limitations when considering the diagenetic features of sandstone. Firstly, it assumes that cement precipitates in a random dense packing of spherical grains with critical porosity and point-to-point grain contact, which is likely to deviate from reality as cement is deposited during burial in a precompacted rock frame with already reduced pore space. An extended model of the Dvorkin and Nur (1996) contact cement model is presented by Dvorkin and Yin (1996), it considers the effects of compaction before cement deposition which results in the variation of grain contact stiffnesses with the precompacted area between the grains. The geometric details of the grain precompaction and cement deposition are sketched in Figure 1.7.

Regarding the porosity variation away from critical porosity, a heuristic extension

of the contact cement model, i.e., the constant cement model (Avseth et al., 2010) is proposed to address the porosity reduction resulting from sorting before cementation, though from a modeling perspective, the cementation is implemented before porosity extrapolation.

In addition, for cases involving extensive cementation, the elastic moduli predicted by the CC model underestimate the reality and may not be valid. In such scenarios, alternative models such as the increasing cement model (Avseth et al., 2010) are considered in the literature for more accurate predictions.

The most noticeable limitation of the CC model is that even a tiny bit of soft cement can render the effective rock stress-insensitive. In response to this concern, Guo and Chen (2022) developed lower and upper bounds for the stress-dependent elastic wave velocities in unconsolidated cemented sands, building upon the precompacted model by Dvorkin and Yin (1995). In their approach, the grain direct contact area and cement layer thickness are allowed to vary with stress, leading to the stress-sensitive elastic properties of the cemented grain pack. Notably, the cement remains intact and elastic during variations in applied effective stress in this model. The sensitivities of the elastic wave velocities to the effective stress increase as the precompacted pressure, cement elastic moduli, and cement volume content decrease.

All the above models are based on linear elasticity without considering hysteresis. This means that when the stress is reversed, the elastic properties prediction will return to a lower value along the model prediction corresponding to the lower stress. However, these models are unable to explain the observed hysteresis and the dramatic decrease (up to 60%) in wave velocities observed in very weakly cemented samples, as presented in Chapter 2. Therefore, there is a clear need for new mechanisms and modeling approaches to explain such observations, which will also be one of the research focuses of this thesis.
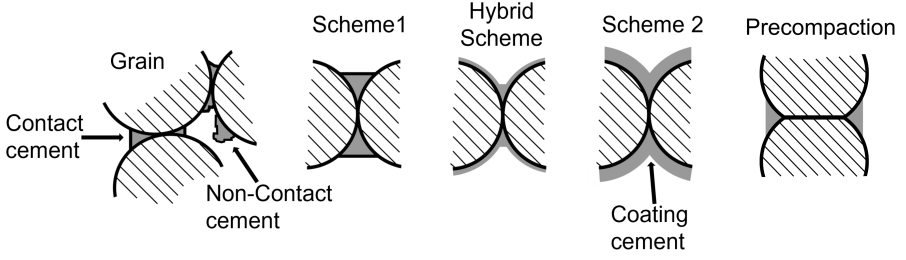
Figure 1.7: Schematic representation of different types of cement deposition and grain compaction. Modified from Mavko et al. (2020) and Dvorkin and Yin (1995).

Stress dependence of pore pressure

Undrained conditions prevail in underground formations. Although this thesis primarily focuses on studying the rock frame response to effective stress, it is worth restating the importance of pore pressure. Because the determination of effective stress, calculation of fluid properties at various P-T conditions (Batzle and Wang, 1992), as well as the effective properties of the bulk rock, require the knowledge of pore pressure. A relative issue concerning the variation of rock frame properties in response to effective stress is how pore fluid pressure changes due to changes in the total applied stress. This topic is extensive, and here, we only briefly touch upon it.

The change in pore pressure caused by a change in applied stress is characterized by Skempton's coefficients A and B, also known as the pore pressure coefficients (Skempton, 1954). For reservoir rock assuming uniaxial strain condition:

$$\Delta p_{\mathrm{f}} = B \left[\Delta \sigma_3 + A \left(\Delta \sigma_1 - \Delta \sigma_3 \right) \right] \tag{1.12}$$

The change in mean stress is defined as the arithmetic mean of changes in each normal stress and can be written as (Fjær et al., 2008):

$$\Delta \bar{\sigma} = \frac{1}{3} \left(\Delta \sigma_1 + 2 \Delta \sigma_3 \right) = \Delta \sigma_3 + \frac{1}{3} \left(\Delta \sigma_1 - \Delta \sigma_3 \right) \tag{1.13}$$

Therefore equation 1.12 can be written in terms of the applied mean stress as:

$$\Delta p_{\mathrm{f}} = B \left[\Delta \bar{\sigma} + \left(A - \frac{1}{3} \right) (\Delta \sigma_1 - \Delta \sigma_3) \right] \qquad (1.14)$$

For isotropic linearly elastic porous rock, A= 1/3 (Holt et al., 2018). Therefore we have

$$\frac{\Delta p_f}{\Delta \sigma} = B \qquad (1.15)$$

Here we can see that Skempton's B coefficient quantifies the change in pore pressure with respect to confining stress under undrained conditions. Hart and Wang (1999, 2010) demonstrated through laboratory measurements and inversion of the measured data that Skempton's B decreases with increasing effective stress for Berea sandstone.

Biot-Gassmann theory is the most common way of determining pore-fluid compressibility or calculating other poroelastic constants of the undrained rock. Skempton's B coefficient is related to the Biot coefficient α as (Fjær et al., 2008; Holt et al., 2018):

$$B = \frac{\alpha M}{K_{fr} + \alpha^2 M} \qquad (1.16)$$

Where K_{fr} is the dry rock bulk modulus. The storage modulus M is given by

$$\frac{1}{M} = \frac{\alpha - \phi}{K_0} + \frac{\phi}{K_f} \qquad (1.17)$$

Where K_0 and K_f are the bulk moduli of solid grain and fluid, respectively.

1.3   Thesis outline

This thesis comprises four papers presented respectively in Chapters 2-5. Additionally, two extended abstracts have been included in the appendix. It is im-

portant to note that since the abstracts are preliminary results for the already published papers, only basic information, including the title, introduction, and conference details, are provided in the appendix.

In Chapter 2, we present a novel rock physics model aimed at quantitatively describing the stress sensitivity of weakly to moderately cemented sandstone during effective stress release. The model is built upon the patchy cement model and incorporates microscopic observations of cement cracking and crumbling. To account for the reduced coherence of the cement coherence upon stress release, we introduce the cement diluting factor, which helps analyze stress sensitivity changes during stress removal. Additionally, we put forward a sequential modeling approach i.e., PCM-VPCM, which effectively explains the hysteresis behavior observed in cemented sandstone during stress loading and unloading. To validate our model's performance, we compared it against published measurements. The results demonstrate a strong agreement between the modeled stress sensitivities and the measured wave velocities. The result is published in *Geophysics*, 2023, and also partially presented at the First EAGE Rock Physics Workshop in Latin America.

In Chapter 3, we perform integrated rock physics modeling using the model developed in Chapter 2 guided by predefined burial history to simulate the effect of stress release and cementation on the velocity and porosity of rocks during burial and uplift. Based on the different stress sensitivities of velocity and porosity to stress release, we propose porosity inconsistency as a measure of how much the rock has been affected by stress release induced weakening. We discover that the disparity between porosity sensitivity and velocity sensitivity to stress release can be leveraged to derive a metric "porosity inconsistency" which can serve as both a qualitative and quantitative measure for identifying and evaluating stress release in sandstone using geophysical field measurements. We create an extensive well-log database that consists of clean sandstone data from the Norwegian Sea normally

buried and uplifted areas and the Barents Sea uplifted areas. We show for the first time using field data that the exhumation estimation using velocity depths trend yield underestimated magnitude compared to estimated using density/porosity depth trend. The porosity inconsistency indicates the degree of underestimation and it is correlated with the amount of exhumation. Field data observations are aligned with the conceptual rock physics modeling. The findings in this work will contribute to the improved understanding of interactions between exhumation, cementation, and velocity of rocks. The result is published in *Geophysics*, 2023.

In Chapter 4, We use laboratory data, field data, and rock physics modeling approaches to reveal stress paths, overconsolidation, cementation, and their effects on the acoustic elastic and petrophysical properties of unconsolidated sands and weakly cemented sandstone. More importantly, we aim to demonstrate how these factors impact the well-established models and workflows commonly used in seismic rock physics. The findings of the study indicate discernible disparities in the behavior of overconsolidated sands and sandstone, as influenced by stress release, in comparison to their normally consolidated counterparts. Specifically, mechanical compaction emerges as the driving mechanism dictating the response of unconsolidated sands under conditions of stress loading and subsequent unloading. However, the weakly cemented sandstone shows more sophisticated features because of cementation. The role of cement is multifaceted: the saturation of cement attenuates the stress sensitivity of sandstone. On the other hand, the strain energy possessed by the cement behavior becomes manifest upon stress release, leading to markedly distinct behavior compared to over-consolidated sands affected by stress release. This investigation underscores the paramount significance of acknowledging and accommodating the ramifications of overconsolidation and stress release on porous rock within contemporary seismic rock physics frameworks. The oversight of these aspects has the potential to encumber the precision of time-lapsed monitoring and the estimation of fluid saturation within formations

of overconsolidated porous rock that also contains cementitious constituents. The work is submitted to *Geophysics*.

In Chapter 5, we present an open-source Python library *rockphypy*. *rockphypy* has successfully migrated and optimized a wide range of rock physics models from Stanford SRB Matlab tools to Python. Additionally, it extends the functionality by introducing new functions and practical workflows. Moreover, the models and knowledge gained during the completion of this dissertation have also been incorporated into the library. By presenting *rockphypy*, we aim to promote ongoing research on stress release and encourage innovation in rock physics. The library caters to individuals interested in rock physics and empowers them to apply rock physics tools in their work and research effectively. The work is published in *SoftwareX*.

1.4   Contributions

Contributions to the papers presented in this dissertation are as follows:

Paper 1 (Chapter 2): The work was carried out by Jiaxin Yu as the lead researcher and author. Kenneth Duffaut and Per Avseth participated as supervisors and provided theoretical support.

Paper 2 (Chapter 3): The work was carried out by Jiaxin Yu as the lead researcher and author. Kenneth Duffaut and Per Avseth participated as supervisors.

Paper 3 (Chapter 4): The work was carried out by Jiaxin Yu as the lead researcher and author. Per Avseth and Kenneth Duffaut participated as supervisors.

Paper 4 (Chapter 5): The work was carried out by Jiaxin Yu as the lead researcher and author. Tapan Mukerji participated as scientific advisor and Per Avseth participated as supervisor.

Two Extended abstracts (Appendices): The work was carried out by Jiaxin Yu with Kenneth Duffaut and Per Avseth participating as supervisors.

References

Al-Awwad, S. F., and L. Pomar, 2015, Origin of the rudstone–floatstone beds in the Upper Jurassic Arab-D reservoir, Khurais Complex, Saudi Arabia: Marine and Petroleum Geology, 67, 743–768.

Allo, F., 2019, Consolidating rock-physics classics: A practical take on granular effective medium models: The Leading Edge, 38, 334–340.

Athy, L. F., 1930, Density, porosity, and compaction of sedimentary rocks: AAPG Bulletin, 14, 1–24.

Avseth, P., T. Mukerji, and G. Mavko, 2010, Quantitative seismic interpretation: Applying rock physics tools to reduce interpretation risk: Cambridge University Press.

Bahrani, N., B. Valley, and P. K. Kaiser, 2015, Numerical simulation of drilling-induced core damage and its influence on mechanical properties of rocks under unconfined condition: International Journal of Rock Mechanics and Mining Sciences, 80, 40–50.

Batzle, M., and Z. Wang, 1992, Seismic properties of pore fluids: Geophysics, 57, 1396–1408.

Bernabe, Y., 1987, The effective pressure law for permeability during pore pressure and confining pressure cycling of several crystalline rocks: Journal of Geophysical Research: Solid Earth, 92, 649–657.

Biot, M. A., 2004, General Theory of Three-Dimensional Consolidation: Journal of Applied Physics, 12, 155–164.

Biot, M. A., and D. G. Willis, 1957, The Elastic Coefficients of the Theory of Consolidation: Journal of Applied Mechanics, 24, 594–601.

Bishop, A., 1973, The influence of an undrained change in stress on the pore pressure in porous media of low compressibility: Geotechnique, 23, 435–442.

Bissell, R., D. Vasco, M. Atbi, M. Hamdani, M. Okwelegbe, and M. Goldwater, 2011, A full field simulation of the in salah gas production and CO_2 storage project using a coupled geo-mechanical and thermal fluid flow simulator: Energy Procedia, 4, 3290–3297.

Bjorkum, P. A., 1996, How important is pressure in causing dissolution of quartz in sandstones? Journal of Sedimentary Research, 66, 147–154.

Bjørlykke, K., and K. Høeg, 1997, Effects of burial diagenesis on stresses, compaction and fluid flow in sedimentary basins: Marine and Petroleum Geology, 14, 267–276.

Bjørlykke, K., and J. Jahren, 2015, Sandstones and sandstone reservoirs: Petroleum geoscience: From sedimentary environments to rock physics, 119–149.

Boutèca, M., and J. Sarda, 1995, Experimental measurements of thermoporoelastic coefficients: Mechanics of porous media, 9, 31–42.

Burov, E., L. Jolivet, L. Le Pourhiet, and A. Poliakov, 2001, A thermomechanical model of exhumation of high pressure (HP) and ultra-high pressure (UHP) metamorphic rocks in alpine-type collision belts: Tectonophysics, 342, 113–136.

Casagrande, A., 1936, The determination of the pre-consolidation load and its practical significance: Proc. 1st Int. Conf. Soil Mech., 3–60.

Chadwick, R., 2013, Offshore CO_2 storage: Sleipner natural gas field beneath the North Sea, in Geological storage of carbon dioxide (CO_2): Elsevier, 227–253e.

Chemenda, A. I., M. Mattauer, J. Malavieille, and A. N. Bokun, 1995, A mech-

anism for syn-collisional rock exhumation and associated normal faulting: results from physical modelling: Earth and planetary science letters, 132, 225–232.

Civan, F., 2021, Parameterization of Biot–Willis effective-stress coefficient for deformation and alteration of porous rocks: Transport in Porous Media, 138, 337– 368.

Corthèsy, R., and M.-H. Leite, 2008, A strain-softening numerical model of core discing and damage: International Journal of Rock Mechanics and Mining Sciences, 45, 329–350.

Cosenza, P., M. Ghoreychi, G. De Marsily, G. Vasseur, and S. Violette, 2002, Theoretical prediction of poroelastic properties of argillaceous rocks from in situ specific storage coefficient: Water Resources Research, 38, 25–1.

Coussy, O., 2004, Poromechanics: John Wiley & Sons.

Dorè, A., D. Corcoran, and I. Scotchman, 2002, Prediction of the hydrocarbon system in exhumed basins, and application to the NW European margin: Geological Society, London, Special Publications, 196, 401–429.

Dræge, A., M. Jakobsen, and T. A. Johansen, 2006, Rock physics modelling of shale diagenesis: Petroleum Geoscience, 12, 49–57.

Dvorkin, J., and A. Nur, 1996, Elasticity of high-porosity sandstones: Theory for two North Sea data sets: Geophysics, 61, 1363–1370.

Dvorkin, J. and M.A. Gutierrez, 2002, Grain sorting, porosity and elasticity: PETROPHYSICS-HOUSTON, 43, 3, 185-196.

Dvorkin, J., and H. Yin, 1995, Contact laws for cemented grains: Implications for grain and cement failure: International Journal of Solids and Structures, 32,

2497–2510.

Fayon, A. K., D. L. Whitney, C. Teyssier, J. I. Garver, and Y. Dilek, 2001, Effects of plate convergence obliquity on timing and mechanisms of exhumation of a mid-crustal terrain, the central Anatolian crystalline complex: Earth and Planetary Science Letters, 192, 191–205.

Florez-Ninõ, J.-M., 2004, Pressure-solution and the rock physics diagenetic trend in quartzose sandstones: SEG International Exposition and Annual Meeting, SEG, SEG–2004.

Graham, S., and L. Williams, 1985, Tectonic, depositional, and diagenetic history of Monterey formation (Miocene), central San Joaquin basin, California: AAPG Bulletin, 69, 385–411.

Guo, J., and X. Chen, 2022, Pressure dependence of elastic wave velocities of unconsolidated cemented sands: Geophysics, 87, MR161–MR175.

Hart, D., and H. Wang, 1999, Pore pressure and confining stress dependence of poroelastic linear compressibilities and Skempton's b coefficient for Berea sandstone: ARMA US Rock Mechanics/Geomechanics Symposium, ARMA, ARMA–99.

Hart, D. J., and H. F. Wang, 2010, Variation of unjacketed pore compressibility using Gassmann's equation and an overdetermined set of volumetric poroelastic measurements: Geophysics, 75, N9–N18.

Hedberg, H. D., 1936, Gravitational compaction of clays and shales: American Journal of Science, 5, 241–287.

Hertz, H., 1881, Über die Berührung fester elastischer Körper. J reine und angewandte Mathematik, 92, 156.

Holt, R., M. Brignoli, and C. Kenter, 2000, Core quality: quantification of coring-induced rock alteration: International Journal of Rock Mechanics and Mining Sciences, 37, 889–907.

Holt, R. M., A. Bakk, J. Stenebråten, A. Bauer, and E. Fjær, 2018, Skempton's A—a key to man-induced subsurface pore pressure changes: ARMA US Rock Mechanics/Geomechanics Symposium, ARMA, ARMA–2018.

Holt, R. M., M. Brignoli, E. Fjaer, T. E. Unander, and C. J. Kenter, 1994, Core damage effects on compaction behaviour: SPE/ISRM Rock Mechanics in Petroleum Engineering, SPE, SPE–28027.

Holt, R. M., and C. J. Kenter, 1992, Laboratory simulation of core damage induced by stress release: ARMA US Rock Mechanics/Geomechanics Symposium, ARMA, ARMA–92.

Houseknecht, D. W., 1987, Assessing the relative importance of compaction processes and cementation to reduction of porosity in sandstones: AAPG Bulletin, 71, 633–642.

Hu, Y., Y. Guo, H. Qing, and J. Zhang, 2022, Diagenetic control of reservoir performance and its implications for reservoir prediction in Jinni sandstone of upper carboniferous in the Middle East ordos basin: ACS omega, 7, 39697–39717.

Huang, R., X. Wang, and L. Chan, 2001, Triaxial unloading test of rocks and its implication for rock burst: Bulletin of Engineering Geology and the Environment, 60, 37–41.

Jaeger, J. C., N. G. Cook, and R. Zimmerman, 2009, Fundamentals of rock mechanics: John Wiley & Sons.

Jizba, D. L., 1991, Mechanical and acoustical properties of sandstones and shales: Stanford University.

Johnston, D. H., 1987, Physical properties of shale at temperature and pressure: Geophysics, 52, 1391–1401.

Kern, H., T. Popp, F. Gorbatsevich, A. Zharikov, K. Lobanov, and Y. P. Smirnov, 2001, Pressure and temperature dependence of Vp and Vs in rocks from the superdeep well and from surface analogues at kola and the nature of velocity anisotropy: Tectonophysics, 338, 113–134.

Krief, M., J. Garat, J. Stellingwerff, and J. Ventre, 1990, A petrophysical interpretation using the velocities of p and s waves (full-waveform sonic): The log analyst, 31.

Kwon, O., A. K. Kronenberg, A. F. Gangi, and B. Johnson, 2001, Permeability of Wilcox shale and its effective pressure law: Journal of Geophysical Research: Solid Earth, 106, 19339–19353.

Lander, R. H., and O. Walderhaug, 1999, Predicting porosity through simulating sandstone compaction and quartz cementation: AAPG Bulletin, 83, 433–449.

Lehocki, I., and P. Avseth, 2021, From cradle to grave: how burial history controls the rock-physics properties of quartzose sandstones: Geophysical Prospecting, 69, 629–649.

Leveille, P., M. Sepehri, and D. B. Apel, 2017, Rock bursting potential of kimberlite: a case study of Diavik diamond mine: Rock Mechanics and Rock Engineering, 50, 3223–3231.

Lumley, D., 2019, The role of geophysics in carbon capture: Geophysics and geosequestration, 12.

Maast, T.E., J. Jahren, and K. Bjørlykke, 2011, Diagenetic controls on reservoir quality in Middle to Upper Jurassic sandstones in the South Viking Graben, North Sea: AAPG bulletin, 95, 11, 1883-1905.

Mackenzie, F., and O. Bricker, 1971, Cementation of sediments by carbonate minerals: Carbonate cements. John Hopkins Univ Press, Baltimore, 239–246.

Marion, D., and A. Nur, 1991, Pore-filling material and its effect on velocity in rocks: Geophysics, 56, 2, 225–230.

Mavko, G., T. Mukerji, and J. Dvorkin, 2020, The rock physics handbook: Cambridge University Press.

Mondol, N. H., K. Bjørlykke, J. Jahren, and K. Høeg, 2007, Experimental mechanical compaction of clay mineral aggregates—changes in physical properties of mudstones during burial: Marine and petroleum geology, 24, 289–311.

Mozley, P. S., and S. J. Burns, 1993, Oxygen and carbon isotopic composition of marine carbonate concretions; an overview: Journal of Sedimentary Research, 63, 73–83.

Nordgård Bolås, H. M., C. Hermanrud, and G. M. Teige, 2004, Origin of overpressures in shales: Constraints from basin modeling: AAPG Bulletin, 88, 193–211.

Ogebule, O.Y., J. Jahren, and N.H. Mondol, 2020, Compaction, rock physics and rock properties of sandstones of the Stø Formation: Case study of five wells from the south-western Barents Sea, Norway: Marine and Petroleum Geology, 119, 104448.

Osborne, M. J., and R. E. Swarbrick, 1997, Mechanisms for generating overpressure in sedimentary basins: A reevaluation: AAPG Bulletin, 81, 1023–1041.

Santarelli, F., and M. Dusseault, 1991, Core quality control in petroleum engineering: ARMA US Rock Mechanics/Geomechanics Symposium, ARMA, ARMA– 91.

Saul, M., and D. Lumley, 2015, The combined effects of pressure and cementation on 4D seismic data: Geophysics, 80, WA135–WA148.

Schmertmann, J. H., 1955, The undisturbed consolidation behavior of clay: Transactions of the American Society of Civil Engineers, 120, 1201–1227.

Scholle, P. A., 1979, A color illustrated guide to constituents, textures, cements, and porosities of sandstones and associated rocks: American Association of Petroleum Geologists.

Scholle, P. A., and D. S. Ulmer-Scholle, 2003, A color guide to the petrography of carbonate rocks: grains, textures, porosity, diagenesis, AAPG memoir 77: AAPG, 77.

Seto, M., D. Nag, and V. Vutukuri, 1999, In-situ rock stress measurement from rock cores using the acoustic emission method and deformation rate analysis: Geotechnical & Geological Engineering, 17, 241–266.

Skempton, A., 1984, Effective stress in soils, concrete and rocks: Selected papers on soil mechanics, 1032, 4–16.

Stephenson, L., W. Plumley, and V. Palciauskas, 1992, A model for sandstone compaction by grain interpenetration: Journal of Sedimentary Research, 62, 11–22.

Storvoll, V., K. Bjørlykke, D. Karlsen, and G. Saigal, 2002, Porosity preservation in reservoir sandstones due to grain-coating illite: a study of the Jurassic Garn Formation from the Kristin and Lavrans fields, offshore Mid-Norway: Marine and Petroleum Geology, 19,6,767-781.

Suresh, S., 1998, Fatigue of materials: Cambridge University Press.

Taylor, T. R., M. R. Giles, L. A. Hathon, T. N. Diggs, N. R. Braunsdorf, G.

V. Birbiglia, M. G. Kittridge, C. I. Macaulay, and I. S. Espejo, 2010, Sandstone diagenesis and reservoir quality prediction: Models, myths, and reality: AAPG Bulletin, 94, 1093–1132.

Teng, S., and M. Sams, 2023, Depth-dependent P-wave anisotropy and its influence on AVO interpretation in the Northern Malay Basin: In 84th EAGE Annual Conference & Exhibition, European Association of Geoscientists & Engineers. 1, 1-5.

Terzaghi, K. v., 1923, Die Berechnug der Durchlassigkeit des Tones aus dem Verlauf der hydromechanischen Spannungserscheinungen: Sitzungsber. Akad. Wiss.(Wien). Math.-Naturwiss. Kl., Abt. Iia, 132, 125–138.

Terzaghi, K. v., 1936, The shearing resistance of saturated soils and the angle between the planes of shear: First international conference on soil Mechanics.

Terzaghi, K. v., 1939, 45th James Forrest lecture, 1939. soil mechanics - a new chapter in engineering science: Journal of the Institution of Civil Engineers, 12, 106–142. 54–59.

Terzaghi, K. v., 1965, Theoretical soil mechanics, John Wiley & Sons, New York.

Tutuncu, A. N., A. L. Podio, and M. M. Sharma, 1998, Nonlinear viscoelastic behavior of sedimentary rocks, part ii: Hysteresis effects and influence of type of fluid on elastic moduli: Geophysics, 63, 195–203.

Ulmer-Scholle, D. S., P. A. Scholle, J. Schieber, and R. J. Raine, 2014, A color guide to the petrography of sandstones, siltstones, shales and associated rocks: American Association of Petroleum Geologists Tulsa, OK, USA, 109.

Vanorio, T., 2015, Recent advances in time-lapse, laboratory rock physics for the characterization and monitoring of fluid-rock interactions: Geophysics, 80, WA49–WA59.

Verdon, J. P., J.-M. Kendall, A. L. Stork, R. A. Chadwick, D. J. White, and R. C. Bissell, 2013, Comparison of geomechanical deformation induced by megatonne-scale CO_2 storage at Sleipner, Weyburn, and In-Salah: Proceedings of the National Academy of Sciences, 110, E2762–E2771.

Vilarrasa, V., and J. Carrera, 2015, Geologic carbon storage is unlikely to trigger large earthquakes and reactivate faults through which CO_2 could leak: Proceedings of the National Academy of Sciences, 112, 5938–5943.

Walderhaug, O. and P.A. Bjørkum, 1998, Calcite cement in shallow marine sandstones: Growth mechanisms and geometry: International Association of Sedimentologists, Special Publication 26, 179–192.

Walderhaug, O., 1996, Kinetic modeling of quartz cementation and porosity loss in deeply buried sandstone reservoirs: AAPG Bulletin, 80, 731–745.

Wang, C., and Z. Zeng, 2011, Overview of geomechanical properties of Bakken formation in Williston basin, North Dakota: Presented at the 45th US rock mechanics/geomechanics symposium, OnePetro.

Warpinski, N. R., and P. T. Branagan, 1989, Altered-stress fracturing: Journal of petroleum technology, 41, 990–997.

Warplnski, N., and L. Teufel, 1992, Determination of the effective stress law for permeability and deformation in low-permeability rocks: SPE formation evaluation, 7, 123–131.

Warren, C., 2013, Exhumation of (ultra-) high-pressure terranes: concepts and mechanisms: Solid Earth, 4, 75–92.

Wensaas, L., H. Shaw, K. Gibbons, P. Aagaard, and H. Dypvik, 1994, Nature and causes of overpressuring in mudrocks of the Gullfaks area, North Sea: Clay Minerals, 29, 439–449.

Williams, L. A., G. A. Parks, and D. A. Crerar, 1985, Silica diagenesis; I, solubility controls: Journal of Sedimentary Research, 55, 301–311.

Worden, R. H., and S. Burley, 2003, Sandstone diagenesis: the evolution of sand to stone: Sandstone diagenesis: Recent and ancient, 1–44.

Zadeh, M.K., N.H. Mondol, and J .Jahren, 2016, Experimental mechanical compaction of sands and sand–clay mixtures: a study to investigate evolution of rock properties with full control on mineralogy and rock texture: Geophysical Prospecting, 64, 4-Advances in Rock Physics, 915-941.

Zhang, J. J., 2019, Applied petroleum geomechanics: Gulf Professional Publishing.

Zhu, T., and D. Huang, 2019, Experimental investigation of the shear mechanical behavior of sandstone under unloading normal stress: International Journal of Rock Mechanics and Mining Sciences, 114, 186–194.

Zimmer, M. A., 2003, Seismic velocities in unconsolidated sands: Measurements of pressure, sorting, and compaction effects.

Zimmerman, R. W., 1990, Compressibility of sandstones.

Zimmerman, R. W., W. H. Somerton, and M. S. King, 1986, Compressibility of porous rocks: Journal of Geophysical Research: Solid Earth, 91, 12765–12777.

Zoback, M. D., and J. Byerlee, 1975, Permeability and effective stress: AAPG Bulletin, 59, 154–158.

Zoback, M. D., and A. H. Kohli, 2019, Unconventional reservoir geomechanics: Cambridge University Press.

CHAPTER 2

STRESS SENSITIVITY OF ELASTIC MODULI IN HIGH-POROSITY CEMENTED SANDSTONE — HEURISTIC MODELS AND EXPERIMENTAL DATA

ABSTRACT: Quantitative description of the reservoir rock stress sensitivity is critical for seismic modeling and interpretation. Laboratory studies have indicated that the wave velocity of high porosity cemented sandstone is asymmetrically much more sensitive to stress unloading than stress loading. However, there is a lack of a simple rock physics model that is capable of describing the asymmetric stress sensitivity of reservoir rock. A new rock physics model is developed by extending an existing rock physics model based on contact theory combined with elastic bounds. The new model relates the stress softening of rock to cement cracking and crumbling induced by stress release. The diluting factor is introduced to describe the weakening of effective cement and analyze the increase of stress sensitivity when the stress is gradually removed. The combination of the new model and its base model forms a rock physics modeling workflow that can accurately describe the evolution of velocities measured in samples undergoing stress loading and unloading. The model performance is compared with samples representing synthetic weakly cemented glass bead pack and sandstone manufactured with different types of cement at different forming stress levels. The modeling results are in accordance with the measured stress sensitivities of wave velocities. The sequential model calibration using a simple constraint optimization approach yields important calibration parameters that are indicative of the elastic stress sensitivity and damage behavior in the studied rocks. The model can be particularly interesting for time-lapse monitoring of fluid injection and seismic interpretation of overpressured reservoir rock.

2.1 Introduction

Dry rock stiffnesses can vary greatly with changing effective stress. Intriguingly, laboratory and numerical studies show the stress sensitivity of weakly cemented sandstone upon unloading can be significantly larger than that observed during stress loading (Holt et al., 2014; Langlois and Jia, 2014; Torset et al., 2021).

Accounting for the variation of the stress sensitivity is critical for seismic interpretation and reservoir characterization in an exhumed area (Bredesen et al., 2019). It also facilitates the pressure maintenance and time-lapsed monitoring of reservoir fluid injection.

The lack of useful rock physics models that map the consequences of stress release effect on poroelastic attributes of the reservoir rock has been mentioned in the literature (Langlois and Jia, 2014; Weinzierl and Wiese, 2021). The stress release results in reduced uniaxial compressive strength, reduced stiffness, and reduced acoustic velocities. These alterations are mainly attributed to the mechanical weakening of the cement by microcracks (Holt et al., 2005). Several works have applied and explored this assumption, e.g., Vernik and Hamman (2009) apply the rearranged exponential rise function from Shapiro (2003) to predict the velocity variations as a function of effective stress. Stress sensitivity can be changed by varying the exponent relating to crack density in the function. Saul and Lumley (2015) simulate the injection-induced pressure softening of the cement by varying the cement volume in the heuristic velocity-pressure-cementation model from Avseth and Skjei (2011) and better assess the observed 4D anomalies. Bredesen et al. (2019) show that velocity predictions of tight sandstone from an uplifted area can be considerably improved by accounting for the effect of microcracks using the "Kite" model which combines the contact cement model with differential effective medium theory (Berryman, 1992) to incorporate a crack-like inclusion geometry in the low porosity range (Avseth et al., 2014). Torset et al. (2021) apply a modified anisotropic crack model (Fjaer, 2006) to fit the measured P-wave velocities in a weakly cemented synthetic sandstone upon stress unloading, and the modeling result agrees with the measured data. In this work, we will present a new rock physics model that aims to quantitatively assess and predict the evolution of stress dependence in high-porosity weakly to moderately cemented sandstone (porosity >20%) as stress is progressively removed. The model is based on the patchy ce-

ment model (PCM) proposed by Avseth et al. (2016). It is widely accepted that velocities in unconsolidated sands exhibit stress sensitivity that arises from grain-grain contact and friction-resisted rotation (Hertz, 1882; Mindlin, 1949; Winkler, 1983; Walton, 1987; Norris and Johnson, 1997). When the sands are cemented, the resulting sandstone will become completely stress insensitive (Dvorkin and Nur, 1996). However, several workers have observed that cemented reservoirs rock can have significant stress sensitivity that might originate from the inhomogeneous spatial distribution of the cement within the grain packing (Avseth and Skjei, 2011; Duffaut et al., 2011). Against this background, Avseth et al. (2016) propose the PCM to make the high-porosity cemented sandstone still stress sensitive by mixing the cemented sandstone with unconsolidated sands using a nested Hashin and Shtrikman (1963) (HS) mixing combined with contact theory.

Contact-based effective medium theory assumes that the distribution of contacts around grains is statistically homogeneous (Mavko et al., 2020). This assumption holds approximately when predicting compressional modulus but fails for shear modulus prediction (Makse et al., 2004). To resolve the discrepancy among experimental measurements of acoustic properties from contact theory estimates, binary models that honor the nonuniform contact in the grain assembly are proposed (Bachrach and Avseth, 2008). A similar correction also is given by Dutta et al. (2010). Duffaut et al. (2010) also suggest a methodology that accounts for the fact that all grains probably exist somewhere between the limits of no-slip and slip. In this work, shear correction is implemented in the PCM to calibrate the overpredicted shear modulus from contact theory.

Our overall modeling strategy is to extend the PCM to a varying patchiness cement model (VPCM) by nonlinear stress-dependent diluting guided by a newly proposed pragmatic function. By combining the experimental evidence, we identify that the crumbling of brittle cement also might contribute to the deterioration of the rock stiffness. This effect can be seamlessly incorporated into the proposed VPCM. A

46

two-step sequential calibration of PCM and the newly proposed model is suggested. The modeling workflow is tested using two relevant published data sets of synthetic cemented glass bead and sandstone. The calibrated parameters derived from the data are interpreted in terms of their physical implications.

2.2   Rock physics modeling

2.2.1   Patchy cement model

Avseth et al. (2016) propose the PCM to account for the observed stress sensitivity in medium- to high-porosity cemented sandstone. *Patchy* means the microstructure of the cemented sandstone can be regarded as a mixture of two end members: stress-sensitive unconsolidated sands and stress-insensitive cemented sandstones (where all grain contacts are cemented). The stiffnesses of the soft loose sand K_W and G_W at critical porosity ϕ_c are obtained by applying the Walton (1987) contact theory with shear correction (Bachrach and Avseth, 2008; Duffaut et al., 2010; Dutta et al., 2010; see Appendix 2.A). The stiff cemented sandstone moduli K_{CEM} and G_{CEM} are modeled according to the contact cement model (Dvorkin and Nur, 1996). The amount of cement input into the contact cement model is a predefined cementation limit ϕ_{CEM} in Avseth et al. (2016), beyond which the sandstone is completely stress insensitive. The choice of this bulk volume of the cement limit is subjective, and 10% is used in Avseth et al. (2016), assuming that all the stress-sensitive grain contacts are completely cemented at this threshold volume.

Once K_W, G_W, K_{CEM}, and G_{CEM} are calculated, they are mixed with HS bound to obtain the stiffnesses of the effective well-sorted end member of patchy cement sandstone. Physically, HS bound can be interpreted as a two-phase composite consisting of inner cores and coating shells. Depending on the coating phase stiffness in HS, different patchiness of cement can be obtained. The dry effective

moduli K_{CC} and G_{CC} for a well-sorted connected patchy cement sandstone can be modeled with stiff cemented sandstone coating the unconsolidated sands (i.e., HS upper bound):

$$K_{\text{CC}} = K_{\text{CEM}} + \frac{(1 - f_{\text{CC}})}{\left(K_{\text{W}} - K_{\text{CEM}}\right)^{-1} + f_{\text{CC}}\left(K_{\text{CEM}} + \frac{4}{3}G_{\text{CEM}}\right)^{-1}} \tag{2.1a}$$

$$G_{\text{CC}} = G_{\text{CEM}} + \frac{(1 - f_{\text{CC}})}{\left(G_{\text{W}} - G_{\text{CEM}}\right)^{-1} + 2f_{\text{CC}}\left(\frac{K_{\text{CEM}}+2G_{\text{CEM}}}{5G_{\text{CEM}}\left(K_{\text{CEM}}+\frac{4}{3}G_{\text{CEM}}\right)}\right)} \tag{2.1b}$$

The effective dry moduli K_{DC} and G_{DC} for a well-sorted disconnected patchy cement sandstone are calculated when an opposite coating relation is applied (i.e., HS lower bound):

$$K_{\text{DC}} = K_{\text{W}} + \frac{f_{\text{DC}}}{\left(K_{\text{CEM}} - K_{\text{W}}\right)^{-1} + (1 - f_{\text{DC}})\left(K_{\text{W}} + \frac{4}{3}G_{\text{W}}\right)^{-1}} \tag{2.2a}$$

$$G_{\text{DC}} = G_W + \frac{f_{\text{DC}}}{\left(G_{\text{CEM}} - G_W\right)^{-1} + 2(1 - f_{\text{DC}})\left(\frac{K_{\text{W}}+2G_{\text{W}}}{5G_{\text{W}}\left(K_{\text{W}}+\frac{4}{3}G_{\text{W}}\right)}\right)} \tag{2.2b}$$

The effective cement fractions f_{CC} and f_{DC} represent the volume fraction of stiff cemented sandstone in the binary mixture, varying between zero and one. The product of the cementation limit and connected effective cement fraction f_{CC} gives the cement volume V_{CEM} of the patchy cement sandstone:

$$V_{\text{CEM}} = f_{\text{CC}}\phi_{\text{CEM}} \tag{2.3}$$

Next, effective dry-rock bulk and shear moduli of patchy cement sandstone K_{dry} and G_{dry} at a smaller porosity ϕ can be obtained by interpolating between the well-sorted end member calculated at critical porosity and mineral point (zero porosity) using the modified lower HS bound (Avseth et al., 2010a) as a soft interpolator to account for varying porosity associated with sorting:

$$K_{\text{dry}} = \left[\frac{\frac{\phi}{\phi_c}}{K_{\text{PCM}} + \frac{4}{3}G_{\text{PCM}}} + \frac{1 - \frac{\phi}{\phi_c}}{K + \frac{4}{3}G_{\text{PCM}}} \right]^{-1} - \frac{4}{3}G_{\text{PCM}} \qquad (2.4a)$$

$$G_{\text{dry}} = \left[\frac{\frac{\phi}{\phi_c}}{G_{\text{PCM}} + z} + \frac{1 - \frac{\phi}{\phi_c}}{G + z} \right]^{-1} - z \qquad (2.4b)$$

where

$$z = \frac{G_{\text{PCM}}}{6} \left(\frac{9K_{\text{PCM}} + 8G_{\text{PCM}}}{K_{\text{PCM}} + 2G_{\text{PCM}}} \right) \qquad (2.5)$$

$$K_{\text{PCM}} = \begin{bmatrix} K_{\text{CC}} \\ K_{\text{DC}} \end{bmatrix} \qquad (2.6a)$$

$$G_{\text{PCM}} = \begin{bmatrix} G_{\text{CC}} \\ G_{\text{DC}} \end{bmatrix} \qquad (2.6b)$$

where K and G are the bulk and shear moduli of the grain material, respectively. The stress sensitivity of the patchy cement sandstone at a given porosity is obtained by varying the pressure σ' in the Walton model (see equation 2.10 in Appendix 2.A).
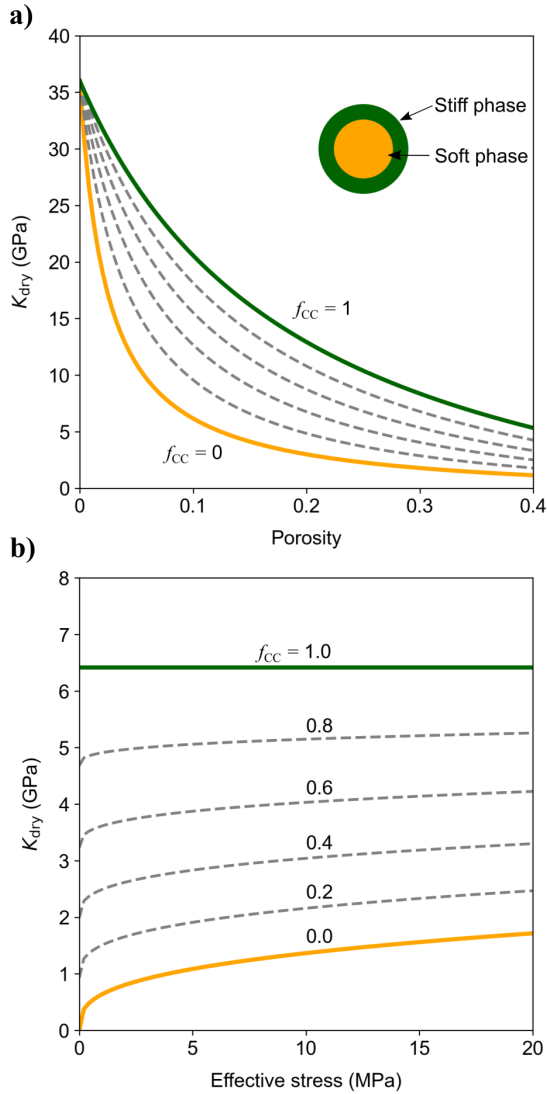
Figure 2.1: Rock physics modeling of connected patchy cement sandstone resulting from a stiff HS mixing of stress-sensitive unconsolidated sands (orange line) and stress-insensitive cemented sandstone (green line) with 10% contact cement. (a) Modeled dry bulk modulus versus porosity and the schematic representation of corresponding HS mixing. The effective stress is 10 MPa in this example. (b) Stress sensitivity curves computed by varying the effective stress in Hertz-Mindlin theory for porosity = 0.36.

Figure 2.1a shows the modeling results of PCM assuming connected patchy cement in the porosity and bulk modulus domain. Figure 2.1b shows a family of

stress sensitivity curves generated at a specific porosity with the lower bound being the stress sensitivity of unconsolidated sands and the upper constant bound representing the stress-insensitive nature of cemented sandstone modeled with the contact cement model. The results for disconnected patchy cement modeling are shown in Figure 2.2.
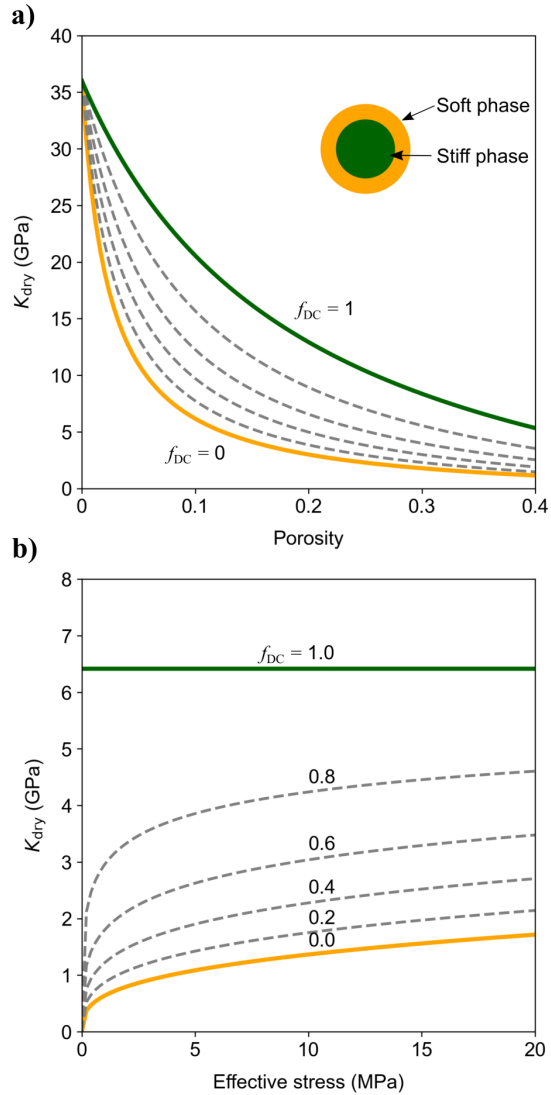
Figure 2.2: Rock physics modeling of disconnected patchy cement sandstone resulting from a soft HS mixing with the effective cement fraction f_{DC} varying from zero to one. The results are quite different if we assume connected versus disconnected patchy cement.

The modeling results presented in Figure 2.1 and 2.2 assume that the grain and cement materials are quartz with a bulk modulus $K = 36$ GPa, shear modulus $G = 42$ GPa, and a density of 2.65 g/cm³. The coordination number C is assumed to be 6, the critical porosity $\phi_c = 0.4$, and the slip factor $f = 0$.

2.2.2 Varying patchiness cement model

Microcracks play an important role in the stiffness degradation of cemented sandstone. The presence of cement can prevent the shatter and cracking of grains by reducing the stress concentration (Bernabé et al., 1992; Yin and Dvorkin, 1994; Dvorkin and Yin, 1995). Upon continuing stress release, the rock expansion driven by the grain residual compressive stresses is counteracted by the cement. The cement can be eventually broken when the tensile strength of cement reaches its limit (Bredesen et al., 2019). Instead of putting cracks through an inclusion-based model in the effective medium, we derive the premise that breaking of the contact cement bound during stress release can be viewed as a process in which the connected patchy cement is progressively replaced by disconnected patchy cement, which we call *diluting*. Figure 2.3 shows the conceptualization of our modeling approach.

As shown in Figure 2.3a, the grain contact cement is initially bonded together, forming bridge-like cement that connects individual grains and stabilizes the whole frame before unloading. This can be readily represented by the connected PCM of which geometric information regarding the cement and grains is shown in Figure 2.3b. As the stress is being removed, microcracks start to develop within the contact cement, as shown in Figure 2.3c, which will greatly reduce the connectivity and stability of the cement structure, thus softening the rock. The idealized model of the corresponding disconnected patchy cement sandstone is shown in Figure 2.3d. Note that the bulky cement is cracked into clustered cement. The red and blue lines shown in Figure 2.3e are the stress sensitivity curves calculated

using PCM, assuming connected patchy cement and disconnected patchy cement, respectively. The difference between these two curves contains rich information about the development of microcracks in patchy cement structure. For a given effective stress, the actual rock stiffness close to the upper bound will correspond to a stiff patchy cemented sandstone, whereas proximity to the lower bound will indicate a soft patchy cemented sandstone. The movement from the upper bound to lower bound with stress decrements indicates a dynamic process in which microcracks are developing (open or closure of microcracks) in the initially intact patchy cement network. It indicates that the cohesion of the cement structure is destroyed gradually by the stress release.
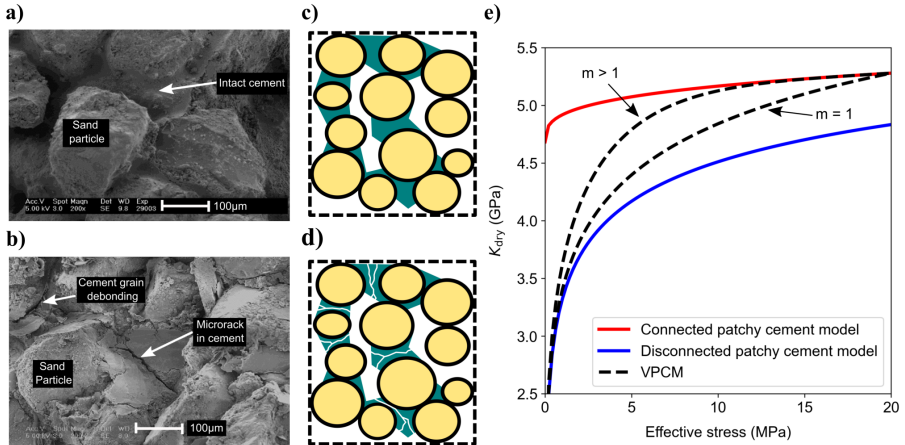
Figure 2.3: Physical interpretation of VPCM in terms of the possible variation of microgeometry. (a) Scanning electron microscope micrographs showing the artificial weakly silica-cemented sandstone with intact cement network before unloading and (b) cement breakage due to stress unloading; adapted from Alvarado et al. (2012). (c) Schematic representations of idealized connected PCM and (d) disconnected PCM. (e) The dashed black lines depict the modeling result of VPCM using different curvature parameters m. The red and blue lines are stress sensitivities computed from connected PCM and disconnected PCM, respectively. The red line corresponds to the stress sensitivity line with $f_{CC} = 0.8$ in Figure 2.1b. The blue line corresponds to the stress sensitivity line with $f_{DC} = 0.8$ in Figure 2.2b. The modeling is shown for porosity = 0.36.

This physical interpretation in terms of the possible variation of microgeometry

provides a possibility to model the increasing stress sensitivity upon stress release observed in high-porosity cemented sandstone. Mathematically, PCM can be extended to VPCM by introducing an *ad hoc* diluting parameter α to account for the increase of stress sensitivity when the effective stress is progressively removed. The elasticities given by VPCM at high-porosity end member are:

$$K_{\mathrm{VPCM}} = K_{\mathrm{CC}} - \alpha(K_{\mathrm{CC}} - K_{\mathrm{DC}}) \tag{2.7a}$$

$$G_{\mathrm{VPCM}} = G_{\mathrm{CC}} - \alpha(G_{\mathrm{CC}} - G_{\mathrm{DC}}) \tag{2.7b}$$

The effective dry rock moduli at smaller porosity are again computed using equations 2.4 - 2.6 with K_{PCM}, G_{PCM} replaced with K_{VPCM} and G_{VPCM}. The diluting factor α quantifies how much of connected patchy cement has been replaced by disconnected patchy cement upon stress unloading. It is allowed to be stress-dependent by

$$\alpha = \left(1 - \frac{\sigma'}{\sigma_0'}\right)^m \tag{2.8}$$

where the in situ effective stress σ' is the difference between the total stress and pore pressure, i.e., $\sigma' = \sigma - p_f$ assuming Biot coefficient equals unity (Fjaer, 2006). Here, σ_0' is a reference effective stress at which unloading begins and this stress can be related to the hydrostatic net stress of the reservoir rock before any stress perturbation caused by, e.g., fluid injection or uplift. For laboratory measurements, this stress corresponds to the maximum loading stress. Here, m is the curvature parameter that defines diluting rate. An example of VPCM for porosity = 36% is depicted as the dashed line in Figure 2.3e. Similar to the widely applied bound averaging methods (Hill, 1963; Marion, 1990; Marion and Nur, 1991; Avseth et al., 2010b, 2016), equations 2.7 and 2.8 compute a stress-dependent weighting average of the stress sensitivity of connected and disconnected patchy cement sandstones.

As shown in Figure 2.3e, when $m > 1$, VPCM mimics the case in which the rock exhibits certain reversible behavior at the early stage of unloading by being insensitive to stress changes, followed by an increasing softening upon extensive unloading. Such behavior is observed in the glass bead sample presented in the subsequent section. More information about the effect of m is included in the "Modeling results" and "Discussion" sections.

2.2.3 Cement crumbling

Several works report the production of grain fines by grain crushing in unconsolidated sands during tension and shearing (see Figure 5 of Andò et al. (2013) and Figure 5 of Chuhan et al. (2002)). Kozhagulova et al. (2020) examine how the mechanical behavior of weak artificial sandstone is altered by the bond breakage of the cement and conclude that the cement bond breakage constitutes the main mechanism for the deterioration of the sandstone strength. Wang and Leung (2008) characterize the effect of cementation on the sandstone mechanical properties using Particle Flow Code (PFC) simulation. It is found that the cement bond breakage can lead to the formation of bonded clusters and decemented grains, which are detached from the cement bond network. It also is observed in samples that the cement can be broken into chips filling the pore space (see Figure 10 in Kozhagulova et al. (2018)). This observed cement crumbling not only indicates the irreversible damage to the structure of the rock by stress release but also represents a snapshot of the deterioration of cemented sandstone being transformed from structure-dominated material to friction-dominated material. The geometric details of cement crumbling and the idealized model for patchy cement sandstone are shown in Figure 2.4a and 2.4b, respectively. Cement crumbling represents somewhat the displacement of cement through which contact cement changes to pore-filling cement. Thus, the porosity in the modeling is assumed unchanged.

The cement crumbling effect can be incorporated into the VPCM when the ce-

ment fraction parameter f_{DC} used to compute disconnected patchy cement end member is smaller than the f_{CC} for connected patchy cement end member. The physical explanation is that chipped cement filling the pore space will no longer be regarded as part of the load-bearing structure. Thus, the effective cement amount is reduced. As shown in Figure 2.4c, a larger stress sensitivity is modeled using VPCM through cement crumbling, and the stiffness of the rock is further reduced upon stress release. The amount of crumbled cement can be calculated via

$$V_{Crh} = (f_{CC} - f_{DC})V_{CEM} \qquad (2.9)$$

Notice that V_{Crh} is nonzero when $f_{CC} > f_{DC}$. Cement crumbling is muted for full diluting ($f_{CC} = f_{DC}$) and partial diluting ($f_{CC} < f_{DC}$).
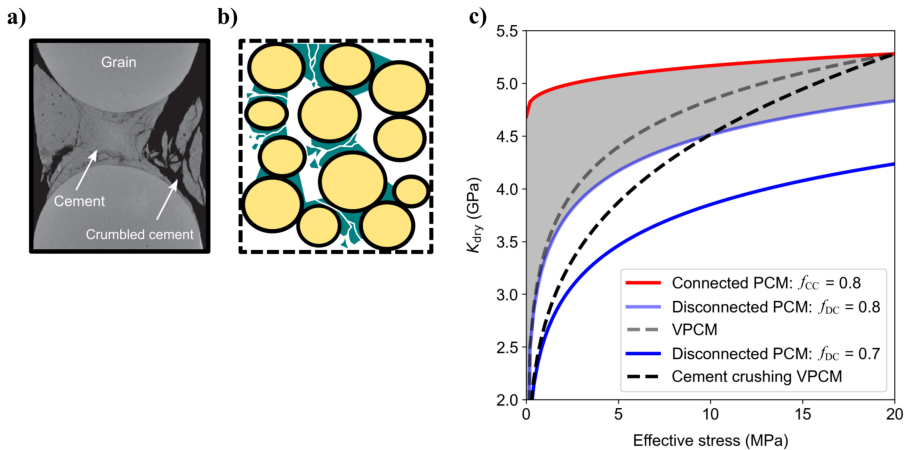
Figure 2.4: VPCM for cement crumbling and its idealized model. (a) Schematic representation of cement crumbling of single cement bond (Tengattini et al., 2014). (b) Idealized model sketch. Chipped cement detaches from the cement network and fills the pore space. This represents the further degradation of cement cohesion in the cemented sandstone. (c)Modeling result of cement crumbling in VPCM. Note that the crumbling of the cement contributes to the enlarged pressure sensitivity in addition to microcrack generation.

2.3 Sequential model calibration

The application of VPCM requires the calibration of PCM: given the cement volume VCEM and porosity ϕ of the sandstone, PCM assuming connected patchy cement (equations 2.1,2.3, 2.4 - 2.6, and 2.10 - 2.14) is first calibrated to post-cementation loading data (velocity or stiffness variation with effective stress) to determine the optimal choice of cement sandstone fraction f_{CC} and the slip factor f for shear correction. Then, these two output parameters from the calibration of PCM are used as input to VPCM (equations 2.2, 2.7 and 2.8). VPCM is subsequently calibrated to the unloading data given the reference stress σ'_0 to obtain the optimal choice of f_{DC} and positive curvature parameter m.

Given the fact that the effective cement fractions f_{CC} and f_{DC} and the slip factor f are bounded within zero and one, the trust region reflective method (Branch et al., 1999) is used as an optimization method in the PCM-VPCM modeling sequence because it is robust and able to determine the model parameters within predefined bounds. The implementation of the trust region reflective method is available in Virtanen et al. (2020).

2.4 Experimental data sets

The model performance is evaluated using one published experimental data set of cemented glass bead from Langlois and Jia (2014) and a data set generated at SINTEF that aims to investigate the unloading effect on the elastic behavior and damage of synthetic weakly cemented sandstone (Torset et al., 2021).

In the experiment by Langlois and Jia (2014), the glass beads have uniform grain diameter of 0.7 mm, with density = 2.45 g/cm^3, shear modulus = 26.2 GPa, and Poisson's ratio = 0.28. The cemented granular media are formed using a thermally controlled cementation strategy: first, the grains are evenly wetted with

tetradecane and then the oedometric cell containing the wet pack loaded under a predefined uniaxial stress P(0) is placed inside a refrigerator in which the temperature is lowered homogeneously below the freezing point of the tetradecane. The initial porosity of wet pack is 38%. The coordination number C $\approx$ 6 is chosen by Langlois and Jia (2014) according to Makse et al. (2004). Note that the experiment still simulates a dry pack as the wet pack is transformed into cemented pack during cooling. The solid tetradecane has density = 0.8 g/cm^3, shear modulus = 1.1 GPa, and Poisson's ratio = 0.34. The amount of frozen cement is approximately 0.65of 40±20 kPa and 1240±20 kPa. The cemented pack is then subjected to a cycle of uniaxial strain loading and unloading.

The other experimental data set originates from a series of coring tests on artificial sandstone performed at SINTEF (Holt et al., 2000, 2014). The sample is fine-grained loose sand with an average grain diameter of 0.04 mm and a wide grain-size distribution, which causes the initial porosity of the sand packing to be approximately 33%. This is smaller than the random dense packing porosity of 36%. The coordination number is 9 in the modeling in Torset et al. (2021). The dry synthetic sandstone is manufactured through a chemically controlled cementation strategy: the mixture of sand pack with a small amount of sodium silicate solution is flushed with carbon dioxide under a high predefined stress level (15 MPa axial stress and 7.5 MPa radial stress), mimicking sandstone cemented with quartz cement at typical reservoir settings. The sand grains are hardened when the cement agent reacts chemically with the CO_2, which causes amorphous silica to precipitate as grain contact cement. After the cementation, the sample is continuously loaded to the maximum stress of 40 MPa and then unloaded to 7.5 MPa. The loading and unloading after cementation are performed uniaxially with no radial deformation. The cement volume given in Torset et al. (2021) is 1.6%. The grain and cement properties are the same as quartz with density = 2.65 g/cm^3, shear modulus = 36 GPa, and Poisson's ratio = 0.08.

The elastic properties of the cement are different in the two experiments. The cement is much softer than the grain in the thermally controlled cementation experiment, whereas the stiffnesses of the cement are comparable to those of the grain in the chemically controlled experiment. For simplicity, we label the former as a soft cement experiment and the latter as a stiff cement experiment.

When performing contact cement modeling, it also is critical to determine the cement scheme. According to Dvorkin and Nur (1996), the radius of the contact cement layer is related to the cement distribution. There are two types of contact cement deposition: scheme 1 is representative of the case in which cement only precipitates at grain-grain contacts, and scheme 2 indicates that cement distributes evenly on the grain surface (see Figure 5.5.6 in Mavko et al. (2020)). Langlois and Jia (2014) point out that the capillary liquid is mainly accumulated at bead contact for the soft cement experiment, with only a small amount of wetting liquid attracted by the asperities at the grain surface. The cemented contact radius as a function of cement saturation for such cement distribution is very close to the scheme 1 cement deposition (see the numerical simulation in Langlois and Jia (2014)). As a result, scheme 1 is chosen when modeling the soft cement data in this work.

The stiff cement experiment aims to mimic the natural quartz cementation of reservoir rock. McBride (1989) mentions that it is common for quartz cement and overgrowth to precipitate around the grains in sandstones. The coating cement (scheme 2) is usually applied by default in rock physics modeling of sandstones (Avseth et al., 2014; Lehocki and Avseth, 2021). Accordingly, scheme 2 is selected for recreating the silica cement experimental data in this work.

2.5 Modeling results

2.5.1 Soft cement

Figure 2.5 shows the modeled P-wave velocities and acoustic measurements for a cycle of loading and unloading of the synthetic cemented glass bead pack manufactured under different prestress P(0). For a better comparison of the stress sensitivity variation, the P-wave velocity measurements are normalized with respect to the velocity measured under the maximum loading stress. The predictions from rock physics modeling also are normalized to the maximum modeled P-wave velocities. During loading, the cemented pack shows a weak stress sensitivity that is well captured by PCM. As shown in Figure 2.5a, the sample formed under low stress shows a slightly reversible behavior at the beginning of unloading preceding an irreversible reduction of the P-wave velocity, whereas the velocity of the glass bead pack prepared at higher stress (Figure 2.5b) starts to decrease at the beginning of unloading followed by a drastic velocity decrease. In both cases, the VPCM agrees reasonably well with the observations. The optimal choices for modeling parameters are tabulated in Table 2.1.

2.5.2 Stiff cement

Figure 2.6 shows the evolution of axial P-wave velocities for the synthetic sandstone with silica cement during post-cementation loading and unloading. The displayed P-wave velocities also are normalized. During the stage of loading from 7.5 MPa to 40 MPa, the stiff cement sample shows more pronounced stress sensitivity than the soft cement samples. The increased stress sensitivity also is observed upon unloading. Again, PCM and VPCM successfully explain the stress sensitivities in the sample observed during the stage of loading and unloading, respectively. Table 2.1 provides the optimal choices of modeling parameters.

Table 2.1: The optimal parameters from sequential calibration of PCM and VPCM using trust region reflective method. Notice that for the stiff cement sample, the critical cement limit ϕ_{CEM} assumed in Torset et al. (2021) is 6%, which is comparable with 6.54% in this study.

	f_{CC} (frac)	f_{DC} (frac)	Slip factor f	Curvature m	Diluting degree	$V_{\mathrm{Crh}}(\%)$	$\phi_{\mathrm{CEM}}(\%)$	$V_{\mathrm{CEM}}(\%)$
Soft cement sample low prestress	0.739	0.840	7.68e-16	4.233	Partial diluting	0	0.879	0.065
Soft cement sample high prestress	0.787	0.708	0.134	1.611	Cement crumbling	9.92	0.826	0.065
Stiff cement sample	0.245	9.6e-18	0.611	1.83	Cement crumbling	99.9	6.54	1.6
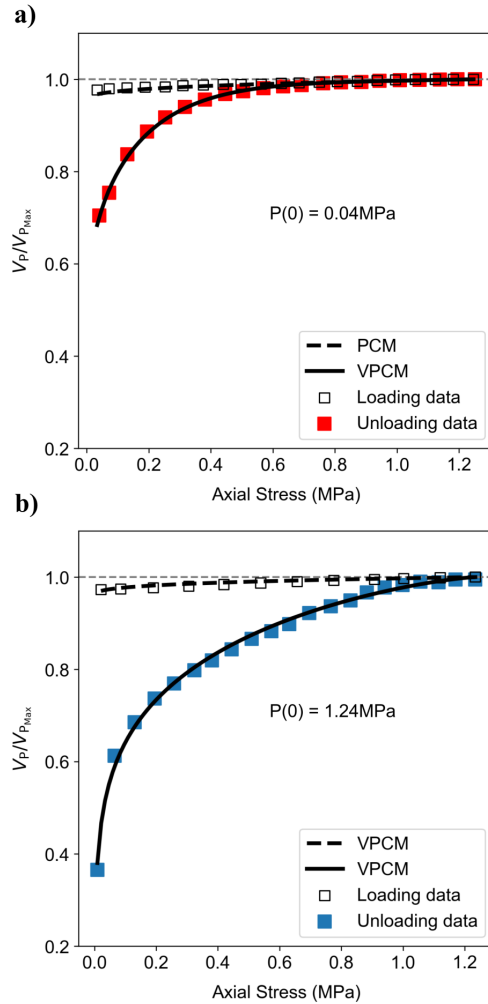
Figure 2.5: Normalized model predictions and measured P-wave velocities as a function of stress for tetradecane-cemented glass bead pack prepared (a) under low stress with measured $V_{PMax} = 1912.5$ m/s and (b) under high stress with $V_{PMax} = 1994$ m/s.
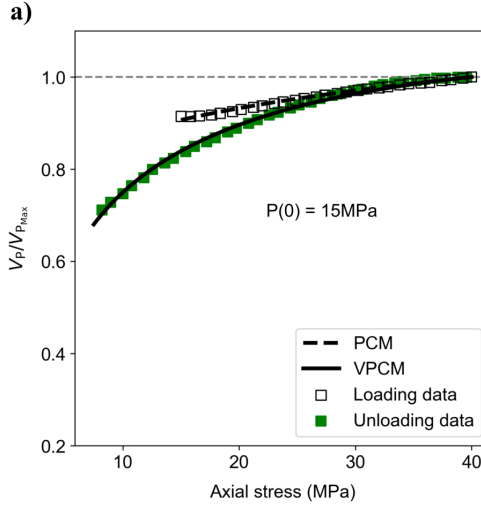
Figure 2.6: Model predictions and the evolution of normalized P-wave velocities measured for silica-cemented sandstone during post-cementation loading and unloading. The measured $V_{\mathrm{P}Max} = 2340$ m/s.

2.6   Discussion

The PCM has been extended to VPCM by stress-dependent diluting. VPCM aims to explain and quantify the increasing stress sensitivity of P-wave velocities observed upon stress unloading in high-porosity cemented sandstones. It has been shown that the combination of PCM and VPCM is able to match very well with measured P-wave velocities in high-porosity cemented grain pack and sandstone manufactured at different forming stresses with different types and amounts of cement.

Contact cement significantly contributes to the contact stiffness (Dvorkin and Nur, 1996). The connected effective cement fraction f_{CC} and slip factor determined through PCM calibration reflect the combined contributions from cement and forming stress to rock stiffness. In the soft cement experiment, samples have the same amount of cement, but the effective cement fraction f_{CC} is higher for the sample with high forming stress than for the sample with low forming stress (Table 2.1).

The slip factor is nearly zero for the low-prestress sample, whereas the high-prestress sample has a slightly larger slip factor given the same cement amount. The silica cement sample prepared under much higher stress with more cement yields a slip factor larger than 0.5 (see Table 2.1). It indicates that the slip factor shows a good correlation with the cementation and stress at which cement deposits. The stress-dependent behavior of the slip factor is reported in the literature (Bachrach and Avseth, 2008; Ahmed and Lebedev, 2019). Although the slip factor is devised to fix the nonaffine assumption in effective medium theory in the shear modulus prediction of loose sand, we can see that it also can be used to indicate how well the grains are locked in a cemented granular pack. Note that the coordination number also is reported to be stress-dependent (Dutta et al., 2010), but it is canceled out in equation 17 in Bachrach and Avseth (2008).

In this work, the velocity decrease during the stage of unloading is attributed to the cement weakening. The stress-dependent diluting in VPCM simulates the breaking of the cement bond by replacing connected patchy cement sandstone with disconnected patchy cement sandstone as the stress is progressively removed. The effective cement fraction f_{DC} determines the elasticity of the disconnected patchy cement sandstone, thus representing the stage to which the sandstone evolves during stress release. For instance, both low and high-prestress samples experience a decrease in velocity after unloading, with reductions of more than 30% and 60%, respectively. Despite these reductions, the velocities of both samples remain nonzero when the applied stress is completely removed. This suggests that the grain packing remains coherent despite partial cement debonding (Langlois and Jia, 2014) induced by stress release. In this case, f_{DC} derived from these soft cement samples is larger than zero. In contrast, for the stiff cement sample (Figure 2.6), f_{DC} derived from VPCM is very close to zero indicating significant damage to the sample during unloading, and the stress sensitivity of the sample will be close to unconsolidated sands as the bonding effect from cement vanishes

(Vcrh closes to 100%). This agrees with the fact that the velocity measurements in the cemented sandstone are approaching its pre-cementation measurements upon unloading (see Figure 3 in Torset et al. (2021)). From these interpretations, we suspect that the diluting degree and the exact value of f_{DC} provide a way to infer the structural coherence of the sample. That is to say if f_{DC} is nonzero in VPCM, the stiff connected patchy cement sandstone is evolving to a less-stiff disconnected cemented sandstone. In contrast, if f_{DC} is zero, it indicates that microcracks have severely affected the cement network such that the cemented sandstone tends to behave similarly to unconsolidated sands with Hertzian stress sensitivity.

Note that the last velocity measurement at the end of unloading shown in Figure 2.5b is much smaller than its prior sampling point indicating an accelerating deterioration of the grain packing stiffness. Surprisingly, VPCM successfully predicts this tendency. In VPCM, the curvature m is allowed to control the cement debonding rate. Figure 2.5a shows that the P-wave velocity of the low-stress sample exhibits a less rapid change with stress at the initial stage of unloading followed by a rapid decrease upon further unloading. As the forming stress increases (Figure 2.5a, b and 2.6), the curvature parameter m becomes close to one (Table 2.1), indicating that the cement debonding becomes increasingly more linearly dependent on stress. A similar failure behavior of weakly cemented sandstone also is reported in previous work. E.g., numerical simulation in Kozhagulova et al. (2020) shows that the rate of bond breakage in samples of lower confining pressure indicates an evident speed transition, which will become less distinct for high confining pressure.

The samples are dry in both soft and stiff cement experiments. The proposed model can be combined with Gassmann (1951) theory to compute elastic moduli and low-frequency wave velocities of the saturated rocks. At high frequencies, the unequalized pore pressure between cracks and pores can cause frame stiffening in fluid-saturated porous media with embedded cracks upon stress load-

ing (Mavko and Jizba, 1991; Mavko and Nolen-Hoeksema, 1994; Müller et al., 2010; Zhang et al., 2021, 2022); Winkler (1983) observes that the brine-saturated high-porosity sandstone shows the opposite sign of dispersion compared with dry samples. Tillotson et al. (2012) observe that the P-wave attenuation of artificially high-porosity (30%) silica-cemented sandstone upon unloading is different from loading, and the difference results from hysteresis. The cement weakening effect on the velocity dispersion and attenuation remains less understood, hence future works should consider how effective stress release will influence the short-wavelength wave propagation through saturated high-porosity porous media in addition to the well-studied effects, such as saturation state and fluid properties.

This work exclusively is concerned with measurements of artificial samples, which are oversimplifications of real rocks. The soft cement sample has relatively uniform grain size, and frozen tetradecane is not analogous to the natural cementation. Compared to the soft cement sample, the stiff cement sample is a fair representation of the quartz-dominated sandstones. The quartz grains are sourced from real sediments. The cementation is allowed to happen under a stress level that is comparable with in situ reservoir state, and the stress path is selected to be representative of those occurring in reservoir rocks. Different samples generated by using the same cementation strategy are presented in Holt and Stenebråten (2013). It is found that the synthetic sample has properties mimicking those of real rock in terms of mechanical, petrophysical, visual, and acoustic characteristics. Future experimental design could investigate the impact of varying mineralogy and lithology on stress sensitivity to stress reduction.

It has been demonstrated that by assuming cement bond breakage and reduction in effective cement amount, VPCM is able to capture the significant velocity decrease resulting from the effective stress reduction. According to Terzaghi's law, effective stress release can be associated with an increase in pore pressure when the overburden stress remains unchanged. This is typical for a fluid injection scenario

if the pore pressure is not properly maintained. Previous studies have reported that 4D seismic response around high-pressure injectors cannot be explained by classical models that only consider fluid saturation and pressure changes (Duffaut et al., 2011; Saul and Lumley, 2015). Al Hosni et al. (2016) also show that 4D crosswell data of CO_2 injection into weakly cemented Frio sandstones can be better interpreted by assuming the reduction in contact-cement percent in the chosen rock physics model. The ability of VPCM to model the asymmetrical sensitivity of sandstone velocities to stress decrease due to the weakening of rock frame can help the interpretation of 4D seismic attributes of fluid injection monitoring and fluid saturation estimation. In practice, VPCM can be repeatedly calibrated using newly acquired monitoring data. The resulting f_{DC} value, as discussed previously, indicates the coherence of rock frame. When the value is approaching zero, it indicates a high level of injection risk because the cemented rock frame might have been significantly damaged by injection.

The proposed model is rooted in isotropic linear elasticity with the inherent limitations and caveats of grain contact models and bound filling models (see Mavko et al., 2020). The nonlinearities exhibited by the initiation and evolution of microcracks are mitigated and approximated by the diluting process in the VPCM model. In material science, fatigue theory is widely used to treat stress cycling-induced excessive rock deformation (Marigo, 1985; Newman, 1998; Suresh, 1998). When the stress is repeatedly released and reapplied, the material may eventually fail due to the accumulation of damage in each loading-unloading stress cycle. The number of stress cycles required for fatigue failure varies greatly from 1 up to millions and more depending on the magnitude of applied stress and material strength (Newman et al., 1999; Caputo and Carcione, 2011). Although this work studies the first unloading cycle, the microcrack generation during this single unloading step can be part of a complete fatigue life.

The proposed model works well for high-porosity cemented sandstone. When the

rock becomes heavily cemented (e.g., cement >10%), increasing cement model (Avseth et al., 2010a) can be introduced to PCM to circumvent the limitation of the contact cement model. Only axial P-wave velocities are used in this work due to the isotropic assumption of the model. Nevertheless, the applicability of the modeling is not greatly limited to field application because the stress-induced anisotropy in sandstone is considered weak (Thomsen et al., 1993). The input parameters, such as the amount of cement, coordination number, and grain moduli, are known for soft and stiff cement samples present in this work but might not be always available and often are very difficult to obtain. Empirical relationships among coordination numbers, porosity, and stress can be applied (Murphy, 1982; García and Medina, 2006; Dutta et al., 2010; Mavko et al., 2020). In practice, the cement and grain properties can be estimated from petrophysical logs and core quantification to narrow the uncertainty related to the choice of these parameters.

PCM and VPCM assume that microcracks are distributed randomly in the effective medium considering the structural heterogeneity of the granular medium, unknown spatial distribution of cement, and coupling of shear and tensile failure (Fjaer, 2006). However, this assumption will be violated if the rock develops global failure, e.g., rock core discing by coring (Holt et al., 2000; Fairhurst, 2003) and horizontal fracturing due to severe uplift (Flottmann et al., 2004).

2.7   Conclusion

A new rock physics model has been proposed for high-porosity cemented sandstone to describe the deterioration of the stiffness as stress is gradually removed. Unlike inclusion-based and pore shape models, the softening of the cement is described by the stress-dependent diluting, i.e., replacement of connected patchy cement sandstone by disconnected cement sandstone. The cement crumbling is identified and modeled as an additional source of the increasing stress sensitivity upon stress release at a grain-scale level. The model prediction is compared with axial P-wave

velocity data measured for artificial cemented glass bead pack and sandstone. Despite the pragmatic nature, the model recreates the experimental measurements very well. The sequential calibration workflow acts as a tool to quantify the velocity evolution with effective stress in target sandstone. The parameters derived through the sequential calibration have physical implications about the coherence of the rock, which is likely to provide early warning of the unexpected collapse of the high-porosity cemented sandstone upon stress release and facilitate the underground pressure maintenance in practice. The modeling workflow also can be useful in predicting velocities affected by the combined effect of overpressure and fluid effect in time-lapsed monitoring of fluid injection projects.

2.8   Acknowledgments

2.A   Walton contact theory and shear correction

Walton (1987) contact theory can be formulated as two limits: no-slip limit for grains with infinite friction and slip limit for grains without friction. The effective bulk modulus is identical for the limits and given by

$$K_{\mathrm{W}} = \frac{1}{6} \left[\frac{3(1-\phi)^2 C^2 \sigma'}{\pi^4 B^2} \right]^{1/3} \tag{2.10}$$

where C is the coordination number, ϕ is the porosity, and σ' is the effective stress. B is defined as

$$B = \frac{1}{4\pi} \left(\frac{1}{G} + \frac{1}{G + \lambda} \right) \tag{2.11}$$

where λ is the Lamé's coefficient of the grain material. The effective shear modulus for slip limit is given by

$$G_{slip} = \frac{3}{5} K_{\mathrm{W}} \tag{2.12}$$

For nonslip limit,

$$G_{non-slip} = \frac{3(5 - 4\nu)}{5(2 - \nu)} K_{\mathrm{W}} \tag{2.13}$$

where ν is the Poisson's ratio of the grain material.

The shear correction from Bachrach and Avseth (2008) is applied to account for the loose contact in the grain assembly. Finally, the effective shear modulus used in this work is

$$G_{\mathrm{W}} = (1 - f)G_{slip} + f G_{non-slip} \tag{2.14}$$

where f is the slip factor.

CHAPTER 3

UNDERSTANDING THE SYNERGISTIC IMPACT OF STRESS RELEASE AND CEMENTATION ON SANDSTONE USING SOUND WAVES — IMPLICATIONS FOR EXHUMATION ESTIMATION

ABSTRACT:

Exhumation is the process that encompasses both uplift and erosion, leading to the removal of overburden and the release of effective stress exerted on rocks. When estimating exhumation magnitude using the compaction trend method, it is commonly assumed that the physical properties of rocks are insensitive to stress reduction. However, recent laboratory evidence has shown that porosity exhibits weaker sensitivity to stress release compared to velocity which can be significantly affected by stress release. This raises uncertainties regarding the assumption of irreversible compaction. It remains unclear whether the impact of stress release can be observed in real rocks in exhumed areas, as there is a lack of methods to directly measure the impact of stress release on field data. Additionally, studying real rocks is further complicated by the presence of rock diagenesis and its interaction with stress release. To address these knowledge gaps, this study employs stress-dependent burial and uplift modeling and interprets an extensive well-log dataset using the modeling-derived evaluation metrics. Conceptual modeling suggests that the velocity depth trend method tends to underestimate exhumation magnitude when the combined effect of cementation and stress release on rock elastic properties is neglected. Furthermore, we discover that the disparity between porosity sensitivity and velocity sensitivity to stress release can be leveraged to derive a metric *porosity inconsistency* which can serve as both a qualitative and quantitative measure for identifying and evaluating stress release in sandstone using geophysical field measurements. We have gathered a significant amount of sonic velocity and porosity data from normally compacted and uplifted clean sandstones in the Norwegian Sea and the Barents Sea. Notably, we observe significant porosity inconsistency in the exhumed well 6510/2-1 in the Norwegian Sea. In the Barents Sea, which has experienced extensive Cenozoic exhumation, the well data reveals a varying pattern of porosity inconsistency increasing towards the north

and decreasing towards the west. This distribution of porosity inconsistencies in Barents Sea wells not only aligns with the spatial variation of exhumation reported in various studies but also exhibits a positive correlation with the magnitude of exhumation. Furthermore, the exhumation magnitude derived from velocity-depth trends is considerably lower than the magnitude obtained from porosity/density-depth trends for wells displaying significant porosity inconsistency. These observations provide support for the predictions made by the conceptual modeling. The results of this study enhance our understanding of the synergistic impact of stress release and cementation on sandstone. Moreover, these findings have implications for pore pressure prediction and core evaluation in exhumed areas. They also provide insights into the feasibility and interpretation of time-lapse data of reservoir injection, where the effective stress is likely to decrease due to pore pressure buildup. When estimating the magnitude of exhumation using the compaction trend method, velocity and porosity are usually assumed to be stress-insensitive as the rock is uplifted from the maximum burial to the surface. The degree of stress release associated with uplift is assumed negligible by default and hardly ever quantified from field data. By performing conceptual rock physics modeling honoring the burial history, a simple diagnostic approach is proposed to study the exhumation-cementation-velocity interplay and its impact on exhumation estimation. The approach is based on the difference between the velocity stress sensitivity and porosity stress sensitivity upon stress release. By utilizing the regional reference porosity and velocity depth trends, porosity inconsistency, a quantitative measure of the average stress release degree can be computed for uplifted rocks. P wave velocity and porosity data of normally compacted and uplifted clean sandstones in the Norwegian Sea and Barents Sea are analyzed using the diagnostic approach. Significant porosity inconsistency is observed in the well 6510/2-1 in the Norwegian Sea. In the Barents Sea, the data shows varying porosity inconsistency

that is positively correlated with increased exhumation towards the north and decreased exhumation towards the west. The porosity inconsistency and different estimations given by the porosity depth trend indicate the deteriorating effect on the rock velocity caused by uplift. The field data observations support the conceptual model prediction i.e., the velocity depth trend approach tends to underestimate exhumation magnitude under the assumption of irreversible compaction due to ignorance of stress release impact on the velocity.

3.1   Introduction

Exhumation is a term used to describe the integral effect of uplift and erosion on buried rocks relative to a datum (Lasabuda et al., 2021). Accurately estimating the magnitude of exhumation is crucial for assessing the hydrocarbon prospectivity in both onshore and offshore basins, as it significantly impacts various aspects, such as source rock maturation, structural stability of reservoirs, and migration pathways (Doré and Jensen, 1996; Henriksen et al., 2011). Practically, the parameter of interest is the net exhumation, which refers to the displacement of rocks along the depth axis from their maximum burial depth to their present-day burial depth (Corcoran and Doré, 2005). This definition coincides with the terms "net erosion" used in Henriksen et al. (2011) and "net uplift" used by Doré and Jensen (1996). In this study, exhumation is used as the descriptive term, and "uplift" is used per se to describe the elevation of the buried rocks when applicable. Comprehensive overviews of the estimation methodologies are available in the literature (Japsen and Chalmers, 2000; Corcoran and Doré, 2005; Lasabuda et al., 2021). Among the various estimation techniques, the compaction trend method is widely applied due to its simplicity, wide data availability, and independence of sample distortion (Corcoran and Doré, 2005).

Generally, the estimation of exhumation magnitude for a single well using the compaction trend method at a specific depth location can be summarized as fol-

lows: a Normal Compaction Trend (NCT) is established for a given lithology in an unexhumed area, representing the relationship between a rock property e.g., porosity and burial depth under hydrostatic conditions. This requires a significant number of core or sonic measurements spanning a wide depth range and currently buried at their maximum burial depth with normal pore pressure. Subsequently, the exhumation magnitude is estimated as the vertical offset between the NCT and the depth trend established using the data observed in the exhumed well.

A key assumption in this workflow is the irreversibility of compaction, meaning that the porosity (or its proxies) of the exhumed rock will remain unchanged from its state at maximum burial (Licciardi et al., 2020). Compaction is a diagenetic process that involves the reduction of sediment volume, resulting in increased rock stiffness and decreased porosity (Athy, 1930; Magara, 1980). There are two main types of compactions: mechanical and chemical. Mechanical compaction involves a decrease in rock volume due to increased compressive stress from mechanical processes. Chemical compaction, on the other hand, involves a reduction in rock volume due to chemical processes such as dissolution (Worden and Burley, 2003). Another important diagenetic process that significantly impacts rock properties is cementation i.e., the precipitation of minerals in the pore space. It's worth noting that some literature considers cementation as part of chemical compaction (Bjørlykke and Høeg, 1997; Avseth et al., 2010a). For the purpose of this study, a differentiation is made between cementation and chemical compaction. The removal of the overburden typically leads to a reduction in the effective stress exerted on the rock, which will be referred to as "stress release" herein in this work. If the poroelastic properties of rock are significantly altered by factors such as cementation and stress release during exhumation, the aforementioned NCT workflow may yield inaccurate estimations (Japsen and Chalmers, 2000; Al-Chalabi, 2001; Bredesen et al., 2019; Torset et al., 2021). Experimental and rock physics studies have indicated that porosity changes upon effective stress

release are generally modest (≈ 1 porosity unit) for overconsolidated sandstone (Luo and Vasseur, 1995; Giles et al., 1998; Dong et al., 2010; Holt et al., 2014; Wang et al., 2017a; Narongsirikul et al., 2019b), and varies for shale depending on the factors such as clay composition, organic matter content, temperature and diagenetic transformation of mineral phase, which influence the inelasticity of shale (Johnston, 1987; Katahara, 2006; Masri et al., 2014).

In contrast to porosity, velocity can greatly change as the effective stress is progressively released. Laboratory studies have shown that sandstones can exhibit strong asymmetries in the velocity stress gradient during stress loading and unloading due to the weakening of the cement bond upon stress release (Langlois and Jia, 2014; Torset et al., 2021). During exhumation, if a sandstone is cemented when the reduction of overburden begins, the cement will be subjected to tensile stress, which may eventually lead to brittle deformation and tensile fracturing (Bjørlykke and Jahren, 2010), even though the total stresses remain compressive (Holt et al., 2014). Such brittle deformation can significantly reduce velocity while only slightly affecting porosity. Indeed, cementation plays an important role in influencing the velocities of both sandstones and shales during compaction and stress release associated with uplift. As one of the most common types of cement in sandstones, quartz cementation begins when the temperature reaches around 70 – 90 °C (Avseth et al., 2010a). Within a similar temperature window, silica released from the smectite-to-illite conversion in shale diagenesis (Thyberg and Jahren, 2011) can precipitate as micro-quartz crystals which accelerates the stiffening of shale (Thyberg et al., 2009; Thyberg et al., 2010). According to Dvorkin and Nur (1996), even a tiny amount of cement at sand grain contacts can drastically increase velocity while causing almost no change to porosity. Similarly, shale diagenesis can lead to an increase in velocity without a significant change in density. A representative example can be found in Figure 4 of Thyberg et al. (2010): quartz cementation induced by clay minerals is indicated by an abrupt

change in the velocity-depth trend, while the corresponding density-depth trend does not exhibit a similarly sharp change.

Since cementation is temperature-dependent (Huang et al., 1993; Walderhaug, 1996), it will not cease unless the temperature drops below the threshold required for cementation to occur. Consequently, during uplift, if the rock remains within the temperature range suitable for cementation (referred to as the cementation window), a reduction in porosity and an increase in velocity can be anticipated.

In well-explored offshore areas, e.g., the North Sea, NCTs are commonly constructed based on compressional velocity data obtained from sonic transit time or shot gathers due to the wide availability of well logs and dense seismic arrays (Japsen, 1998; Baig et al., 2016; Olierook and Timms, 2016). These data have also facilitated the generation of regional exhumation magnitude maps (Tassone et al., 2014; Baig et al., 2016; Ktenas et al., 2019). However, rich literature employing velocity depth trends often overlooks the effect of stress release and its interplay with cementation during the exhumation process. Cementation and stress release are two distinct and competitive mechanisms that influence the elastic properties of rocks. Specifically, cementation stiffens the rock whereas stress release tends to weaken the rock. The combined effects of these two mechanisms on velocity can complicate the estimation of exhumation (See Figure 3.1 for further details). One of the challenges in investigating how the joint effect of cementation and exhumation influences rock velocity is the lack of a reliable indicator for assessing the degree of stress release in rocks (Al-Chalabi, 2001). Nevertheless, the distinct responses of porosity and velocity to stress release offer insights for a better understanding of the exhumation-cementation-velocity triangle. Getting that better understanding will be the main objective of this study. Specifically, the following questions will be addressed:

- Can stress release and cementation impact the estimation of the exhumation

magnitude using the velocity compaction trend method?

- How can the impact on the rocks and their velocity depth trend be diagnosed?

- Is the impact significant or negligible in practical terms?

- How to improve the estimation of exhumation magnitude using velocity depth trends?

Firstly, we perform a conceptual integrated rock physics modeling guided by burial history following a modeling strategy outlined in Torset et al. (2021). This modeling is aimed at extracting the different depth/stress dependencies of porosity and velocity during both burial and uplift, based on which a simple indicator is proposed to identify the presence of stress release. Next, an extensive well-log dataset collected from the Norwegian Sea and the Barents Sea is presented. The principles for selecting the wells and processing the data are also described in detail. This dataset then serves as the basis for establishing the normal compaction and uplift trends, as well as for verifying the modeling hypothesis. Finally, the observations from the well-log dataset are presented and thoroughly discussed in relation to the aforementioned research questions.

3.2   Porosity and velocity evolution with burial and uplift

Although the estimation of exhumation magnitude using compaction trends is primarily done for shale, this study will specifically focus on sandstone due to the following reasons:

The huge shaly sedimentary package in offshore basins generally motivates the use of data-driven empirical models for shale compaction and diagenesis (Avseth et

al., 2010a). However, there is a lack of deterministic rock physics models for shales that handle stress sensitivities as a function of various geological parameters (fabric, composition, etc.). The understanding of stress sensitivity in the shales during uplift is also limited (Holt et al., 2005). Furthermore, due to the low permeability, the time required for pore pressure equilibrium in a typical shale layer is usually in a geological time scale (Fjaer et al., 2008), and the disequilibrium compaction significantly contributes to overpressure development in thick shale sequences (Osborne and Swarbrick, 1997). Additionally, the illitization of smectite in shale also causes pore pressure build-up (Katahara, 2006; Meng et al., 2021), Therefore, it is quite challenging to isolate the effects of stress release and cementation in shale without considering the pore pressure. More importantly, the density of shales can vary significantly (Rider, 1986), and the density well logs are often unavailable for shaly intervals.

Rock physics combined with basin modeling provides a valuable approach for obtaining insights into the porosity and velocity evolution of sandstones. Avseth and Lehocki (2016) proposed a modeling scheme that can predict the variations of physical properties throughout the "life cycle" of sandstone, considering any given burial history. Torset et al. (2021) implement an integrated rock physics workflow, building upon the work of Lehocki and Avseth (2021), to simulate the velocity evolution of rock during a representative burial history. When modeling the stage of uplift, different models can be blended with the cementation model depending on the properties of the sandstone. For example, the crack model (Fjaer, 2006) is used in Torset et al. (2021) to capture the impact of stress release on soft sandstone with weakly cemented grain contacts. The differential effective medium (DEM) model (Avseth et al., 2014) is commingled with a cementation model in Bredesen et al. (2019) to simulate the effect of fracturing on the elastic properties of the well-cemented Kobbe Formation sandstone during uplift. In this study, the varying patchiness cement model proposed by Yu et al. (2023a) is used

for the uplift modeling. The model is suitable for describing weakly to moderately cemented sandstones, which are common reservoir rocks present in the Norwegian Sea and the Barents Sea.
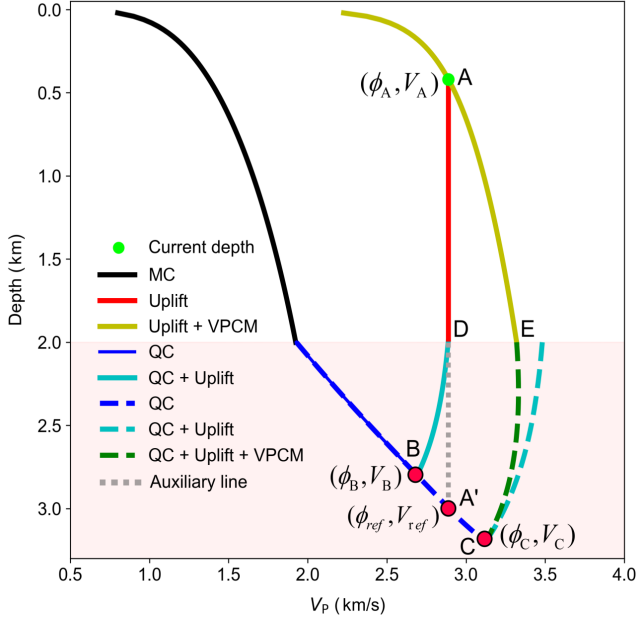
Figure 3.1: The conceptual modeling of P wave evolution through different stages of burial and uplift. The modeling strategy follows that of Torset et al. (2021). The degradation effect on velocity induced by uplift is modeled by using Varying Patchiness Cement Model (VPCM) as proposed by Yu et al. (2023a). The cementation begins when the rock is buried below 2 km in this example. The cementation window is shaded with light red color. The porosity and P wave velocity at point A' are denoted as ϕ_{ref} and V_{ref}, respectively. Whereas porosities and P wave velocities at locations A, B and C are distinguished by the corresponding subscripts. D and E mark the exit of the cementation window. When the rock is lifted outside the cementation window either from D to A or from E to A, cementation ceases and no longer impacts the rock. Note that the integration of the varying patchiness cement model with the cementation model (C – E) generates a depth trend of decreased velocity. The modeling result for subsequent uplift outside the cementation window (E – A) shows an increasing gradient of velocity reduction. Acronyms: MC: mechanical compaction; QC: quartz cementation.

Figure 3.1 illustrates the conceptual rock physics modeling of the P wave evolution guided by two predefined burial histories with different maximum burial depths. The complete modeling workflow and the input burial histories can be found in the

Appendices. Note that all depths indicated in the figures in this work are True Vertical Depth Below Sea Floor (TVD-BSF) unless otherwise stated. The red-shaded highlights the quartz cementation realm in which the cementation modeling is performed. Several important diagenetic processes defining the rock properties are simulated, including mechanical compaction after deposition (black), quartz cementation during burial (blue; blue dashed), continued quartz cementation during uplift (cyan; cyan dashed), and subsequent uplift outside the cementation realm without considering the stress release effect (red), combined effect of continued quartz cementation and stress release during uplift (green dashed), and subsequent uplift considering the effect of stress release effect (olive). The determination of the maximum burial depth directly controls the final net exhumation estimation. Figure 3.1 elucidates how the velocity NCT method can lead to incorrect interpretations of the maximum burial depth when cementation and stress release during uplift are disregarded. The figure highlights three associated cases, providing valuable insights into the complexities introduced by cementation and stress release on exhumation estimation:

- Case 1: According to the conventional NCT method, the apparent maximum burial is determined by projecting the current burial depth A vertically onto the reference velocity trend. Hence, the net exhumation estimate is obtained as the vertical offset between A and A′.

- Case 2: If the effect of cementation during burial is considered but the stress release does not affect the sandstone velocity during uplift, the actual maximum burial depth will be at B. The uplift modeling trajectory from maximum burial depth to the current depth follows the path B – D – A. In this case, the offset AA′ represents an apparent net exhumation estimate which overestimates the true magnitude—the vertical distance between A and B.

- Case 3: If the cemented sandstone undergoes weakening due to stress release associated with uplift, the rock at current depth location A may have been buried even deeper to location C. The corresponding uplift modeling trajectory from maximum burial depth to current depth follows the path C – E – A. This implies that the conventional NCT method will underestimate the net exhumation magnitude, as the vertical distance between A and C is larger than the vertical offset AA′. This finding aligns with the qualitative conclusion made by Torset et al. (2021).

The corresponding conceptual modeling results of porosity evolution and the amount of the quartz cement precipitation are shown in Figure 3.2a and 3.2b, respectively. By considering the variations in porosity as a cross-reference when applying the standard velocity depth compaction trend method, it becomes possible to discern the influence of stress release and assess its effect on the exhumation estimation in the velocity-depth domain. More specifically, the relative magnitude of porosity at current depth location A and its vertical counterpart A′ in the velocity depth trend serves as both an effective indicator and a diagnostic tool for evaluating the impact of stress release on the rock and its velocity depth trend.
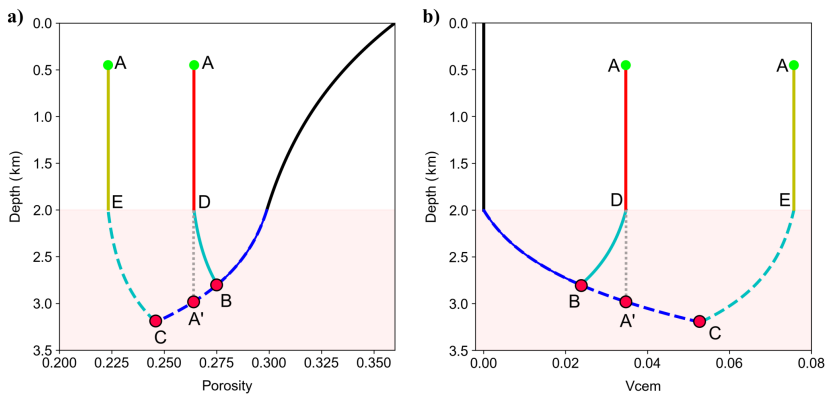

Figure 3.2: (a) Porosity evolution as a function of burial history. (b) The cumulative amount of intergranular quartz precipitation as the rock undergoes burial and uplift within the cementation window. The color coding, legend, and annotation are consistent with Figure 3.1.

The analysis is as follows: the assumption made in the conventional NCT method is that the rock elastic properties will remain the same as acquired at the maximum burial during the entire uplift. If this irreversible compaction assumption holds valid, it is expected to observe the porosity $\phi_A = \phi_{ref}$ at the current depth. Note that ϕ_{ref} refers to the porosity of the reference porosity depth trend at the depth that would have been predicted by the conventional velocity NCT.

If the rock experiences continued quartz cementation during uplift while the stress release effect is negligible, the rock's diagenetic history corresponds to case 2. In this case, as shown in Figure 3.2, the porosity at the true maximum burial point B (ϕ_B) is larger than the porosity at reference point A′ (ϕ_{ref}). However, the ongoing quartz cementation during uplift from B to D will further reduce the porosity, resulting in the same porosity value as at the reference point A′. During the subsequent uplift outside the cementation window, the porosity remains unchanged. Therefore, in this case, the resulting porosity at location A will still satisfy the relationship $\phi_A = \phi_{ref}$.

Conversely, in case 3 where cementation continues during uplift and rock is weakened by stress release, the porosities at locations A and A′ in the velocity–depth domain will not satisfy the relationship $\phi_A = \phi_{ref}$. This is explained by the following reasons: Firstly, the porosity ϕ_C at maximum burial C is smaller than ϕ_{ref}. Because the rock was buried deeper and experienced more quartz cementation. In addition, from maximum burial C to the cessation of cementation at point E, the rock undergoes continued quartz cementation, leading to a further reduction in porosity. Hence, the resulting porosity at current depth A will be smaller than the porosity at reference point A′, i.e., $\phi_A < \phi_{ref}$ in the velocity-depth domain. Notice that in all cases, the porosity variation is assumed negligible from the exit point (D and E) of the cementation window to the current depth A.

Table 1 presents a summary of the three cases together with the respective ve-

locity and porosity relationships between A and A′ in the velocity-depth domain. The above analysis highlights that porosity can be used as a stress release indicator when estimating the exhumation magnitude using the velocity depth trend. Specifically, if the porosity of the rock at the current depth location is smaller than that of the rock with the same velocity on the reference velocity depth trend, it is likely to indicate the P-wave velocity was affected by the stress release during exhumation. The exhumation magnitude will be thus underestimated.

Table 3.1: A summary of three cases and the corresponding diagnostics when estimating the net exhumation using the velocity compaction trend as shown in Figure 3.1.

Cases	Velocity	Porosity	Processes during uplift	NCT assumption
Case1	$V_A = V_{ref}$	$\phi_A = \phi_{ref}$	Cementation: no Stress release: no	Valid
Case2	$V_A = V_{ref}$	$\phi_A = \phi_{ref}$	Cementation: yes Stress release: no	Invalid
Case3	$V_A = V_{ref}$	$\phi_A < \phi_{ref}$	Cementation: yes Stress release: yes	Invalid

3.3 Dataset

In this study, well-log data from clean sandstones from the Barents Sea and the Norwegian Sea are compiled to investigate the combined effect of cementation and stress release on the exhumation estimation using velocity depth trends. The major part of the Barents Sea is believed to be greatly affected by the Cenozoic uplift and erosion (Ohm et al., 2008; Henriksen et al., 2011). The magnitude of the exhumation varies greatly, ranging from less than 100 m to more than 2000 m from west to east (Baig et al., 2016). The Stø formation forms a primary target reservoir rock present across the Barents Sea (Duran et al., 2013). It mainly contains

mature sandstone with quartz-rich detrital grains (Bergan and Knarud, 1993). Petrographically, the typical sub-arkose sandstones in the Stø formation show a favorable comparison to their equivalents in the Norwegian Sea, especially the middle Jurassic sandstones (Ehrenberg, 1990; Henriksen et al., 2011). Hence, the sandstone NCT established using the Norwegian Sea data are used as the reference depth trend for the Stø formation in the Barents Sea. Note that the eastern part of the Norwegian Shelf and mainland Norway also experienced uplift and erosion during the late Cenozoic with decreasing magnitude outwards from the coastline (Hansen, 1997). Thus, the reference wells in the Norwegian Sea are selected from areas with no or little uplift according to the exhumation map for the area between the Danish-Norwegian sector border and 66°N created by Hansen (1997). Generally, the selection of wells and data processing follow specific principles to minimize the influence of undesired factors. The following principles are applied: 1) Wells with sandstone formations in a hydrostatic compaction state are selected to avoid the effects of overpressure. 2) Brine saturated sandstones are preferred. In cases where the pore space of sandstone is filled with hydrocarbons, the measured velocity and density logs are corrected. To minimize the fluid substitution impact, for wells in the Norwegian Sea, only the water zone data are used, and the sections saturated with hydrocarbons are excluded from the reference dataset by utilizing the oil-water contact (OWC) and gas-water contact (GWC) information present on the NPD website. Note that two oil-saturated (Wisting) wells penetrating the Stø formation are included in the analysis. The rest of the wells are brine saturated. 3) All the deviated wells are calibrated for True Vertical Depths (TVDs) to ensure consistency in the depth reference across the wells. Figure 3.3a shows the well location maps of the study areas. An interactive map is created for visualizing the well locations and associated structure information. In addition to the Barents Sea wells, the exhumed well 6510/2-1 Ylvingen fault complex in the Norwegian Sea is also included in the analysis. The location of this well is marked with an orange star in Figure 3.3a.
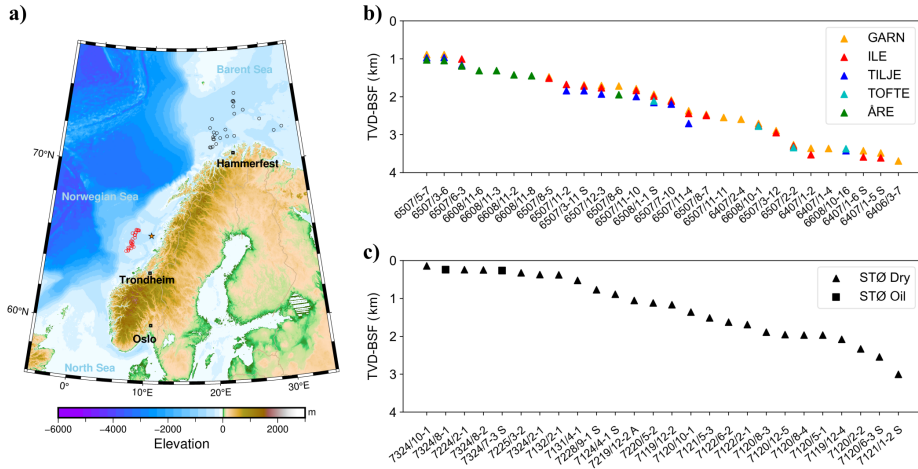
Figure 3.3: (a) Well locations for 29 selected wells (28 reference wells and 1 exhumed well) in the Norwegian Sea and 26 wells in the Barents Sea. Check the interactive well location map for more information. (b) Top depths of the clean sandstone formations in 28 reference wells. All sandstones are brine saturated (c) Top depths of the clean Stø formation. Two Wisting wells are oil saturated. The top depths are in True Vertical Depth Below See Floor (TVD-BSF).

As indicated by Figure 3.3b, the tops of clean sandstone formations in the reference wells exhibit a wide and nearly continuous depth range, ensuring the generation of reliable depth trends. These sandstones primarily belong to the Fangst group, which includes the Garn and Ile formations. Additionally, clean sandstones from the Båt group, specifically the Tilje, Tofte and Åre formations are used to supplement the creation of the reference depth trend. Note that the Åre sandstones with burial depths exceeding 2 km are excluded from the dataset. Because the prevailing interbedding of sand-shale sequence with coal embedding layers makes those Åre sandstones less comparable to the Stø formation. The well-log data undergoes rigorous quality controls following the steps outlined in Ktenas et al. (2017). Moreover, the rock physics screening approach proposed by Avseth et al. (2021) is used to check whether the well-log data is physically justified. This screening approach also facilitates the identification and removal of erroneous total porosity data, washouts, and calcite cement layers. The cut-off $V_{sh} \leq 10\%$ is used to define clean sandstones across all sandstone formations in the total 55

wells in the Norwegian and the Barents Sea. Figure 3.4 illustrates that the clean
sandstone data, categorized by formation, align nicely within the elastic domain
defined by different robust rock physics models (Avseth et al., 2021).
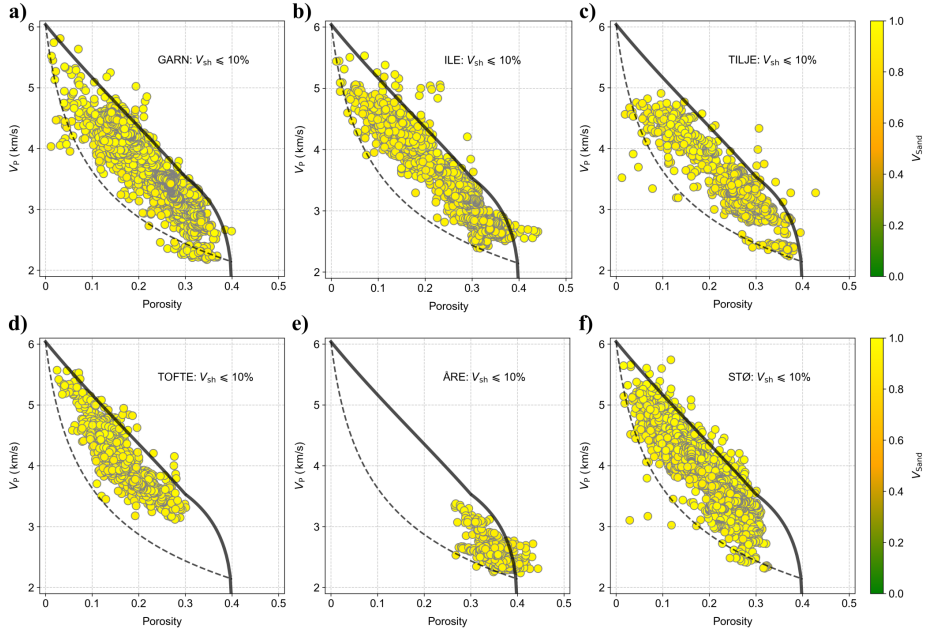
Figure 3.4: Rock physics diagnostics of well log data from the Norwegian Sea
and the Barents Sea clean sandstone formations using elastic bounds. Garn, Ile
formations from the Fangst group are shown in (a) and (b), respectively. Tilje,
Tofte, and Åre formations from the Båt group are shown in (c), (d), and (e),
respectively. The Stø formation data are shown in (e). The lower bound (dashed
line) is friable sand model (Mavko et al., 2020) computed at $\sigma' = 20$MPa. The
upper bound (solid line) is modeled with contact cemented model (Dvorkin and
Nur, 1996) blended with increasing cement model (Avseth et al., 2010a) at $\phi = 0.3$.

The porosity values are not directly measured but rather derived from the density
log. To verify the accuracy of the density-derived total porosity data, three pub-
lished porosity depth trends are compared to the well-log data from the Norwegian
Sea. Ramm and Bjørlykke (1994) proposed a linear porosity compaction model
based on the He porosity data sourced from Jurassic sandstones, including the Båt
group and Garn formation in the Haltenbanken area. In the same paper, a cou-
pled model that considers both mechanical compaction and quartz cementation
was concurrently presented to honor the increased porosity depth trend gradients

below intermediate burial at around 2600m. The compaction trend from Ehrenberg (1990) was derived from the average core porosity data for the Garn formation in the Haltenbanken area.
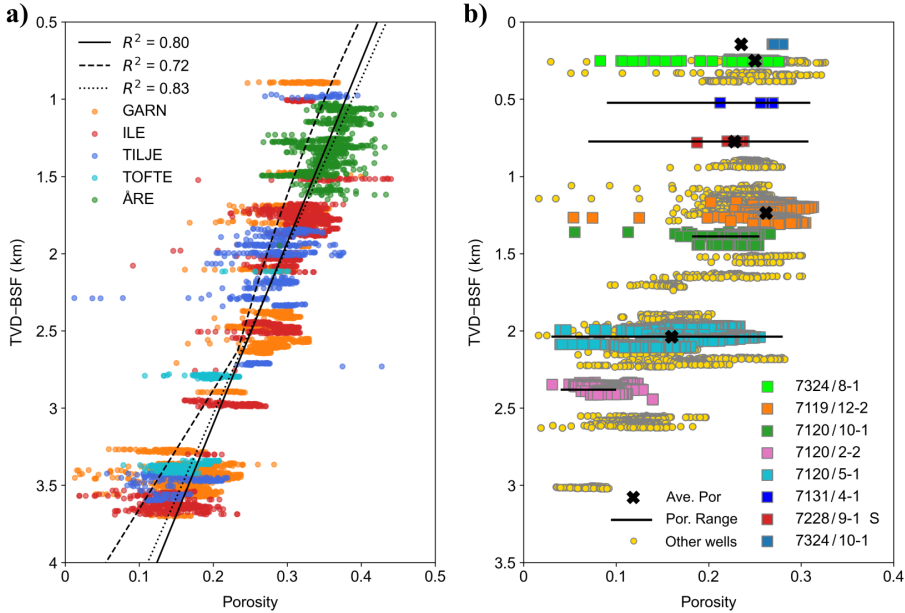
Figure 3.5: (a) The Norwegian Sea porosity data of clean sandstone formations plotted against three published porosity depth trends. The linear Halten trend-line proposed by Ramm and Bjørlykke (1994) is depicted as a solid line. Ramm and Bjørlykke (1994) also proposed a coupled mechanical-chemical model (dashed line), namely the porosity loss due to mechanical compaction follows an exponential decay model, and the porosity loss caused by quartz cementation in deeper burial is a linear model. The dotted trend line is digitized from Figure 3.6 in Ehrenberg (1990). The functional forms of these depth trends are listed in Table 3.2. (b) The porosity versus depth plot of the Barents Sea Stø formation. Wells with porosity validation are highlighted with color-coded squares. The porosity range and average porosity values are tabulated in Table 3.3.

Figure 3.5 depicts the comparison between the derived porosity data from well logs and the published porosity depth trends. It is observed that the coupled model tends to underestimate the porosity with a relatively low explained variance. This discrepancy may be attributed to the fact that the depth axis of the coupled model is not measured depth, but is calculated thermal maturity corrected depth based on the thermal history of the Northern Viking Graben, as described in Ramm

and Bjørlykke (1994). Nonetheless, both linear trendlines derived from core data fit the selected Norwegian Sea data with reasonable goodness, thus validating the porosities derived from well logs.

Table 3.2: The empirical porosity and velocity depth trends used in this work. Note that the functional form of the porosity model is not published in Ehrenberg (1990). It is obtained by linear regression of the digitized data point from the original plot in the paper. Japsen (1998) also proposed a regional segmented depth trend for the North Sea Chalk but with different function parameters.

	Model	unit		References
		ϕ or V_P	z	
ϕ-z	$\phi = 46.4 - 0.0085z$	%	m	Ramm and Bjørlykke (1994)
ϕ-z	$\phi = 45 - \exp(-0.00025z)$ $\phi = 25 - 0.013(z - 2500)$	%	m	Ramm and Bjørlykke (1994)
ϕ-z	$*\phi = -0.092z + 0.48$	frac	km	Ehrenberg (1990)
V_P-z	$V_P = 2325 + 0.51z$	m/s	m	Scherbaum (1982)
V_P-z	$V_P = 304.8/(135.9 - 20.22z)$	km/s	m	Hillis (1995)
V_P-z	$V_P = 2600 + (1/1.76)z$	m/s	m	Storvoll et al. (2005)
V_P-z	$V_P = \begin{cases} 1550 + 0.6z & z < 1393 \\ -400 + 2z & 1393 \leq z < 2000 \\ 2600 + 0.5z & 2000 \leq z < 3500 \\ 3475 + 0.25z & 3500 \leq z < 5300 \end{cases}$	m/s	m	Japsen (2000)
V_P-z	$V_P = \begin{cases} 1708 + 0.66z & z \leq 2630 \\ 1200.8 + 0.85z & 2630 < z < 4000 \end{cases}$	m/s	m	This study

The porosity values derived from cores sampled in some of the Barents Sea wells are compared with the well log-derived porosities for the Stø formation. The data used for comparison, along with the associated references, are presented in Table 3.3. Figure 3.5b demonstrates a good agreement between the well log data agrees and the average and range of porosities derived from core samples. Notice that a mismatch between the average core porosity value and the density porosity for

the Stø formation in well 7324/10-1. This discrepancy arises because the Stø formation in this well is condensed, with a net sand thickness of only 6.13m and a net-to-gross (N/G) ratio of 76.6%. The average porosity is affected by the presence of shaly sand, resulting in a slightly higher density-derived porosity for the clean sandstone ($V_{sh} \leq 10\%$) compared to the average porosity.

Table 3.3: The core porosity measurements of the Stø formation in some of the selected wells in the Barents Sea. The data from NPD are petrophysical evaluations documented in the well reports.

Wells	TVD-BSF Ave. (m)	Por. Ave.	Por. Range	References Por. Ave.	References Por. Range
7324/10-1	143.9	0.235	-	NPD	-
7324/8-1	250	0.25	-	Meunier (2019)	-
7131/4-1	524.2	-	$0.09 - 0.31$	-	Henriksen et al. (2011)
7228/9-1 S	774.3	0.228	$0.07 - 0.308$	NPD	Henriksen et al. (2011)
7119/12-2	1236.5	0.262	-	NPD	-
7120/10-1	1388.5	0.22	$0.18 - 0.255$	NPD	NPD
7120/5-1	2037.3	0.16	$0.03 - 0.28$	NPD	Løvstad et al. (2022)
7120/2-2	2381.6	-	$0.04 - 0.1$	-	Henriksen et al. (2011)

3.4 NCT assumption validation

The reference velocity depth trend is established using the sonic velocity data of clean sandstones from the Norwegian Sea. This compaction trend serves as the basis for the analysis of stress release impacts on the velocity data in other selected wells. As shown in Figure 3.6, the reference velocity data show a monotonous increase with increasing depth, which is usually approximated by linear trendlines (Japsen et al., 2007). Figure 3.6 displays five previously published velocity depth trends (Scherbaum, 1982; Hillis, 1995; Japsen, 2000; Storvoll et al., 2005; Ktenas et al., 2017) along with the reference data present in this work. The function

forms of all trendlines are tabulated in Table 3.2. These trendlines underfit the data to varying degrees. In order to better describe the average velocity increase resulting from mechanical compaction and quartz cementation during burial of the Norwegian Sea data, a linear segment NCT (yellow line) is proposed. This NCT adopts the onset of cementation depth ($\approx$2630m) approximated by the coupled model proposed by Ramm and Bjørlykke (1994). Figure 3.6 demonstrates that the proposed NCT aligns well with velocity data. The trend also agrees well with the velocity in the gas saturated Garn formation in well 6507/3-7 after Gassmann (1951) fluid substitution (grey data points).
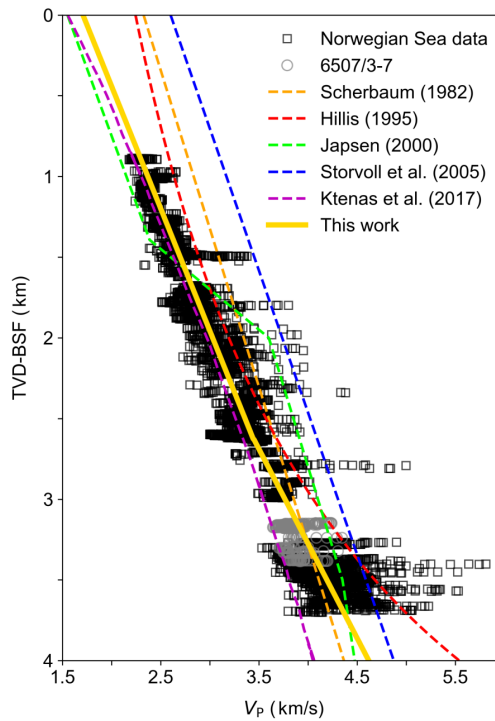
Figure 3.6: Comparison of the Norwegian Sea clean sandstones velocity data to the NCT of this study and previously published NCTs applying to sandstone. The functional forms of the baselines are given in Table 3.2. The trendline from Ktenas et al. (2017) is digitized from the original plot. The HC-saturated well 6507/3-7 fills the gap depth location, the velocities after Gassmann fluid substitution fall on the depth trend proposed in this study.

Well 6510/2-1, located close to the Norwegian coastline, has been affected by the

uplift of mainland Norway (Hansen, 1997). The well penetrates several sandstone formations that are also present in the reference wells, including the Garn, Ile, Tilje, and Åre formations. Note that, the sandy sequences in this well contain thin coal beddings whose depth locations are identified and documented in the well report. Therefore, these thin coal layers are removed from the dataset. Figure 3.7a illustrates the comparison between the reference velocity depth trend (solid black line) proposed in this study and the well log data of clean sandstone formations in well 6510/2-1. To mitigate the lithological effects that may cause exceptionally high velocities, such as layers of calcite concretions within the sandstone, running moving means have been applied along the depth axis using a window size of 1m (Ravasi and Vasconcelos, 2020). The data points are color-coded by porosity. The core evaluated porosities (see Table 3.4) and the corresponding average velocities for each sandstone formation in the exhumed well 6510/2-1 are highlighted as squares with black edges in both Figure 3.7a and 3.7b.
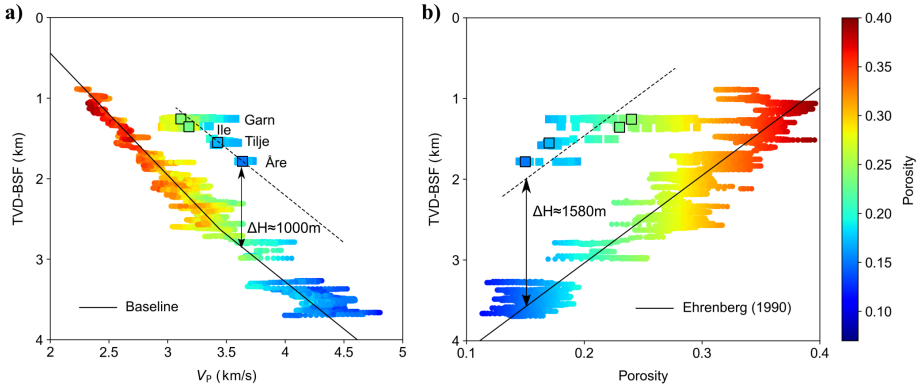
Figure 3.7: Stress release effect identification for exhumed well 6510/2-1 in the Norwegian Sea. The core porosity data highlighted in the plot for the well are tabulated in Table 3.4. (a) Data visualization in the velocity-depth domain, the segmented velocity NCT (Normal Compaction Trend) proposed in this study is plotted as baseline. The auxiliary dashed line is the result of linear fitting to the highlighted velocities in the exhumed well, with a constrained gradient that matches that of the quartz cementation line segment in the velocity baseline quartz cementation. (b) Data visualization in the porosity-depth domain, the empirical porosity NCT with the highest explained variance (Ehrenberg, 1990) is plotted as a reference. The auxiliary dashed line has the same gradient as the Ehrenberg porosity reference trend.

Before proceeding with the data analysis, it's useful to recall the model-derived hypothesis: porosity can serve as a stress release indicator when estimating the exhumation magnitude using the conventional velocity depth trend approach. If the rock was affected by the stress release during exhumation, the porosity at the current depth location will be smaller than that of the rock with the same velocity on the reference velocity depth trend. And the magnitude yield by the conventional approach will underestimate the true magnitude of exhumation.

As depicted in Figure 3.7a, the porosities of uplifted sandstone formations are visibly smaller than that of the vertical projection counterpart in the reference velocity trend, i.e., $\phi_A = \phi_{ref}$ as described by the case 3 interpretation of the conceptual modeling. The hypothesis regarding the underestimation of exhumation magnitude is also verified. As shown in Figure 3.7b, the vertical offset estimated using the porosity depth trend is larger than the offset determined from the velocity depth trend. The discrepancy between these estimates is approximately 600m. Sidewall cores have been from the sandstone formations in this well. According to the well report, the cores are mostly soft and friable despite the sandstones being predominantly cemented, ranging from weak to moderate and high cementation degrees in Garn and Båt groups (Table 3.4). Notably, some of the cores exhibit shattered grains and cement fabrics, which indicate significant stress-weakening effects.

In the Barents Sea data, similar inconsistencies in porosity are also observed between the exhumed rock and its iso-velocity counterpart in the reference velocity depth trend. Figure 3.8 illustrates the average velocity and porosity response of the clean Stø formations in each of the Barents Sea wells. Interestingly, the porosity inconsistency is particularly pronounced for rocks currently buried less than 1 km below the seafloor. When comparing the magnitude estimated using the velocity depth trend (Figure 3.8a) to the magnitude given by the porosity depth trend (Figure 3.8b), the difference is also maximized for the shallowly buried rocks. The

Table 3.4: The average petrophysical result of sandstone section in well 6510/2-1. Data is taken from the final well report from NPD. All depths are in Measured Depth (MD).

Formation	From (m)	To (m)	Sidewall core sampling depth (m)	Cementation	Coherence and hardness	Porosity
Garn	1543	1654	1597.5	Very weakly cemented	Friable	0.24
Ile	1688.5	1719.5	1704	Weakly cemented	Friable very soft	0.23
			1718.5	Very weak silica cement	Very friable	
Tilje	1823	1945	1853	Weak silica cement	Friable, soft to firm	0.17
			1883	Moderate silica cement	Friable	
			1887	Weak siliceous cement	Shattered	
Åre	1945	2236	1952	Silica cement	Friable	0.15
			1991.3	Weak silica cement	Very friable	
			2067	Weak silica cement	Very friable/crumbly	
			2163.5	Silica cement	Shattered	

porosity inconsistency becomes less prominent for rocks at intermediate burial depths between 1 to 1.7 km and diminishes further for rocks with deeper burial. It is worth noting that in Figure 3.8a, the Wisting wells 7324/8-1 and 7324/7-3 S exhibit great differences in their distances to the reference velocity depth trend. While in the porosity depth domain (Figure 3.8b), these two wells show larger distances to the porosity depth trend, but the difference between them is smaller compared to what is observed in the velocity depth domain.

The porosity inconsistency can be computed approximately by using the reference velocity and the reference porosity depth trends. By taking the velocity of the exhumed rock at the current depth, the corresponding burial depth location on the reference velocity depth trend can be determined by inverting the linear segment function proposed in this study. Next, the reference porosity trend from Ehrenberg (1990) is used to compute a corresponding average porosity response at this depth location. The porosity inconsistency is then computed by subtracting the porosity of the exhumed rock from the computed porosity. Figure 3.9 presents the porosity inconsistency for the Barents Sea data plotted against the burial
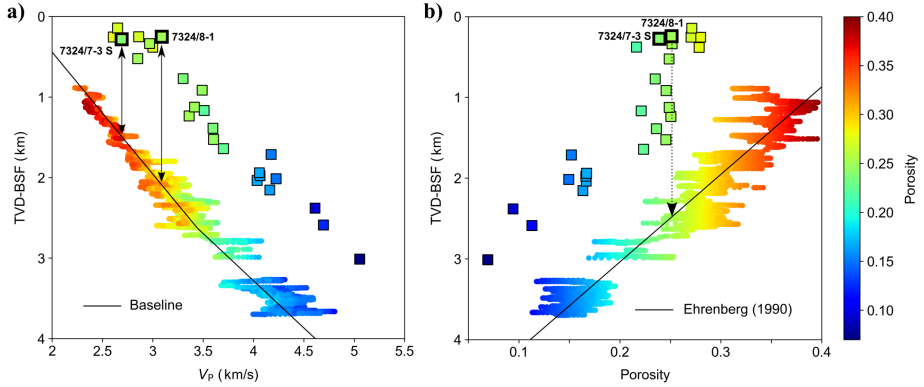
Figure 3.8: The mean velocity and (b) porosity variations with depths of the clean Stø formations in the Barents Sea wells compared to the reference depth trends established using the Norwegian Sea data.

depth. The data points are color-coded by the corresponding structure element of each well. The results reveal relatively small porosity inconsistency (less than 2% porosity unit) in the Hammerfest basin, Ringvassøy-Loppa Fault Complex, Måsøy Fault Complex, and Polhem Sub-platform. These structures are mainly located on the southwestern side of the Barents Shelf (check the map interactively). Conversely, higher porosity inconsistency is observed in the wells located in the bank area of the Finmark Platform and Signalhorn Dome. Notably, wells exhibiting significant porosity inconsistency are found on the north Barents Shelf, including the Bjarmeland Platform, Hoop Fault Complex, and Norvarg Dome.

Figure 3.10 presents a compilation of different published estimations of the total Cenozoic exhumation of the Barents Sea shelf, obtained using various estimation approaches. The data utilized in this compilation are taken from Henriksen et al. (2011), Baig et al. (2016), and Lasabuda et al. (2021). Despite the confidence variability and methodological uncertainties, a general pattern emerges wherein exhumation tends to increase from the southwest to the north. Interestingly, it is observed that the porosity inconsistency also exhibits the same spatial variation and is positively correlated to the magnitude of exhumation.
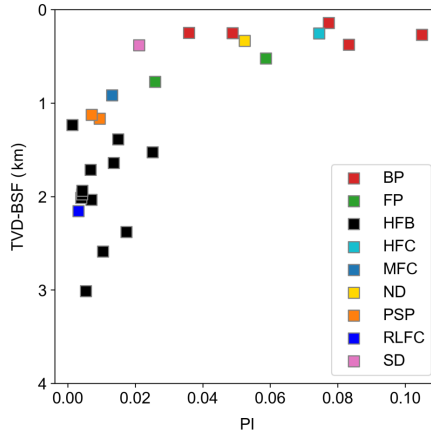
Figure 3.9: The porosity inconsistency computed for the Barents Sea wells; Data points are color-coded by the corresponding structure unit. Abbreviations used: BP: Bjarmeland Platform; FP: Finmark Platform; HFB: Hammerfest Basin; HFC: Hoop Fault Complex; MFC: Måsøy Fault Complex; ND: Norvarg Dome; PSP: Polhem Sub-platform; RLFC: Ringvassøy-Loppa Fault Complex; SD: Signalhorn Dome.

3.5   Discussion

The main objective of this study is to gain a deeper understanding of the interplay between cementation and stress release during uplift and their impact on exhumation estimation using the velocity compaction trend method, thereby verifying the validity of the irreversible compaction of the NCT method. Through conceptual modeling, we propose that porosity inconsistency plays an important role in diagnosing the presence and degree of stress release, as porosity is less sensitive to stress reduction compared to the elastic properties of the rock. The analysis of well-log data from the Norwegian Sea and Barents Sea supports the hypotheses derived from the conceptual modeling.

The sandstone data obtained from well 6510/2-1 in the Norwegian Sea shows evident porosity inconsistency in the velocity-depth domain. The presence of local shattered features in soft cemented sidewall cores suggests the potential stress weakening of the sandstone during uplift. However, it is important to acknowl-

Figure 3.10: The net exhumation estimations from published studies using different estimation methods with the uncertainties indicated as err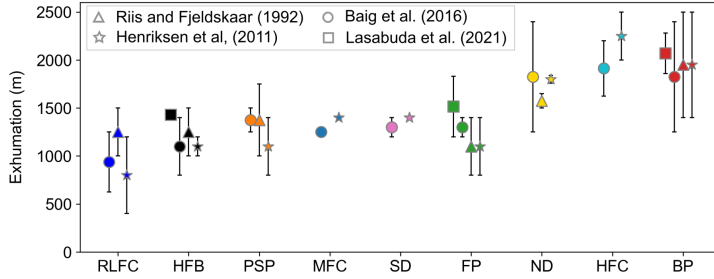or bars. Abbreviations and color coding are the same as used in Figure 3.9. The circle indicates estimations based on the shale compaction trend, thermal maturity and shot gathers methods from Baig et al. (2016). The triangle represents the estimations given by the vitrinite reflectance method in Riis and Fjeldskaar (1992). The star represents the estimations from Henriksen et al. (2011) which is a compilation of results from vitrinite reflectance (VR), sandstone diagenesis, thermal apatite fission track and shale compaction method. The square represents the summation of the pre-glacial (Lasabuda et al., 2018) and the post-glacial (Laberg et al., 2012) exhumation estimation using mass balance (Lasabuda et al., 2021). Data are taken from Lasabuda et al. (2021), Baig et al. (2016) and Henriksen et al. (2011).

edge the uncertainty associated with the interpretation: it is not trivial to distinguish between the coring effect and potential uplift-induced weakening effect in the core, as retrieval from deep boreholes can cause core damage and significantly alter the rock mechanical properties (Holt et al., 2014). Nevertheless, rock core samples extracted from normally buried wells with similar degree of cementation are mostly hard and firm without any shattered features (Table 3.5). This observation strengthens the confidence in the interpretation that the stress release effect contributes to the weak coherence and hardness of the core samples retrieved from the uplifted well. It also suggests that coring may not significantly weaken a cemented sandstone that is hard and firm. However, if the sandstone has undergone extensive unloading prior to coring, the coring process can induce weakening. In practical scenarios, it is possible to observe that a rock sample, taken from an exhumed area with a shallow burial depth, may display a significant stress sensitivity of velocity which arises due to both coring and stress release.

Table 3.5: Core description for sandstone in some of the selected Norwegian Sea wells. Data are taken from the NPD website

Well	Core sample depth	Group	Cement	Coherence and hardness
6608/10-1	3065-3092 3159-3187	Garn Ile Tofte Åre	Silica cement Silica cement Moderate Silica	Moderate hardness Moderate to hard hardness Moderate Firm to moderate caused by silica cement
6507/2-2	3672-3697 3697.5-3720 3746-3770 3790-3810	Garn Ile Tofte Tilje - Åre	Strong Strong Moderate Strong	Very hard Very hard Hard to friable Moderately hard to hard
6407/1-4	3675-3776	Garn	Locally hard Silica cement	Moderately hard to hard
6407/1-2	3716	Garn	Very weakly Silica cement	Render the rock hard but friable

The Wisting Central well in the Bjarmeland Platform exhibits the most significant porosity inconsistency and the discrepancy between estimations derived using the velocity and porosity depth trends, as depicted in Figure 3.8. Lasabuda et al. (2021) estimated an exhumation magnitude of 1277m using the compaction trend of sonic velocity and a magnitude of 1300m using interval velocity for the shale interval in well 7324/8-1. This corresponds to a maximum burial depth of 1520 $\approx$ 1543m for the Stø formation in 7324/8-1, considering that the current burial depth below the sea floor is 243m for that well. The Stø formation in Wisting central area contains approximately $1-3$ percent quartz cement, according to the microscopic analysis (Meunier, 2019) and rock physics diagnostics (Lehocki et al., 2020). This indicates that the rock has been buried below the cementation window. The average temperature gradients for the research area in the Barents Sea range from 35°C/km to 42°C/km (Khutorskoi et al., 2008; Lasabuda et al., 2021). Lehocki et al. (2020) used a temperature gradient of 38°C/km in the rock physics modeling guided by a burial history for the Wisting area. Let's assume the onset of quartz precipitation happens at approximately 70°C$-$80°C (Bjørlykke and Jahren, 2010) and the temperature at the sea floor is 4°C. Quartz cementation is then expected to occur when the burial depth reaches at least 1.74km$-$2km

for sandstones in the Wisting well (with $T_{grad} = 38°C/km$). However, this depth range is greater than the maximum burial estimated by the sonic and interval velocity depth trend methods. Lasabuda et al. (2021) also reported an estimated exhumation magnitude of 1760m using a sandstone diagenesis approach for the Wisting Central well. The discrepancy between the sandstone diagenesis method and interval/sonic velocity methods is considered to be related to structural complexities, strain partitioning and differential erosion according to Lasabuda et al. (2021). As demonstrated in this study, the velocity NCT methods tend to underestimate the true magnitude of the exhumation due to the neglect of stress release and its interplay with the cementation effect during uplift. Although the sandstone diagenesis approach used by Lasabuda et al. (2021) honors the impact of sandstone cementation, it does not account for the stress release effect. Hence, it is postulated that the Wisting central well may have been buried even deeper than 1760m, considering the significant porosity inconsistency observed in this well.

In addition to the porosity inconsistency, the stress release effect becomes evident through the discrepancy in exhumation magnitudes estimated using velocity and porosity depth trends. As shown in Figure 3.7 and Figure 3.8, in the porosity-depth domain, the estimation is higher. However, this higher estimation is not the true magnitude either. As mentioned in the section on conceptual modeling, during uplift within the cementation window, the porosity acquired at the maximum burial will continue to decline due to ongoing cementation. Theoretically, if the rock is affected by stress release, the true exhumation magnitude may lie between the magnitudes derived from velocity NCT and the porosity NCT. On the other hand, when the stress release effect is negligible, the two magnitudes should be equal. Note that, the sandstone diagenesis method, considering the cementation effect, can serve as a more accurate lower bound for exhumation estimation compared to the velocity NCT method. For example, the exhumation magnitude estimated using the diagenesis approach for the Wisting Central well is

about 1760 to 2000m (Lasabuda et al., 2021; Lehocki and Avseth, 2021), which is higher than about 1300m given m approach for shale intervals, and is smaller than 2500m as given by the porosity depth trend in Figure 3.8b. Hence, the Wisting well might have been buried between 2000m (given by sandstone diagenesis) and 2500m (the porosity depth trend) before being uplifted. Given the proportional relationship between cementation speed and burial/uplift rate (Figure 3.2b), along with the inhibiting effects of coating and oil saturation on quartz precipitation, it is expected that the reduction in porosity during cementation while experiencing uplift would be insignificant. Consequently, the exhumation magnitude is likely to closely align with the magnitude derived from porosity. In practice, by establishing or finding published regional porosity and velocity depth trends of sandstones that are comparable to the sandstone in the exhumed area can be very useful to help narrow down the uncertainty of the exhumation estimation performed by using other lithology e.g., shale or chalk compaction trends.

An intriguing observation from the analysis of the Barents Sea Stø formations, as depicted in Figure 3.9 and Figure 3.10 is that there exists a positive correlation between exhumation magnitude and porosity inconsistency. In other words, the extent to which the rock has been affected by stress release during uplift is higher when the exhumation magnitude is greater. This finding aligns with the conceptual modeling prediction. Figure 3.1 illustrates the stress-dependent uplift modeling, indicating a non-linear stress release effect where velocity decreases with an increasing gradient from the exit of the cementation window to the sea surface.

This observation aligns with the findings of Han et al. (2021) regarding the influence of overpressure on rock properties. In their study, Han et al. (2021) conducted simultaneous measurements of ultrasonic velocity and porosity on three quartz-dominated Berea sandstones. The pore pressure was systematically increased from 0 to 40 MPa while maintaining a constant confining pressure of 50 MPa. This gradual increase in pore pressure reduced the effective stress imposed on the samples.

As depicted in Figure 3.11, the porosity exhibited a slight linear increase with pore pressure, whereas the compressional velocity showed a much stronger nonlinear dependence on pore pressure. Han et al. (2021) emphasized that the increase in porosity alone was insufficient to explain the exponential variation in elastic properties of the rock with pore pressure. Instead, they highlighted that changes in the microstructure of the rock played a more significant role in the exponential decrease in elastic velocity. Likewise, the stress-dependent uplift modeling in this study assumes that porosity remains unchanged while velocity decreases due to stress release. The velocity reduction is modeled using the Varying Patchiness Cement Model (Yu et al., 2023a), which accounts for the deterioration of cement coherence. The corresponding results from this study and the overpressure study by Han et al. (2021) indicate that the pore pressure prediction in exhumed rocks cannot purely rely on empirical effective stress–porosity relationships.
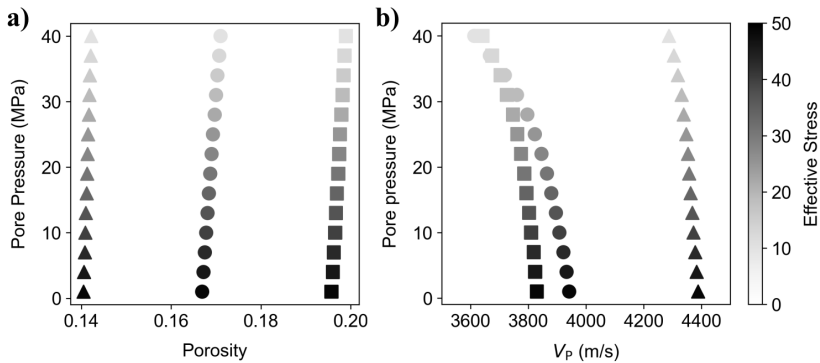
Figure 3.11: (a) Porosity and (b) velocity of three Berea sandstone samples measured as a function of pore pressure ranging from 0 to 40Mpa. The confining pressure is maintained at a constant 50 MPa. The data are sourced from Han et al. (2021).

Another important implication derived from the results of this study pertains to feasibility studies and the interpretation of time-lapse seismic data in uplifted reservoirs: since the reduction of effective stress in reservoir rocks can occur not only due to the removal of overburden but also because of pore pressure buildup, it is plausible to anticipate that the weakening effect of stress release associated

with uplift can render a reservoir in an exhumed area more sensitive to further stress changes caused by fluid injection. Moreover, the heightened response to effective stress variation during injection may be underestimated if the mechanical compaction and cementation models are used in isolation without accounting for the prior uplift.

All the rock physics models utilized in the conceptual modeling are isotropic, and the collected field data primarily consist of axial P-wave velocities. A noteworthy finding made by Torset et al. (2021) is the reversal of P-wave anisotropy during simulated uplift. This reversal was attributed to the tensile deformation having a directional dependence favoring the reduction of the vertical P-wave velocity. The stress dependence of P-wave anisotropy has also been explored in Firdaus et al. (2022), who examined different lithologies and stress paths. Both studies support a pressure dependence of the anisotropy due to preferentially aligned deformation. In future research, it would be valuable to investigate the potential for an uplift-controlled, depth-dependent anisotropy trend to manifest in real-world examples using the similar workflow present in this work. However, gathering data to establish such a trend can be challenging. Nevertheless, it might be feasible to obtain an "estimated" trend of anisotropic parameters derived from analyzing wide-azimuth seismic data (Bachrach et al., 2009).

The dataset exclusively consists of sandstones. However, it is natural to question if the stress release effect observed in sandstone is also present in shale. Obradors-Prats et al. (2019) offer valuable insights into this question through coupled geomechanical-poroelastic modeling by incorporating a phenomenological diagenetic model that describes the smectite to illite transition in shale into a constitutive model. The integrated modeling framework, guided by an approximate burial history similar in this work, reveals that the shale packages become more prone to failure due to the ductile to brittle transition, and predicts a softening of shale during simulated uplift. These findings, combined with the results obtained

in our study, emphasize the importance of considering the effects of cementation and stress release when conducting research on both sandstone and shale.

In this study, we have presented the collection, processing, and analysis of data from a substantial number of wells to validate the hypothesis derived from the conceptual modeling. The advantage of the dataset present in this work is that it provides a significantly broader foundation for drawing conclusions regarding the effects of stress release compared to the limited and synthetic core data that has been previously utilized. However, it is important to note that data collection is limited to the Norwegian Sea and Barents Sea. The principles for well selection and data evaluation, as well as the data analysis workflow presented in this work, can be utilized as a framework for conducting similar analyses in different regions. It would be highly encouraging if similar results could be obtained in other exhumed basins in the future. Note that although the dataset has been carefully processed prior to data analysis, the natural variability related to textural and compositional complexities, such as sorting, clay content, grain size, and packing can still introduce significant ambiguities in the porosity-velocity space (Løvstad et al., 2022). Conceptual modeling can never fully capture the complexities of reality. Moreover, the Cenozoic exhumation in the Barents Sea is believed to be multi-episodic (Japsen, 2000; Sobolev, 2012; Zattin et al., 2016), while the modeling in this work assumes continuous uplift of the rock from the maximum burial to the sea floor. Nevertheless, the impact of stress release persists in the rock and accumulates over time, ultimately leading to the permanent alteration of rock properties (Bjørlykke and Jahren, 2010; Torset et al., 2021). Future work could explore the possibility of integrating the impact of unloading-reloading cycles on the elastic and acoustic properties of rocks into the estimation of exhumation.

3.6 Conclusion

It is commonly assumed in the NCT method that the velocity and porosity acquired at the maximum burial remain unchanged as the rock is uplifted towards the surface when estimating the magnitude of exhumation. However, the findings of this study challenge that assumption. By using the porosity inconsistency as a qualitative and quantitative metric of stress release, it has been demonstrated that the compressive velocity of sandstone in the exhumed regions of the Norwegian Sea and Barents Sea is more affected by exhumation compared to the porosity. The degree of stress release impact is positively related to the magnitude of exhumation. The results of this study highlight the limitations of using velocity as the sole metric for the exhumation estimation without considering the effects of stress release, cementation, and their interplay. Relying solely on velocity depth trends, as has been done in past and potentially future exhumation estimation studies, is likely to lead to underestimating the magnitude of exhumation. Furthermore, the findings in this work also suggest that the inconsistent variation of elastic stress sensitivity and acoustic stress sensitivity of reservoir rocks due to stress release is crucial for understanding core damage evaluation, pore pressure prediction, time-lapse seismic interpretation, and the feasibility of fluid injection in reservoir rocks in areas affected by significant exhumation.

3.7 Acknowledgments

3.8 Data availability

All well-log data used in this study are currently released by the Norwegian Petroleum Directorate and available for members of Diskos (The Norwegian National Data Repository for Petroleum data: www.npd.no/en/diskos).

3.A Input burial history

The burial history from Torset et al. (2021) is adopted for the conceptual modeling in this work. The main inputs include temperature gradient g_T, effective stress gradient g_S, seafloor temperature T_0, temperature at the onset of temperature T_c, burial rate r_b, uplift rate r_u, and maximum burial depth. The corresponding values are tabulated in Table 3.6. Note that two maximum burial depths are used in the conceptual modeling, i.e., 2.5km for point B and 3.2km for point C in Figure 3.1, respectively.

The depth at which quartz cementation begins can be calculated as:

$$Z_c = (T_c - T_0)/g_T \tag{3.1}$$

Table 3.6: The input parameters used for conceptual modeling shown in Figure 3.1 and 3.2.

Parameters	Symbol	Magnitude	Unit
temperature gradient	g_T	35	°C/km
effective stress gradient	g_S	12	MPa/km
seafloor temperature	T_0	5	°C
cementation onset temperature	T_c	70	°C
burial rate	r_b	0.05	m/Ma
uplift rate	r_u	0.1	m/Ma
maximum burial depth	Z_{max}	2.5 and 3	km

3.B   Porosity modeling

3.B.1   Phase1: Mechanical compaction from seafloor to Z_c

According to Ramm (1992), the porosity variation with effective stress (typically expressed as burial depth) is found to follow:

$$\phi = \phi_c e^{-[\alpha_0 + (XV_{sh})]Z} \tag{3.2}$$

where ϕ is the porosity at current depth Z, ϕ_c is critical or depositional porosity taken as 40% (Ramm, 1997), α_0 is the framework grain stability factor of clean sandstones, assumed as 0.175 in this work following Ramm (1992), and X is a factor that describes the sensitivity to increasing clay content V_{sh}. In actual sandstones, the factor X would likely depend on the distribution of clay. Specifically $X = 1$ for dispersed clay. For clean sandstone, $V_{sh} = 0$, equation 3.2 collapses to the well-known exponential decay function from Athy (1930).

3.B.2   Phase 2: Quartz cementation during compaction

The effect of quartz cementation on porosity is calculated using the kinematic model proposed by Walderhaug (1996). The model assumes that mechanical compaction ceases upon the onset of cementation, and pore space is reduced solely due to continuous quartz precipitation within a time period:

$$\sum_{i=1}^{n} \Delta t_i = \frac{(Z_{max} - Z_c)}{r_b} \tag{3.3}$$

where n is number of time discretization Δt.

The volume of cement $V_{cem(i)}$ precipitates at a given time step t_i is described by:

$$V_{cem(i)} = \phi_1 - (\phi_1 - V_{cem(i-1)}) \exp\left[\frac{-MA_0a}{bc\rho_{qrz}\phi_1 ln(10)}(10^{b(ct_i+T_c)} - 10^{b(ct_{(i-1)}+T_c)})\right]$$

(3.4)

where ϕ_1 is the porosity resulted from phase 1 mechanical compaction, which can be calculated using equations 3.1 and 3.2 with $Z = Z_c$. $M = 60.09$ g/mol is the molar mass of quartz. The density of quartz ρ_{qrz} is 2.65 g/cm^3. Heating rate c in this phase is the product of burial rate and temperature gradient, i.e., $c = r_b g_T$. a and b are two constants that define the rate of quartz precipitation r_q. Here a linear time-temperature history is assumed, thus $r_q = a10^{ct+T_c}$. The default values from Walderhaug (1996),

where $a = 1.98 \times 10^{-22}$mol/cm^2 and b $= 0.0221/°$C are used. A_0 is the initial surface area available for quartz cementation assuming spherical grains with diameter D for one unit volume, which equals to:

$$A_0 = \frac{6f}{D}(1 - \gamma)$$

(3.5)

where f is the volume fraction of quartz grains in the sandstone at the onset of cementation, for sandstone with 100% quartz composition, $f = 1 - \phi_c$. If a sandstone contains 65% quartz blast, 10% feldspar, and 25% porosity after mechanical compaction, then $f = 0.65$. When quartz grains are coated by clay or other minerals, such as carbonate, the initially available quartz surface area will be reduced. This effect is taken care of by the factor γ, $\gamma = 0$ for the absence of coating in this study. When coating presents, $\gamma \in (0, 1]$ depends on the type and amount of coating.

Since $V_{cem(i)}$ at time step t_i depends on the cement volume $V_{cem(i-1)}$ at the previous time step t_{i-1}, Equation 3.3 needs to be solved iteratively. The quartz surface area at given time step is proportional to the porosity loss caused by quartz pre-

cipitation and can be calculated as:

$$A_i = A_0(1 - \frac{V_{cem(i)}}{\phi_1}), i = 1, 2, ..., n \tag{3.6}$$

The porosity variation due to the quartz cementation is:

$$\phi_i = \phi_1 - V_{cem(i)}, i = 1, 2, ..., n \tag{3.7}$$

3.B.3   Phase 3: Quartz cementation during uplift

The amount of quartz cement precipitated in the process of exhumation from the maximum burial to the depth point where the rock exits the cementation window can be calculated using the same procedure as outlined above. However, due to the disparity between the uplift rate and burial rate, the time series for this phase is different:

$$\sum_{j=1}^{m} \Delta t_j = \frac{(Z_{max} - Z_C)}{r_u} \tag{3.8}$$

As the rock is uplifted from the maximum burial towards the surface, the temperature progressively decreases over time. Therefore, the cooling rate becomes $c = r_u g_T$. The quartz precipitation is modeled using a modified version of Lander and Walderhaug (1999) model considering the cooling effect:

$$V_{cem(j)} = \phi_\tau - (\phi_\tau - V_{cem(j-1)}) \exp \left[\frac{MA_n a}{bc\rho_{qrz}\phi_\tau ln(10)} (10^{b(-ct_j + T_{max})} - 10^{b(-ct_{(j-1)} + T_{max})}) \right] \tag{3.9}$$

where $\phi_\tau = \phi_1 - V_{cem(n)}$ is the remaining porosity after the first phase cementation. T_{max} is the temperature at the maximum burial depth. The initial quartz surface area changes from A_0 to A_n which can be computed using equation 3.6 at the maximum burial.

The porosity variation with increasing quartz cementation is described by the

following relationship:

$$\phi_j = \phi_n - V_{cem(j)}, j = 1, 2, ..., m \qquad (3.10)$$

3.B.4 Phase 4: Uplift outside quartz cementation window

In the conceptual modeling, porosity is assumed to remain constant when the rock is uplifted beyond the cementation window.

3.C Velocity modeling

Rock physics models provide a direct mapping between porosity and velocity. The fluid effect can be incorporated using Gassmann (1951) fluid substitution.

3.C.1 Phase 1: Mechanical compaction from seafloor to D_c

The depth-dependent porosity during mechanical compaction is calculated using equation 3.2 for Z ranging from 0 to Z_c. The resulting porosity values are then used as input in the rock physics model to obtain the corresponding velocities. The rock physics mapping for dry sandstone, associated with mechanical compaction, is accomplished using the friable-sand model (Avseth et al. 2010a). The model computes the high porosity end member using Walton contact theory with shear correction (Bachrach and Avseth, 2010). To account for the sorting effect, the model extrapolates to lower porosity using the lower Hashin-Strikmann (1963) bound (Mavko, 2020), The detailed velocity modeling steps are described by equations A4 – A10 in Bredesen (2019).

3.C.2 Phase 2: Quartz cementation during compaction

A general practice of modeling the porosity reduction due to quartz cementation from critical porosity down to zero porosity involves two steps: firstly, when the

quartz cement is below a certain cement limit, e.g. 4% (Torset et al., 2021), the elastic moduli of the rock can be modeled using Dvorkin-Nur (1996) contact cement model. This model assumes that the quartz cementation starts from a random dense sand packing with critical porosity. For further quartz cementation beyond the cement limit, a modified Hashin-Strikmann upper bound is employed to interpolate between the contact cement model computed at the cement limit and the mineral point. This approach is commonly referred to as the increasing cement model (Avseth et al., 2010a).

However, when critical porosity is reduced due to preceding mechanical compaction before quartz cementation, the two-step modeling strategy requires modification. The modification is illustrated in Figure 3.12: the dots represent the dry velocities calculated using the friable sandstone model at the end of mechanical compaction, which reduced the porosity from critical porosity to approximately 29.8%. For each increment of quartz cement, the corresponding elastic moduli are calculated at critical porosity and extrapolated to the actual porosity using the lower Hashin-Strikmann lower bound. This ensures that the assumption in Dvorkin-Nur model is not violated. This adjustment is depicted by the movement from V_P CC to V_P CC adjusted (and V_S CC to V_S CC adjusted). Once the amount of cement exceeds the cement limit, the increasing cement model is appended as indicated by the V_P IC adjusted and V_S IC adjusted in Figure 3.12.

3.C.3 Phase 3: Quartz cementation during uplift

In this phase, the velocities of the sandstone are primarily influenced by quartz cementation and the degradation effects induced by uplift. Following Torset et al. (2021), the changes in elastic moduli of the sandstone, from maximum burial to the depth at which cementation ceases, can be modeled as a superposition of the effects from cementation models and stress release model. Note that the linear summation of effects arise from the two competitive mechanisms is a simplification
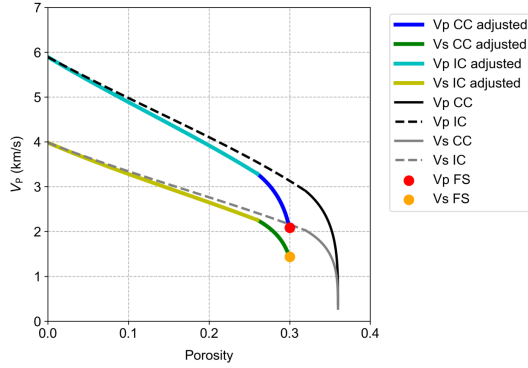
Figure 3.12: Modified two steps modeling strategy that solves the limitation of the contact cement model regarding the critical porosity assumption. Mechanical compaction of unconsolidated sand followed by quartz cementation can be modeled using this approach. Abbreviations: CC, Contact Cement model; IC, Increasing Cement model; FS, Friable-Sand model.

employed for the modeling purpose, the interplay between cementation and stress release can be highly nonlinear in actual geological settings.

The increasing stress sensitivity of wave velocity, resulting from the mechanical weakening of the cement upon stress release is modeled using the Varying Patchiness Cement Model (VPCM) proposed by Yu et al. (2023a). This model describes the softening of the cement by replacing connected patchy cement sandstone with disconnected patchy cement sandstone, this replacement is referred to as cement diluting in Yu et al. (2023a). The patchy cement sandstone model involves the mixing of two end members: stress-sensitive unconsolidated sands and stress-insensitive cemented sandstones, using Hashin-Shtrikman bounds. The connected patchy cement is resulted from the mixing using the upper HS bound, while the lower HS bound results in disconnected patchy cement. The effective cement fraction f_{CC} in Yu et al. (2023a) refers to the proportions of the connected patchy cement in the binary mixture. To apply VPCM in the stress-dependent uplift modeling, the cemented sandstone at the maximum burial depth is considered as a patchy cement sandstone with 100% connected patchy cement, thus the connected effective cement fraction $f_{CC} = 1$.

VPCM allows the modeling of both cement breakage by microcracks and crumbling of cement upon stress release. In this work it is assumed that the uplift only causes microcrack development within the cement. The stress-dependent factor α describing the cement diluting follows an empirical power law (Yu et al., 2023a):

$$\alpha = \left(1 - \frac{\sigma'}{\sigma'_0}\right)^m \tag{3.11}$$

where σ' is the current effective stress, σ'_0 is the effective stress at the maximum burial. m determines the rate of diluting depending on the type of cement and the magnitude of stress at which cement precipitates (Yu et al. 2023a). m approaches to unity with increasing cementation stress. In this work m is chosen as 1.2.

The detailed VPCM modeling can be found in equations 1–12 by Yu et al. (2023a). The procedure for modeling the combined effect of stress release and cementation during uplift can be summarized as follows: 1) Consider the rock at maximum burial depth as a binary mixture, where the cemented end member constitutes the entire mixture. 2) Model the stress release effect from the maximum burial point to the surface using the VPCM. 3) Determine ΔV (see Figure 3.13) by comparing the VPCM modeled velocity with the velocity at maximum burial depth. 4) The final velocity for the rock within the cementation window is obtained as a summation of the weakening effect modeled with VPCM and the cementation effect modeled with the increasing cement model.

3.C.4   Phase 4: Uplift outside quartz cementation window

During subsequent uplift, as the rock exits the cementation window, the quartz cementation ceases. As a result, the sandstone retains the velocity it possessed at the point of exit from the cementation window. This can be observed as the vertical red dashed line in Figure 3.13. When taking into account the effect of stress release, the velocity of the rock uplifted outside the cementation window will be the velocity indicated by the red dashed line, adjusted by subtracting the
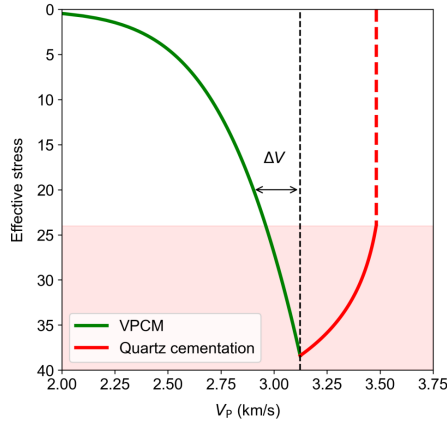
Figure 3.13: VPCM is a pure stress model that causes the reduction of velocity, while the quartz cementation is the detrimental factor to the porosity, thus causing the velocity to increase. When the rock exits the cementation window, the quartz cementation shuts down, hence the velocity is preserved at the end of quartz cementation as shown by the red dashed line. The final velocity profile is the summation of the cementation effect modeled with increasing cementation model and VPCM.

stress weakening effect ΔV modeled using VPCM model, as shown in Figure 3.13.

CHAPTER 4

OVERCONSOLIDATION AND STRESS RELEASE - A COMPARATIVE STUDY OF UNCONSOLIDATED SANDS AND WEAKLY CEMENTED SANDSTONE

This paper is submitted for publication and is therefore not included.

CHAPTER 5

ROCKPHYPY: AN EXTENSIVE PYTHON LIBRARY FOR ROCK PHYSICS MODELING

ABSTRACT: Rock physics aims to understand the relationship between the physical properties of rocks and geophysical observables under various conditions. The generic knowledge provides valuable insights into the behavior of subsurface rocks and has been applied in various fields. However, the availability of comprehensive open-source Python libraries for rock physics is quite limited. To address this limitation, we present **rockphypy**: a comprehensive and streamlined Python library that offers access to a vast array of rock physics models and workflows ranging from basic to sophisticated. The library is designed to be easily embedded in interdisciplinary fields such as deep neural networks and probabilistic frameworks, leveraging the rich resources of Python. Currently, **rockphypy** implements ten modules with over 100 methods, accessible through a straightforward and user-friendly API that facilitates various modeling tasks in rock physics. Its modular design allows easy extension to incorporate new features and functionalities. In addition to the versatility of the library, we have shown that **rockphypy** also greatly simplifies practical tasks that require many different rock physics models, enabling fast experimentation and iteration of research and practical programs.

5.1 Motivation and significance

Rock physics is a multidisciplinary field that draws upon geophysics, petrophysics, geomechanics, and geology. The term "rock" can refer to naturally occurring rocks, sediments and granular media, synthetic rocks created in laboratory settings (Rathore et al., 1995), and digital rocks created using high-resolution imaging and modeling techniques on computers (Andrå et al., 2013). The main objective of rock physics is to quantitatively describe the relationships between rock properties and physical measurables of rock under different conditions (Mavko et al., 2020). Physical measurements of rocks can be obtained from field-based remote sensing data acquisition methods (yilmaz, 2001), such as seismic, electrical and electro-

magnetic measurements, downhole well logging measurements, static and dynamic laboratory experiments (Fjær et al., 2008), as well as estimates from numerical simulations (Saenger et al., 2011). The sought-after relationships can be mathematically formulated as various rock physics models (RPMs). Numerous RPMs models targeting different research problems in rock physics have been proposed in the literature, which constitutes a complex yet invaluable repository of resources.

Rock physics has a wide range of applications in various fields and is essential for making informed decisions in many industries. For example, rock physics has played a crucial role in studying the effect of fluid extraction and injection on the subsurface reservoir system and its surroundings. It helps the quantitative interpretation and monitoring of changes in seismic responses resulting from variations in reservoir rock and fluid properties (Avseth et al., 2010a; Wang, 2001) Recently, there has been a shift in focus from energy recovery to reducing and neutralizing CO_2 emissions, the same generic rock physics knowledge has been increasingly applied to sustainable studies, such as CO_2 sequestration (Daley, 2019) and geothermal energy exploration (Bredesen et al., 2021). Another rapidly evolving field in rock physics is the intersection of rock physics, statistics (Grana, 2016), machine learning (Avseth et al., 2021), and deep learning approaches (Weinzierl and Wiese, 2021), enabling the uncertainty quantification of prediction using rock physics given limited data and promoting significantly the precision and accuracy of predictions given large volumes of data. To foster innovation and progress, it is crucial to democratize the rich resource of rock physics models, making them more adaptable to current computing power and infrastructure for AI-based inference in Python, and more accessible to the research community.

The Stanford SRB Matlab toolbox (Mavko et al., 2020) was one of the earliest open-source projects of an extensive implementation of various rock physics models. There have been other resources of rock physics models and applied examples written in Matlab (Avseth et al., 2010a). Researchers (Grana, 2016; Amato del

Monte, 2017) sometimes will publish Python codes containing a limited number of RPMs dedicated to the workflow present in the research papers. There are also a few open-source Github projects offering a selection of commonly used RPMs such as open_petro_elastic and rppy. Many of the projects mentioned above however don't regard RPMs as the centerpiece. More often, rock physics models are integrated into commercial software and remain prioritized. There is still a lack of comprehensive, standardized streamlined Python integration of the vast array of rock physics models available. To address this gap, we present **rockphypy**, an open-source Python library that provides an extensive, cohesive, and structured implementation of RPMs, supporting e.g. the modeling of elastic behavior of rock, fluid, and their coupling under various considerations, with over 100 methods. **rockphypy** is crafted to embody flexibility and versatility allowing easy extension and remaining adaptable to evolving rock physics field. There are two ways to use **rockphypy**, individual models and extensions are designed to be called without initializing an instance, on the other hand, given data, an instance of the practical workflows built upon different RPMs can be created, the instance is then used to do data analysis. In this way, **rockphypy** permits a great reusability of the code which allows for rapid experimentation and iteration of research and practical programs. This library is expected to be useful for both researchers and practitioners interested in various rock physics applications.

5.2 Software description

rockphypy is an open-source Python library for rock physics modeling. It is a trove of useful models and workflows that aims to offer a convenient and efficient way to perform complex tasks in rock physics studies. For that purpose, a consistent API and image galleries of examples and tutorials are documented on ReadTheDocs `https://rockphypy.readthedocs.io/en/latest/`. All examples can be downloaded as both Python files and Jupyter notebooks. The **rockphypy**

is currently released under the GNU General Public License (GPLv3)(GPL, 2020). To foster a community-driven innovation and collaboration, the codebase is publicly accessible on GitHub `https://github.com/yujiaxin666/rockphypy` and encourages contributions and continued development from the community.

5.2.1 Software architecture

rockphypy utilizes objected oriented programming (OOP) paradigm in Python to create modular, maintainable, and reusable code. the library is built upon two Python libraries numpy and scipy and consists of 10 core modules, each of which is associated with a class that holds the implementation of a specific group of models and workflows. Figure 5.1 depicts module organization and some keywords of the generic functions. The hierarchical classification of **rockphypy** is designed for easy extension to introduce new rock physics modeling approaches.

In rock physics modeling, it is often necessary to use multiple models to complete a task. Additionally, it is common for a newly proposed model to depend on existing models. As a result, the classes in **rockphypy** are designed to interact with one another and are mutually called. These interactions are illustrated and color-coded in Figure 5.1.

5.2.2 Software functionalities

rockphypy includes 10 classes and over 100 methods that can be used to perform a variety of rock physics modeling tasks. The list below provides a detailed description of each class and its purpose. Users are recommended to check the API interface of the library, which provides an exhaustive explanation of each individual method. Referred link of API: `https://rockphypy.readthedocs.io/en/latest/autoapi/index.html`

AVO: The AVO class consists of methods that model the Reflectivity, Amplitude Variations with Offset (AVO), and Amplitude Variations with Azimuth (AVOAz)
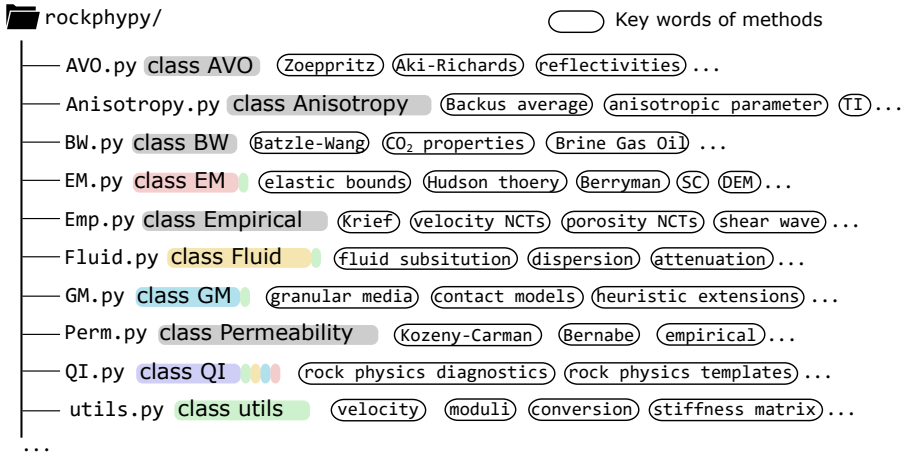
151

Figure 5.1: Codebase structure of rockphypy 0.0.1 version. A color-coding scheme is employed to differentiate classes based on their interdependencies. Classes that exhibit mutual calling relationships have been assigned distinct colors, whereas those classes that operate independently of others are denoted in gray. Taking the red-coded EM class as an example, it invokes the **utils** class, hence it has a green color tag. Notably, the **QI** class exhibits dependencies on multiple classes, one of which being the **EM** class, consequently leading to the assignment of a red tag to the **QI** class.

in both Isotropic and anisotropic Media.

Anisotropy: Anisotropy is generally used to describe the properties of the material or systems that are directionally dependent (Newnham, 2005). The Anisotropy class focuses primarily on seismic anisotropy, which concerns the directional dependence of wave velocity and elastic properties of rock. This class includes various models for computing the effective elastic constants and velocities of transversely isotropic (TI) media.

BW: The acronym BW stands for Batzle-Wang (1992) who developed models for predicting the density and bulk moduli of reservoir fluids by combining thermodynamic relationships and empirical trends from published data. The BW class implements the original Batzle-Wang models to compute water, brine, oil, and gas properties at various pressures and temperatures. Additionally, the modified Batzle-Wang equations that yield more accurate CO_2 properties are also included.

EM: Effective medium (EM) models treat rock as a composite of different constituents such as pore and matrix. The EM class includes most well-known EM models that pertain to the theoretical modeling of macroscopic rock properties by incorporating the individual elastic properties, the volume fractions, and the assumed spatial geometry of the different phases that make up the rock. EM models requiring the recursive or iterative computation of the effective properties such as Differential Effective Models (DEM) and Self-Consistent (SC) models are also included. Note that this class is primarily concerned with elastic mixing laws and inclusion effective medium models, while the effective medium models for granular medium are collected in **GM** class.

Empirical: This class contains models that are empirically derived to best fit certain types of data. Examples include the Krief model (Krief et al., 1990) for computing the elasticity of stiff sandstone, the Greenberg-Castagna model for S-wave velocity prediction, and various rock physics depth trends of different lithologies in different sedimentary basins. These models usually have limited ranges of applicability and should be used with consideration.

Fluid: Fluid presence has a significant impact on the effective elastic properties of rocks and the propagation of waves, and it's a crucial aspect of rock physics. This class includes several methods for performing fluid substitutions, as well as various poroelastic models that describe the attenuation and dispersion caused by wave-induced fluid flow.

GM: The study of granular media is essential in rock physics as it plays a crucial role in determining the mechanical and elastic properties of many types of rocks. Sands and sandstones, for example, can be represented by the granular packing of unbounded and bounded clastic particles, respectively. The literature contains numerous models, including theoretical, hybrid, and heuristic models (Avseth et al., 2010b), which have gained popularity in both academia and industry. The

GM class provides a comprehensive collection of these models, including their heuristic extensions, which can be used to model the elastic properties of different lithologies, such as sand-shale mixtures.

Permeability: This class includes the Kozeny-Carman relation (Carman and Machefer, 1961), as well as several empirical estimations of permeability in porous media based on it.

QI: Rock physics plays a crucial role in Quantitative Interpretation (QI) of geophysical measurements. The QI class offers some of the most widely used techniques and newly developed workflows in practice, including rock physics templates, rock physics diagnostics, AVO synthetics, and diagenetic modeling with rock physics constraints.

utils: Short for utilities, contains fundamental functions and tools that are commonly used throughout the entire codebase. These include velocity computation, conversion between elastic modulus and stiffness matrix formulations for isotropic and anisotropic media, as well as other basic functions. The **utils** class helps reduce code duplication and enhances the maintainability of the codebase.

5.3   Illustrative examples

The classes in the API that were previously described mostly consist of different rock physics models. In the **rockphypy** library, all of the rock physics models, except for workflows, are written as static methods within each Python class. This makes it flexible to use the models with or without a dataset, depending on the task at hand. The following examples demonstrate how to use **rockphypy** to perform various rock physics modeling tasks. All of the datasets and scripts used in these examples are available for download from the GitHub repository and ReadTheDocs page of the library.

5.3.1 Rock physics modelling of CO_2 sequestration

CO_2 injection involves injecting carbon dioxide into a storage reservoir, where it usually mixes with the preexisting pore fluids, To monitor the injection process using time-lapsed seismic methods, it is necessary to have knowledge of the seismic properties of the fluid mixture consisting of CO_2 and *in-situ* pore fluid at different reservoir pressures and temperatures.

The acoustic properties of pure carbon dioxide can be computed using different equations of state, depending on the preferred method. Complex models, such as EOS-CG model (Gernert and Span, 2016) based on Helmholtz energy equations of state, provide accurate estimations for both pure and impure CO_2 as a function of temperature and pressure. However, these models require numerical optimization and are usually only available through specialized software.

A common practice is to use the Batzle-Wang equations for gas to compute CO_2 properties. However, this can be highly inaccurate, particularly at higher fluid pressures. Xu (2006) modified the original Batzle-Wang (B-W) equations, making them more accurate for computing CO_2 properties at various P-T conditions. The discrepancy between using the Batzle-Wang equation and its modified version can be easily compared by utilizing the built-in methods in **rockphypy** as follows.

```python
# import the modules
from rockphypy import BW, GM, Fluid
import numpy as np
# Computing bulk modulus and density of
# pure CO2 properties  as a function of pressure
# and temperature.
G = 1.5349  # gas gravity of CO2
pressure = np.linspace(0, 40, 100)
temperature = np.linspace(20, 80, 100)
P, T = np.meshgrid(pressure, temperature)
# new BW prediction
```

```
rho_co2 , K_co2 = BW.rho_K_co2(P, T, G)
# original BW prediction
rho_co2_BW , K_co2_BW = BW.rho_K_gas(P, T, G)
```

The results are shown in Figure 5.2. The new B-W method gives more accurate predictions compared to the original B-W methods, and the discrepancy between the two models exponentially grows as pressure increases.
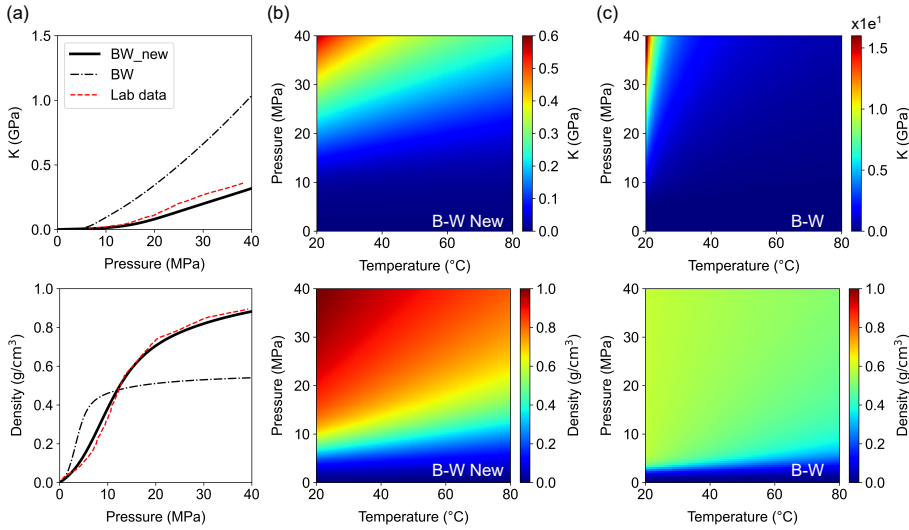

Figure 5.2: (a)Comparison of acoustic properties of CO_2 computed using both the original and modified B-W methods at a temperature of 57°C. The experimental data (Wang and Nur, 1989) of the CO_2 properties are digitized from the reference (Xu, 2006). (b)Bulk modulus and density of pure CO_2 computed using new B-W method at various P-T conditions. (c)The same results computed using the original B-W method for gas.

The following experiment investigates the impact of errors in CO_2 properties on the seismic response of an injected reservoir. The seismic properties of a CO_2-brine mixture are calculated using the Brie fluid mixing method, based on the reservoir temperature, post-injection pore pressure, and known brine salinity. Both the original and modified Batzle-Wang equations are used to calculate the mixture properties. The reservoir is assumed to be homogeneous and isotropic, and a granular medium model is utilized to compute the dry rock properties at the

corresponding effective stress. Finally, the P and S wave velocities of an unconsolidated sandstone reservoir saturated with CO_2-brine mixtures at various levels of CO_2 saturation are calculated using Biot-Gassmann theory.

```python
# Modelling of CO2 sequestration
# in unconsolidated reservoir.
# grain density, bulk and shear modulus
D0, K0, G0 = 2.65, 36, 42
# brine density, bulk modulus
Db, Kb = 1, 2.2
# Reservoir condition and brine salinity
overburden_stress = 40 # MPa
pore_pressure = 20 # MPa
temperature = 45
# effective stress
sigma = overburden_stress - pore_pressure
salinity = 35000/1000000
sw = np.linspace(0, 1, 50) # water saturation
sco2 = 1-sw # CO2 saturation
# Parameter for granular medium
phi_c = 0.4 # critical porosity
Cn = 6 # coordination number
# saturation condition: patchy saturation
brie = 4
# Using softsand model to compute the dry
# rock properties
Kdry, Gdry = GM.softsand(K0, G0, phi_c, phi_c, Cn,
sigma, f=1)
# CO2-brine mixture properties computed using
# original B-W and Brie mixing law
den1, Kf_mix_1 = BW.co2_brine(temperature,
pore_pressure, salinity, sco2, brie_component=brie,
bw=True)
# CO2-brine mixture properties computed using new
# B-W and Brie mixing law
```

```
den2, Kf_mix_2 = BW.co2_brine(temperature,
pore_pressure, salinity, sco2, brie_component=brie,
bw=False)
# Seismic properties of the reservoir rock saturated
# with Brine-CO2 mixture
vp1, vs1, rho1 = Fluid.vels(Kdry, Gdry, K0, D0,
Kf_mix_1, den1, phi_c)# B-W
vp2, vs2, rho2 = Fluid.vels(Kdry, Gdry, K0, D0,
Kf_mix_2, den2, phi_c)# B-W new
```

The impact of CO_2 properties on the modeling of time-lapse effects of CO_2 sequestration is shown in Figure 5.3. The use of **rockphypy** makes it easy and intuitive to perform modeling tasks, enabling users to focus on specific features. It provides great flexibility by allowing users to customize functions with a wide range of pre-built functionalities. In this example, the `BW.co2_brine` method is built upon several basic building blocks to model brine-fluid mixture using patchy mixing.

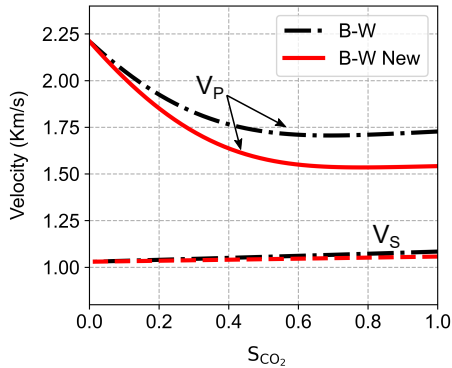**Figure 5.3:** The P and S wave velocities of an unconsolidated sandstone reservoir saturated with CO_2-brine mixture are affected by the accuracy of the CO_2 model. The use of the less accurate B-W gas model leads up to about 15% error in P wave velocity as the CO_2 saturation increases. Mistakes in density calculation of CO_2-brine mixture also impact the shear wave velocity, particularly for high CO_2 saturations.

5.3.2   Rock physics interpretation

Grain contact rock physics models, in combination with fluid substitution, can be utilized for both qualitative and quantitative interpretation tasks (Avseth et al., 2010a). In the following, we demonstrate how to efficiently perform rock physics screening, diagnostics, lithology and fluid predictions using the **rockphypy** with a synthetic dataset. The well-log dataset used in this section is synthesized based on the empirical depth trends for different seismic properties of sandstones in Norwegian offshore.

In practice, given the abundance of well-log measurements, data screening is essential to identify and address any errors, inconsistencies or missing data in the dataset before further analysis is conducted. Figure 5.4a depicts the rock physics screening (Avseth et al., 2021) results for the sandstone data. The elastic bounds generated using contact-based elastic models can determine whether the data is consistent with known principles of physics.

```python
import pandas as pd
from rockphypy import QI
df=pd.read_csv('../../data/well/sandstone.csv')
# grain density, bulk and shear modulus
Dqz, Kqz, Gqz = 2.65, 36.6, 45
# clay density, bulk and shear modulus
Dsh, Ksh, Gsh = 2.7, 21, 7
# cement density, bulk and shear modulus
Dc,Kc, Gc = 2.65, 36.6, 45
Db, Kb = 1, 2.2 # brine density, bulk modulus
phi_c = 0.4 # critical porosity
sigma = 20 # effective pressure
scheme = 2 # cement distribution
Cn = 8.6 # coordination number
vsh = 0 # shale volume
phib = 0.3 # adjust porosity
```

```
f = 0.5 # slip factor
# compute elastic bounds
phi,vp1,vp2,vp3,_,_,_ = QI.screening(Dqz,Kqz,Gqz,
Dsh,Ksh,Gsh,Dc,Kc,Gc,Db,Kb,phib,phi_c,sigma,vsh,
scheme,f, Cn)
# initialize the object
qi = QI(df.VP, phi = df.PHIT_ND,Vsh = df.VSH_GR)
fig_a = qi.screening_plot(phi,vp1,vp2,vp3)
```

Probability density functions can also be applied to provide better visualization of the data, which reveals more information about the distribution of rock properties in certain dataset. Figure 5.4b shows the KDE plot of data generated using the following commands:

```
fig_b = qi.kde_plot(phi,vp1,vp2,vp3)
```

Diagenetic cement is commonly found in reservoir sandstone. The volume of cement can be estimated through rock physics diagnostics using constant cement models. Figure 5.4c displays the estimation for the example dataset, assuming silica cement. The code used to generate the examples is presented below:

```
# estimate cement
vcem_seeds = np.array([0,0.005,0.01,0.02,0.03,0.04,0.1] )
vcem = qi.estimate_cem(vcem_seeds,Kqz,Gqz,Ksh,
Gsh,phi_c,Cn,Kc,Gc,Db,Kb,scheme,vsh,Dsh,Dqz,Dc)
# drawing the constant cement lines
phib_p = [0.3,0.37,0.38,0.39,0.395]
fig_c = qi.cement_diag_plot(vcem,Dqz,Kqz,Gqz,Dsh,Ksh,
Gsh,Dc,Kc,Gc,Db,Kb,phib,phib_p,phi_c,sigma,vsh,Cn, scheme,f)
```

Apart from the aforementioned functionalities, Rock Physics Templates (RPTs) can also be utilized to comprehend the elastic attributes derived from well log data, as depicted in Figure 5.4d. Rock physics models can calculate elastic properties with various combinations of lithology and fluid parameters. Based on these

characteristics, Rock Physics Templates (RPTs) provide a reference framework of all the possible variations of a specific rock with different fluid saturations. RPTs can be constructed using different grain contact models. RPTs can be constructed using various grain contact models. The following code uses the stiffsand model to construct the RPT. By transforming the same data to the RPT domain, it becomes evident that the data are primarily dominated by brine saturated sandstone which comply with the empirical trends used to generate the data.

```python
# stiffsand model
Kdry, Gdry = GM.stiffsand(K0, G0, phi, phi_c, Cn, sigma, f=0)
fig_d = plot_rpt(Kdry,Gdry,K0,D0,Kb,Db,Kg,Dg,phi,sw)
IP= df.VP*df.DEN
PS= df.VP/df.VS
plt.scatter(IP,PS,c=df.eff_stress,edgecolors='grey',
s=80,alpha=1,cmap='Greens_r')
```

5.4   Impact

Rock physics is a broad field of research with a wide range of applications. As demonstrated by previous examples, **rockphypy** is a versatile and flexible Python library that enables users to perform various modeling tasks simply and efficiently while avoiding the hard-coding of many rock physics models and workflows.

Introducing this Python library is instrumental in its adoption by modern researchers seeking to perform sophisticated tasks in rock physics, leveraging the Python infrastructure for statistical and machine learning inference. To our knowledge, **rockphypy** is the first publicly available Python library that provides comprehensive and easy-to-use functionalities in rock physics. Our long-term goal is to standardize base-level rock physics modeling using **rockphypy**, making it a go-to tool for the research community.

rockphypy has already been utilized as teaching material for Reservoir seismic at
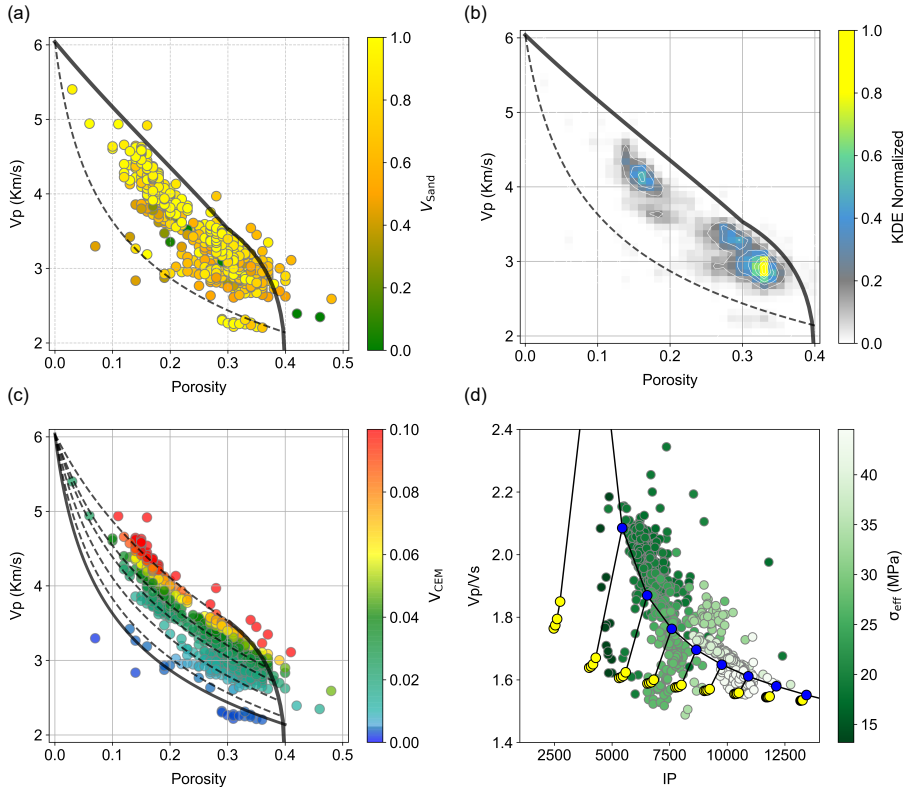
Figure 5.4: (a)Rock physics screening using elastic bounds. (b)2-D KDE plot of the data within elastic bounds defined by several rock physics models. (c)Cement amount estimation using constant cement model. (d)Rock physics template overlain the data.

NTNU since 2022, reaching out to a broad audience beyond the authors' research group. The library is also currently being used in the authors' ongoing project, as mentioned in the Acknowledgments section. The research paper has utilized **rockphypy** to build new rock physics models and there are other papers under revision or in preparation where **rockphypy** is presented.

5.5 Conclusion

We present an extensive yet easy-to-use Python library **rockphypy** for rock physics modeling. It offers a toolbox for computing elastic properties of rock, fluid, and their interactions under various conditions. The built-in workflows also

simplify the process of performing broadband data analysis tasks. The library is created in a modular fashion which allows users to customize functions using pre-built functionalities, build workflows, and easily extend the library's applicability by incorporating new models. We foresee contributions from across different areas of geoscientific research and practice where rock physics modeling is involved.

Current work focuses on expanding the test case suite for automated testing. We strive to maintain the readability and reliability of the codebase while continuously enriching the library's capabilities through both internal and external contributions that adhere to strict contribution guidelines.

5.6   Acknowledgements

6.1   Summary

This thesis is centered on three main objectives: (1) Understanding and modeling the influence of effective stress release on the elastic properties of high-porosity cemented sandstone through the introduction of a novel rock physics model. (2) Systematically elucidating the practical implications of stress release in applications related to high-porosity cemented sandstone. (3) Advocating for the open-source movement within the field of rock physics to improve accessibility, transparency, and innovation in both research and practical applications.

In paper 1, a novel rock physics model was developed for predicting the deterioration of stiffness during stress release in high-porosity cemented sandstone, based on the patchy cement model. In theory, the decreasing elastic properties and subsequent wave velocity changes are associated with the breakage and crumbling of contact cement, thereby weakening the original contact cement network. Additionally, a sequential modeling scheme was proposed, allowing the accurate modeling of elastic properties in partially cemented sandstone under both stress application and reduction. The modeling results successfully replicate experimental measurements in cemented glass bead packs and sandstone. The sequential calibration workflow not only provides a valuable tool for quantifying velocity changes with effective stress but also offers insights into the rock's coherence. The understanding

and theoretical developments acquired in paper 1 were applied in papers 2 and 3 to further elucidate the practical impact of stress release on sandstone with partial cement. In paper 2, a measure of stress release, termed porosity inconsistency, was proposed through integrated rock physics and diagenetic modeling guided by burial history. An extensive database of clean Jurassic sandstone from both the Norwegian Sea and Barents, spanning a wide range of burial depths, was established. By utilizing porosity inconsistency, it was demonstrated that the compressive velocity of sandstone in exhumed regions of the Norwegian Sea and Barents Sea is more affected by exhumation compared to porosity. The extent of stress release impact correlates positively with the magnitude of exhumation. Importantly, it was shown for the first time that relying solely on velocity-depth trends may lead to underestimated exhumation magnitudes. These results highlight the limitations of using velocity alone for exhumation estimation, emphasizing the importance of considering stress release, cementation, and their interactions in future work. Additionally, this study suggests that the inconsistent variation in elastic stress sensitivity and acoustic stress sensitivity due to stress release is critical for understanding core damage evaluation, predicting pore pressure, interpreting time-lapse seismic data, and assessing the feasibility of fluid injection in reservoir rocks in areas with significant exhumation. Additionally, this study suggests that the inconsistent variation in elastic stress sensitivity and acoustic stress sensitivity due to stress release is critical for understanding core damage evaluation, predicting pore pressure, interpreting time-lapse seismic data, and assessing the feasibility of fluid injection in reservoir rocks in areas with significant exhumation. In paper 3, a comprehensive comparison was conducted between the acoustic and elastic properties variation in unconsolidated sand and weakly cemented sandstone, in both normally consolidated and overconsolidated states. The results provide crucial insights into sandstone stress sensitivity. Specifically, in comparison to unconsolidated sands, the presence of contact cement reduces porosity's responsiveness to stress while enhancing velocity sensitivity to stress reduction. Unlike unconsolidated sands,

166

the V_P/V_S in weakly cemented sandstone is stress path dependent. Well-log data from the Norwegian Sea and Barents Sea align with experimental findings. The study underscores the importance of considering cement presence and alterations during stress release. The results emphasize the necessity of selecting appropriate models based on rock type and consolidation state when studying reservoir sandstone. Neglecting improved stress sensitivity in velocity during stress release can impede the accuracy of time-lapsed monitoring and fluid saturation estimation in overconsolidated, cement-containing porous rock formations.

Finally, in paper 4, an extensive Python rock physics library was developed and is publicly available. With this library, many models and workflows, including those developed in this dissertation, can be conveniently applied in both research and practical tasks. This library has garnered attention in both industry and academia, with more than 2,000 downloads as of the completion of this thesis. The author of this thesis believes that embracing open-source practices can foster a more inclusive and cooperative community, enabling researchers and professionals to share, modify, and contribute to advancements in rock physics modeling and analysis. It is therefore sincerely hoped to see more open-source initiatives emerging in the field of rock physics.

6.2   Recommendation for future research

- **From isotropy to anisotropy**

The impact of successive stress application and stress release on elastic anisotropy is unexplored in this dissertation. In Paper 1, the experimental data of the synthetic sandstone reveals a direct link between the decrease in wave velocities and the decrease in effective stress. Notably, alongside the observation of stress release-induced weakening, an intriguing finding involves the reversal of P-wave anisotropy, shifting from negative to positive upon stress release. Further detailed

descriptions of the phenomenon are documented in Torset et al. (2020). Paper 2 utilizes an extensive well-log dataset to demonstrate that stress release associated with uplift weakens the rock. However, a notable gap exists in field data replication for the observed reversal of P-wave anisotropy. Consequently, future research endeavors could focus on providing empirical evidence through field data to ascertain whether stress release can indeed trigger the reversal of P-wave anisotropy. Taking a cue from the approach used in Paper 2, a similar well-log database of stress-dependent anisotropy could be established in an uplifted area and its reference area. An approach worth adopting for dataset building is the work by Teng and Sams (2023), who investigated depth-dependent P-wave anisotropy and its impact on AVO interpretation in the Northern Malay Basin. One foreseeable challenge is acquiring a sufficient amount of data, as deviated wells with varying penetration depths are required to estimate anisotropy parameters fieldwise.

- **From comprehension to prediction**

This dissertation focuses primarily on understanding the impact of stress release on the elastic properties of sandstone and its consequential effects on the seismic rock physics workflows. The knowledge acquired through this research is generic and applicable across various domains, including petroleum exploration, reservoir monitoring, subsurface storage, and basin modeling. In future work, investigating the incorporation of stress release in practical inversion tasks is highly valuable. For instance, commonly used rock physics models in petrophysical seismic inversion and Bayesian inversion often neglect the stress release-induced weakening of the rock. While this might not pose a significant limitation for studying reservoirs that haven't experienced substantial stress release, it becomes a critical problem in cases such as stuying uplifted areas and overpressured zones. Because a stress-muted inversion workflow in such situations may lead to erroneous inversion results. Therefore, it is worthwhile to develop an inversion scheme (e.g., bayesian) for the entire PCM-VPCM workflow, providing flexibility in studying both nor-

mally stressed areas and areas affected by stress release. Note that the linearization of the PCM and VPCM is complicated by the use of the contact cement model and nested Hashin Strikmann bounds with strong nonlinearity. To mitigate this, piecewise linearization and approximations such as the bounds proposed by Avseth et al. (2013) can be employed.

- **From geomechanical to geochemical effects**

The rock physics model VPCM, developed in Paper 1, may offer insights into the seismic response of cement dissolution in siliciclastic rocks triggered by processes like CO_2 injection. Originally, cement crumbling in VPCM describes the detachment of stress-bearing cement from the cement network, transforming it into non-stress-bearing intergranular fragments. This overall implies a reduction in the volumetric percentage of effective contact cement. In literature, the constant cement Model is commonly used for qualitative interpretation of CO_2-dissolved reservoir rock. Typically, data is plotted in the porosity-VP domain overlaid by rock physics models computed at different amounts of cement and a fixed effective stress level. Compared to the constant cement model, VPCM enables a quantitative study of the seismic response to CO_2 sequestration-induced chemical dissolution. More importantly, the stress evolution can be also incorporated into the interpretation workflow. Therefore, future application of the VPCM to rock physics analysis of geochemical effects in CO_2-flooded reservoir rocks is intriguing.

- **Towards full physics**

The emphasis of our research lies in understanding and approaching stress release from the perspective of rock physics. By treating sandstone as an effective granular medium, we extend existing rock physics models to describe changes in stress sensitivity during stress removal in patchy cement sandstone. The practical applications of our proposed modeling approach are likely confined to the realms of seismic exploration and interpretation. However, it's important to note that our

model only covers partial physics. The cement breakage associated with stress release, studied in this dissertation, reflects the inelasticity of partially cemented granular materials. Menendez et al. (1996) pointed out that, in addition to cement damage, inelasticity is also influenced by grain crushing and fragment reorganization—factors not considered in our model. To fully capture the physical processes of rock undergoing stress release, the ultimate solution lies in constructing constitutive models based on the elastoplastic framework. Material science literature indicates that heavily cemented granular media can be well-described by classical breakage mechanics theory. For weakly to moderately cemented granular media, different failure mechanisms need incorporation into the constitutive model. This, however, is beyond the scope of this dissertation. For readers interested in the subject and who have read up to this point, we recommend exploring the following articles as a starting point. These articles provide a fresh perspective on similar issues, approaching them from the angles of failure mechanics and numerical simulation.

APPENDICES

171

Introduction

Uplift estimation using seismic and sonic log data commonly assumes no change in velocities as rocks undergo stress relaxation. However, experimental studies on core damage have shown that breaking of grain contact cement upon coring leads to a significant reduction in velocities. Numerical simulation by Holt et al. (2004) has shown that uplift also causes bonding cement breakage. Ignoring such stress sensitivity of cemented sandstone may greatly underestimate the magnitude of uplift estimation. However, few models have been proposed to predict the stress-dependent velocities of rocks upon stress release. Bredesen et al. (2019) introduced weakness to tight cemented sandstone by combining the contact cement model with DEM theory incorporating a crack-like inclusion geometry in the low porosity range, thus achieving more consistent velocity predictions compared to observed data. Torset et al. (2021) applied a modified anisotropic crack model from Fjaer (2006) to fit the measured compressional wave velocities of weakly cemented synthetic sandstone during simulated uplift. The increased stress sensitivity upon uplift can be well explained, but the complicated forward modeling, plentiful controlling parameters, and the need for accurate determination of radial P wave velocity limit the generalization of the approach. In this work, we propose a model to quantify the stress sensitivity of cemented sandstone undergoing unloading by modifying the Patchy Cement Model (PCM) as proposed by Avseth et al. (2016). We derived the premise that the weakness can be introduced to cemented rock by varying the degree of patchiness of the patchy cemented sandstone. A diluting parameter is introduced to show how much of the connected patchy cement has been replaced by disconnected patchy cement. The diluting parame-

172

ter can be made either stress-dependent or stress-independent. By combining the experimental evidence, we identify that the crushing of brittle cement will also contribute to the deterioration of the rock stiffness, and further increase the stress sensitivity. We demonstrate how the Varying Patchiness Cement Model (VPCM) can further incorporate the crushing effect by reducing the effective stress loading cement amount. We show that the laboratory experimental loading and unloading data can be well replicated and the observed stress sensitivity upon unloading can be predicted with few model parameters.

Introduction

Pore pressure increases during CO_2 injection are expected to be small to avoid initiations of stress-induced fractures. However, pressure is likely to build up due to complex geology, heterogeneity, constrained reservoir volume, etc. (Lumley, 2019). The existing rock physics models that honor the stress sensitivity in sands/sandstones are restricted to contact theory for unconsolidated sands and crack/pore shape models for well-consolidated sandstones (Shapiro, 2003; Vernik and Hamman, 2009). Few models have been proposed to describe the stress sensitivity variation upon stress release in high porosity cemented sandstone that can be also utilized as CO_2 storage formation. This type of reservoir rock may be irreversibly altered by geomechanical effects caused by pore pressure variation during injection. One of these effects is the weakening of the contact cement. Yu et al. (2021) developed a rock physics model which quantifies the stress sensitivity of weakly to moderately cemented sandstone upon stress release by considering cement bond breakage. We demonstrate model calibration using field data measurements and forward modeling combining saturation and geomechanical effects at both well log and seismic scales. The time-lapse seismic modeling indicates that the geomechanical effect caused by pressure transients may be observable as strong 4D AVO differences caused by the reduction of P- and S- wave velocities.

REFERENCES

Ahmed, Z., and M. Lebedev, 2019, Elastic properties of sands, Part 2: Implementation of contact-based model to determine the elasticity of the grains from ultrasonic measurements: Geophysical Prospecting, 67, 4, 745–760.

Al Hosni, M., S. Vialle, B. Gurevich, and T. M. Daley, 2016, Estimation of rock frame weakening using time-lapse crosswell: The Frio brine pilot project: Geophysics, 81, 6, B235–B245.

Al-Chalabi, M., 2001, The use of instantaneous velocity in uplift investigations: Geophysical Prospecting, 49, 6, 645–655.

Alvarado, G., M. R. COOP, and S. Willson, 2012, On the role of bond breakage due to unloading in the behaviour of weak sandstones: Géotechnique, 62, 4, 303–316.

Amato del Monte, A., 2017, Seismic rock physics: The Leading Edge, 36, 523–525.

Andò, E., G. Viggiani, S. Hall, and J. Desrues, 2013, Experimental micro-mechanics of granular media studied by X-ray tomography: recent results and challenges: Géotechnique Letters, 3, 3, 142–146.

Andrä, H., N. Combaret, J. Dvorkin, E. Glatt, J. Han, M. Kabel, Y. Keehm, F. Krzikalla, M. Lee, C. Madonna, et al., 2013, Digital rock physics benchmarks—Part I: Imaging and segmentation: Computers & Geosciences, 50, 25–32.

Athy, L. F., 1930, Density, porosity, and compaction of sedimentary rocks: AAPG Bulletin, 14, 1, 1–24.

Avseth, P., and I. Lehocki, 2016, Combining burial history and rock-physics modeling to constrain AVO analysis during exploration: The Leading Edge, 35, 6, 528–534.

Avseth, P., and N. Skjei, 2011, Rock physics modeling of static and dynamic reservoir properties — A heuristic approach for cemented sandstone reservoirs: The Leading Edge, 30, 1, 90–96.

Avseth, P., I. Lehocki, Ø. Kjøsnes, and O. Sandstad, 2021, Data-driven rock physics analysis of North Sea tertiary reservoir sands: Geophysical Prospecting, 69, 608– 621.

Avseth, P., N. Skjei, and G. Mavko, 2016, Rock-physics modeling of stress sensitivity and 4D time shifts in patchy cemented sandstones — Application to the Visund Field, North Sea: The Leading Edge, 35, 10, 868–878.

Avseth, P., N. Skjei, and Å. Skålnes, 2013, Rock physics modelling of 4D time-shifts and time-shift derivatives using well log data — A North Sea demonstration: Geophysical Prospecting, 61, 2, 380–390.

Avseth, P., T. A. Johansen, A. Bakhorji, and H. M. Mustafa, 2014, Rock-physics modeling guided by depositional and burial history in low-to-intermediate-porosity sandstones: Geophysics, 79, 2, D115–D121.

Avseth, P., T. Mukerji, and G. Mavko, 2010a, Quantitative seismic interpretation: Applying rock physics tools to reduce interpretation risk: Cambridge University Press.

Avseth, P., T. Mukerji, G. Mavko, and J. Dvorkin, 2010b, Rock-physics diagnostics of depositional texture, diagenetic alterations, and reservoir heterogeneity in

high-porosity siliciclastic sediments and rocks — A review of selected models and suggested workflows: Geophysics, 75, 5, 75A31–75A47.

Bachrach, R., and P. Avseth, 2008, Rock physics modeling of unconsolidated sands: Accounting for nonuniform contacts and heterogeneous stress fields in the effective media approximation with applications to hydrocarbon exploration: Geophysics, 73, 6, E197-E209.

Bachrach, R., M. Sengupta, A. Salama, and P. Miller, 2009, Reconstruction of the layer anisotropic elastic parameters and high-resolution fracture characterization from P-wave data: a case study using seismic inversion and Bayesian rock physics parameter estimation, Geophysical prospecting, 57, 2, 253-262.

Baig, I., J. I. Faleide, J. Jahren, and N. H. Mondol, 2016, Cenozoic exhumation on the southwestern Barents Shelf: Estimates and uncertainties constrained from compaction and thermal maturity analyses: Marine and Petroleum Geology, 73, 105–130.

Batzle, M., and Z. Wang, 1992, Seismic properties of pore fluids: Geophysics, 57, 1396–1408.

Bergan, M., and R. Knarud, 1993, Apparent changes in clastic mineralogy of the Triassic–Jurassic succession, Norwegian Barents Sea: possible implications for palaeodrainage and subsidence, in Norwegian Petroleum Society Special Publications: Elsevier, 2, 481–493.

Bernabé, Y., D. Fryer, and J. Hayes, 1992, The effect of cement on the strength of granular rocks: Geophysical Research Letters, 19, 14, 1511–1514.

Berryman, J. G., 1992, Single-scattering approximations for coefficients in Biot's equations of poroelasticity: The Journal of the Acoustical Society of America, 91, 2, 551–571.

Bjørlykke, K., and J. Jahren, 2010, Sandstones and sandstone reservoirs. in K. Bjørlykke, Petroleum Geoscience: From sedimentary environments to rock physics: Springer, 113–140.

Bjørlykke, K., and K. Høeg, 1997, Effects of burial diagenesis on stresses, compaction and fluid flow in sedimentary basins: Marine and Petroleum Geology, 14, 3, 267-276.

Branch, M. A., T. F. Coleman, and Y. Li, 1999, A subspace, interior, and conjugate gradient method for large-scale bound-constrained minimization problems: SIAM Journal on Scientific Computing, 21, 1, 1–23.

Bredesen, K., P. Avseth, T. A. Johansen, and R. Olstad, 2019, Rock physics modelling based on depositional and burial history of Barents Sea sandstones: Geophysical Prospecting, 67, 4, 825–842.

Bredesen, K., R. Rasmussen, A. Mathiesen, and L. H. Nielsen, 2021, Seismic ampli- tude analysis and rock physics modeling of a geothermal sandstone reservoir in the southern part of the Danish Basin: Geothermics, 89, 101974.

Capello de P, M. A. and M. Batzle, 1997, Rock physics in seismic monitoring: The Leading Edge, 16, 9, 1255-1260.

Caputo, M., and J. M. Carcione, 2011, Hysteresis cycles and fatigue criteria using anelastic models based on fractional derivatives: Rheologica Acta, 50, 2, 107–115.

Carman, P. C., and J. Machefer, 1961, L''ecoulement des gaz a' travers les milieux poreux: Paris: Bibliotheeque des Sciences et Techniques Nucleaires, Presses Uni- versitaires de France.

Chuhan, F. A., A. Kjeldstad, K. Bjørlykke, and K. Høeg, 2002, Porosity loss in sand by grain crushing — Experimental evidence and relevance to reservoir

quality: Marine and Petroleum Geology, 19, 1, 39–53.

Corcoran, D., and A. Doré, 2005, A review of techniques for the estimation of magnitude and timing of exhumation in offshore basins: Earth-Science Reviews, 72, 3–4, 129–168.

Daley, T. M., 2019, Rock physics of CO_2 storage monitoring in porous media, in: T. L. Davis, M. Landrø, M. Wilson (Eds.), Geophysics and Geosequestration, Chapter 4, Cambridge University Press, p. 71–82.

Daley, T. M., L. R. Myer, J. Peterson, E. Majer, and G. Hoversten, 2008. Time-lapse crosswell seismic and VSP monitoring of injected CO_2 in a brine aquifer: Environmental Geology, 54, 1657-1665.

Digby, P. J., 1981, The Effective Elastic Moduli of Porous Granular Rocks: Journal of Applied Mechanics, 48, 4, 803-808.

Ding, Y., A. Qian, H. Lu, Y. Li, and Y. Zhang, 2022, DEM investigation of the effect of hydrate morphology on the mechanical properties of hydrate-bearing sands: Computers and Geotechnics, 143, 104603.

Dong, J. J., J. Y. Hsu, W. J. Wu, T. Shimamoto, J. H. Hung, E. C. Yeh, Y. H. Wu, and H. Sone, 2010, Stress-dependence of the permeability and porosity of sandstone and shale from TCDP Hole-A: International Journal of Rock Mechanics and Mining Sciences, 47, 7, 1141–1157.

Doré, A., and L. Jensen, 1996, The impact of late Cenozoic uplift and erosion on hydrocarbon exploration: offshore Norway and some other uplifted basins: Global and Planetary Change, 12 no.1–4, 415–436.

Duffaut, K., and M. Landrø, 2007, V_P/V_S ratio versus differential stress and rock consolidation—A comparison between rock models and time-lapse AVO data: Geophysics, 72, 5, C81-C94.

Duffaut, K., M. Landrø, and R. Sollie, 2010, Using Mindlin theory to model friction-dependent shear modulus in granular media: Geophysics, 75, 3, E143–E152.

Duffaut, K., P. Avseth, and M. Landrø, 2011, Stress and fluid sensitivity in two North Sea oil fields — Comparing rock physics models with seismic observations: The Leading Edge, 30, 1, 98–102.

Dupuy, B., S. Garambois, A. Asnaashari, H. M., M. Landrø, A. Stovas, and J. Virieux, 2016, Estimation of rock physics properties from seismic attributes—Part 2: Applications: Geophysics, 81, 4, M55-M69.

Dupuy, B., A. Romdhane, P. Eliasson, E. Querendez, H. Yan, V. A. Torres, and A. Ghaderi, 2017, Quantitative seismic characterization of CO_2 at the Sleipner storage site, North Sea. Interpretation, 5, 4, SS23-SS42.

Duran, E. R., R. di Primio, Z. Anka, D. Stoddart, and B. Horsfield, 2013, 3D-basin modelling of the Hammerfest Basin (southwestern Barents Sea): A quantitative assessment of petroleum generation, migration and leakage: Marine and Petroleum Geology, 45, 281–303.

Dutta, T., G. Mavko, and T. Mukerji, 2010, Improved granular medium model for unconsolidated sands using coordination number, porosity, and pressure relations: Geophysics, 75, 2, E91–E99.

Dvorkin, J., and A. Nur, 1996, Elasticity of high-porosity sandstones: Theory for two North Sea data sets: Geophysics, 61, 5, 1363–1370.

Dvorkin, J., and H. Yin, 1995, Contact laws for cemented grains: Implications for grain and cement failure: International Journal of Solids and Structures, 32, 17–18, 2497–2510.

Eberhart-Phillips, D., M. Reyners, M. Chadwick, and J.-M. Chiu, 2005, Crustal heterogeneity and subduction processes: 3-D Vp, V_P/V_S and Q in the south-

ern North Island, New Zealand: Geophysical Journal International, 162, 1, 270-288.

Ehrenberg, S., 1990, Relationship between diagenesis and reservoir quality in sandstones of the Garn Formation, Haltenbanken, mid-Norwegian continental shelf: AAPG Bulletin, 74, 10, 1538–1558.

Fairhurst, C., 2003, Stress estimation in rock: a brief history and review: International Journal of Rock Mechanics and Mining Sciences, 40, 7–8, 957–973.

Fawad, M., N. H. Mondol, J. Jahren, and K. Bjørlykke, 2011, Mechanical compaction and ultrasonic velocity of sands with different texture and mineralogical composition: Geophysical Prospecting, 59, 4, 697-720.

Firdaus, G., J. Behura, and M. Prasad, 2022, Pressure-dependent elastic anisotropy: A Bakken petroleum system case study: Geophysics, 87, 3, MR139-MR150.

Fjær, E., 2006, Modeling the stress dependence of elastic wave velocities in soft rocks: Presented at the 41st U.S. Symposium on Rock Mechanics, American Rock Mechanics Association.

Fjær, E., R. M. Holt, P. Horsrud, and A. M. Raaen, 2008, Petroleum related rock mechanics: Elsevier.

Flottmann, T., D. Campagna, R. Hillis, and D. Warner, 2004, Horizontal microfractures and core discing in sandstone reservoirs, Cooper Basin, Australia.

Fonseca, J., P. Bésuelle, and G. Viggiani, 2013, Micromechanisms of inelastic deformation in sandstones: an insight using x-ray micro-tomography: Géotechnique Letters, 3, 2, 78-83.

Fortin, J., Y. Guéguen, and A. Schubnel, 2007, Effects of pore collapse and grain

crushing on ultrasonic velocities and V_P/V_S: Journal of Geophysical Research: Solid Earth, 112, B8.

Gaiser, J. E. ,1996, Multicomponent V_P/V_S correlation analysis: Geophysics, 61, 4, 1137-1149.

García, X., and E. A. Medina, 2006, Hysteresis effects studied by numerical simulations: Cyclic loading-unloading of a realistic sand model: Geophysics, 71, 2, F13–F20.

Gassmann, F., 1951, Elastic waves through a packing of spheres: Geophysics, 16, 4, 673–685.

Gernert, J., and R. Span, 2016, EOS–CG: A Helmholtz energy mixture model for humid gases and CCS mixtures: The Journal of Chemical Thermodynamics, 93, 274–293.

Grana, D., 2016, Bayesian linearized rock-physics inversion: Geophysics, 81, D625–D641.

Giles, M., S. Indrelid, and D. James, 1998, Compaction—the great unknown in basin modelling: Geological Society, London, Special Publications, 141, 1, 15–43.

GNU General Public License, 2007, version 3 (Last retrieved 2020-01-01).

Grana, D., S. Verma, J. Pafeng, X. Lang, H. Sharma, W. Wu, F. McLaughlin, E. Campbell, K. Ng, and V. Alvarado, 2017, A rock physics and seismic reservoir characterization study of the Rock Springs Uplift, a carbon dioxide sequestration site in Southwestern Wyoming: International Journal of Greenhouse Gas Control, 63, 296-309.

Hamada, G., 2004, Reservoir fluids identification using V_P/V_S ratio? Oil & Gas Science and Technology, 59, 6, 649-654.

Hamilton, E. L., 1979, V p/V s and Poisson's ratios in marine sediments and rocks: The Journal of the Acoustical Society of America, 66, 4, 1093-1101.

Han, T., S. Liu, L. Y. Fu, and H. Yan, 2021, Understanding how overpressure affects the physical properties of sandstones: Geophysics, 86, 4, MR203-MR210.

Hansen, S., 1997, Quantification of net uplift and erosion on the Norwegian Shelf south of 66 N from sonic transit times of shale: Oceanographic Literature Review, 44, 7, 696–697.

Hansen, H.N., K. Løvstad, R. Müller, and J. Jahren, 2017, Clay coating preserving high porosities in deeply buried intervals of the Stø Formation: Marine and Petroleum Geology, 88, 648-658.

Hashin, Z., and S. Shtrikman, 1963, A variational approach to the theory of the elastic behaviour of multiphase materials: Journal of the Mechanics and Physics of Solids, 11, 2, 127–140.

Henriksen, E., H. Bjørnseth, T. Hals, T. Heide, T. Kiryukhina, O. Kløvjan, G. B. Larssen, A. Ryseth, K. Rønning, and K. Sollid, 2011, Uplift and erosion of the greater Barents Sea: impact on prospectivity and petroleum systems: Geological Society, London, Memoirs, 35, 1, 271–281.

Hertz, H., 1882, Über die Berührung fester elastischer Körper: Journal fur die reine und angewandte Mathematik, 92, 156–171.

Hill, R., 1963, Elastic properties of reinforced solids: some theoretical principles: Journal of the Mechanics and Physics of Solids, 11, 5, 357–372.

Hillis, R. R., 1995, Quantification of Tertiary exhumation in the United Kingdom southern North Sea using sonic velocity data: AAPG Bulletin, 79, 1, 130–152.

Holt, R. M., and J. F. Stenebråten, 2013, Controlled laboratory experiments to assess the geomechanical influence of subsurface injection and depletion processes on 4D seismic responses: Geophysical Prospecting, 61, 476–488.

Holt, R. M., O.-M. Nes, and E. Fjær, 2005, In-situ stress dependence of wave velocities in reservoir and overburden rocks: The Leading Edge, 24, 12, 1268–1274.

Holt, R., J. Stenebråten, and M. Brignoli, 2014, Effects of cementation on in situ and core compaction of soft sandstone. Presented at the 48th US Rock Mechanics/Geomechanics Symposium, American Rock Mechanics Association.

Holt, R., M. Brignoli, and C. Kenter, 2000, Core quality: quantification of coring-induced rock alteration: International Journal of Rock Mechanics and Mining Sciences, 37, 6, 889–907.

Huang, W. L., J. M. Longo, and D. R. Pevear, 1993, An experimentally derived kinetic model for smectite-to-illite conversion and its use as a geothermometer: Clays and Clay Minerals, 41, 2, 162–177.

Huffman, A. R., and J. P. Castagna, 2001, The petrophysical basis for shallow-water flow prediction using multicomponent seismic data: The Leading Edge, 20, 9, 1030-1052.

Japsen, P., 1998, Regional velocity-depth anomalies, North Sea Chalk: a record of overpressure and Neogene uplift and erosion: AAPG bulletin, 82, 11, 2031–2074.

Japsen, P., 2000, Investigation of multi-phase erosion using reconstructed shale trends based on sonic data. Sole Pit axis, North Sea: Global and Planetary Change, 24, 3–4, 189–210.

Japsen, P., and J. A. Chalmers, 2000, Neogene uplift and tectonics around the North Atlantic: overview: Global and Planetary Change, 24, 3–4, 165–173.

Japsen, P., T. Mukerji, and G. Mavko, 2007, Constraints on velocity-depth trends from rock physics models: Geophysical Prospecting, 55, 2, 135–154.

Jaya, M. S., S. A. Shapiro, L. H. Kristinsdóttir, D. Bruhn, H. Milsch, and E. Spangenberg, 2010, Temperature dependence of seismic properties in geothermal rocks at reservoir conditions: Geothermics, 39, 115–123.

Johnston, D. H., 1987, Physical properties of shale at temperature and pressure: Geophysics, 52, 10, 1391–1401.

Kastner, M. and J.M. Gieskes, 1983, Opal-A to opal-CT transformation: a kinetic study. In Developments in Sedimentology, Elsevier, 36, 211-227.

Katahara, K., 2006, Overpressure and shale properties: Stress unloading or smectite-illite transformation? 76th annual International Meeting, SEG, Expanded Abstracts, 1520–1524.

Khutorskoi, M., K. Viskunova, L. Podgornykh, O. Suprunenko, and V. Akhmedzyanov, 2008, A temperature model of the crust beneath the Barents Sea: Investigations along geotraverses: Geotectonics, 42, 2, 125–136.

King, M. S., 2009, Recent developments in seismic rock physics: International Journal of Rock Mechanics and Mining Sciences, 46, 8, 1341-1348.

Kozhagulova, A., A. Shabdirova, G. Tokazhanov, and N. Minh, 2018, Bond Characteristics of Artificial Sandstones with sodium silicate cement. Paper presented at the 52nd US Rock Mechanics/Geomechanics Symposium, OnePetro.

Kozhagulova, A., N. H. Minh, Y. Zhao, and S. C. Fok, 2020, A study on bond breakage behavior of weak Cretaceous Kazakhstani reservoir sandstone analogue: Geomechanics for Energy and the Environment, 21, 100159.

Krief, M., J. Garat, J. Stellingwerff, and J. Ventre, 1990, A petrophysical inter-

pretation using the velocities of P and S waves (full-waveform sonic): The Log Analyst, 31.

Ktenas, D., E. Henriksen, I. Meisingset, J. K. Nielsen, and K. Andreassen, 2017, Quantification of the magnitude of net erosion in the southwest Barents Sea using sonic velocities and compaction trends in shales and sandstones: Marine and Petroleum Geology, 88, 826–844.

Ktenas, D., I. Meisingset, E. Henriksen, and J. K. Nielsen, 2019, Estimation of net apparent erosion in the SW Barents Sea by applying velocity inversion analysis: Petroleum Geoscience, 25, 2, 169–187.

Laberg, J. S., K. Andreassen, and T. O. Vorren, 2012, Late Cenozoic erosion of the high-latitude southwestern Barents Sea shelf revisited. Bulletin, 124, 77–88.

Lander, R. H., and O. Walderhaug, 1999, Predicting porosity through simulating sandstone compaction and quartz cementation: AAPG Bulletin, 83, 3, 433-449.

Langlois, V., and X. Jia, 2014, Acoustic probing of elastic behavior and damage in weakly cemented granular media: Physical Review E, 89, 2, 023206.

Lasabuda, A. P., N. S. Johansen, J. S. Laberg, J. I. Faleide, K. Senger, T. A. Rydningen, H. Patton, S. -M. Knutsen, and A. Hanssen, 2021, Cenozoic uplift and erosion of the Norwegian Barents Shelf–A review: Earth-Science Reviews, 217, 103609.

Lasabuda, A., J. S. Laberg, S. -M. Knutsen, and G. Høgseth, 2018, Early to middle Cenozoic paleoenvironment and erosion estimates of the southwestern Barents Sea: Insights from a regional mass-balance approach: Marine and Petroleum Geology, 96, 501–521.

Lehocki, I., and P. Avseth, 2021, From cradle to grave: how burial history controls

the rock-physics properties of quartzose sandstones: Geophysical Prospecting, 69, 3, 629–649.

Lehocki, I., P. Avseth, and N. H. Mondol, 2020, Seismic methods for fluid discrimination in areas with complex geologic history—A case example from the Barents Sea: Interpretation, 8, 1, SA35–SA47.

Leveille, P., M. Sepehri, and D.B. Apel, 2017, Rockbursting potential of kimberlite: a case study of Diavik diamond mine: Rock Mechanics and Rock Engineering, 50, 12, 223-3231.

Licciardi, A., K. Gallagher, and S. Clark, 2020, Estimating uncertainties on net erosion from well-log porosity data: Basin Research, 32, 1, 51–67.

Løvstad, K., H. N. Hansen, and J. Jahren, 2022, The porosity preserving effect of basin wide illitic coating in deeply buried sandstone intervals of the lower Jurassic Stø Formation, Barents Sea: Marine and Petroleum Geology, 137, 105498.

Lumley, D., 2010, 4D seismic monitoring of CO_2 sequestration: The Leading Edge, 29, 2, 150-155.

Lumley, D., 2019, The Role of Geophysics in Carbon Capture: Geophysics and Geosequestration, 12.

Luo, X., and G. Vasseur, 1995, Modelling of pore pressure evolution associated with sedimentation and uplift in sedimentary basins: Basin Research, 7, 1, 35–52.

Magara, K., 1980, Comparison of porosity-depth relationships of shale and sandstone: Journal of Petroleum Geology, 3, 2, 175–185.

Makse, H. A., N. Gland, D. L. Johnson, and L. Schwartz, 2004, Granular packings:

Nonlinear elasticity, sound propagation, and collective relaxation dynamics: Physical Review E, 70, 6, 061302.

Marigo, J., 1985, Modelling of brittle and fatigue damage for elastic material by growth of microvoids: Engineering Fracture Mechanics, 21, 4, 861–874.

Marion, D. P. 1990. Acoustical, mechanical, and transport properties of sediments and granular materials: Ph.D. thesis, Stanford University.

Marion, D., and A. Nur, 1991, Pore-filling material and its effect on velocity in rocks: Geophysics, 56, 2, 225–230.

Masri, M., M. Sibai, J. F. Shao, and M. Mainguy, 2014, Experimental investigation of the effect of temperature on the mechanical behavior of Tournemire shale: International Journal of Rock Mechanics and Mining Sciences, 70, 185–191.

Mavko, G., and D. Jizba, 1991, Estimating grain-scale fluid effects on velocity dispersion in rocks: Geophysics, 56, 12, 1940–1949.

Mavko, G., and R. Nolen-Hoeksema, 1994, Estimating seismic velocities at ultrasonic frequencies in partially saturated rocks: Geophysics, 59, 2, 252–258.

Mavko, G., T. Mukerji, and J. Dvorkin, 2020, The rock physics handbook: Cambridge University Press.

McBride, E. F., 1989, Quartz cement in sandstones: a review: Earth-Science Reviews, 26, 1–3, 69–112.

Meng, Q., F. Hao, and J. Tian, 2021, Origins of non-tectonic fractures in shale: Earth-Science Reviews, 222, 103825.

Meunier, K. H., 2019, Reservoir Characterization of the Realgrunnen Subgroup in Wisting Central III (7324/8-3), SW Barents Sea: M.S. thesis, Norwegian University of Science and Technology.

Mindlin, R. D., 1949, Compliance of elastic bodies in contact: Journal of Applied Mechanics, 16, 259–268.

Müller, T. M., B. Gurevich, and M. Lebedev, 2010, Seismic wave attenuation and dispersion resulting from wave-induced flow in porous rocks—A review: Geophysics, 75, 5, 75A147–175A164.

Murphy, W. F., 1982, Effects of microstructure and pore fluids on the acoustic properties of granular sedimentary materials. Stanford University.

Nakajima, J., T. Matsuzawa, A. Hasegawa, and D. Zhao, 2001, Three-dimensional structure of Vp, Vs, and V_P/V_S beneath northeastern Japan: Implications for arc magmatism and fluids: Journal of Geophysical Research: Solid Earth, 106, B10, 21843-21857.

Narongsirikul, S., N. H. Mondol, and J. Jahren, 2019a, Acoustic and petrophysical properties of mechanically compacted overconsolidated sands: part 1–experimental results: Geophysical Prospecting, 67, 4, 804-824.

Narongsirikul, S., N. H. Mondol, and J. Jahren, 2019b, Acoustic and petrophysical properties of mechanically compacted overconsolidated sands: part 2–Rock physics modelling and applications: Geophysical Prospecting, 67, 1, 114–127.

Newman Jr, J, 1998, The merging of fatigue and fracture mechanics concepts: a historical perspective: Progress in Aerospace Sciences, 34, 5–6, 347–390.

Newman Jr, J. C., E. P., Phillips, and M. Swain, 1999, Fatigue-life prediction methodology using small-crack theory: International Journal of fatigue, 21, 2, 109–119.

Newnham, R. E., 2005, Properties of materials: anisotropy, symmetry, structure: Oxford University Press on Demand.

Nordgård Bolås, H. M., C. Hermanrud, and G. M. Teige, 2004, Origin of over-pressures in shales: Constraints from basin modeling: AAPG Bulletin, 88, 2, 193-211.

Norris, A., and D. Johnson, 1997, Nonlinear elasticity of granular media: Journal of Applied Mechanics, 64, 39–49.

Obradors-Prats, J., M. Rouainia, A. C. Aplin, and A. J. L. Crook, 2019, A diagenesis model for geomechanical simulations: Formulation and implications for pore pressure and development of geological structures: Journal of Geophysical Research: Solid Earth, 124, 5, 4452-4472.

Ohm, S. E., D. A. Karlsen, and T. Austin, 2008, Geochemically driven exploration models in uplifted areas: Examples from the Norwegian Barents Sea: AAPG Bulletin, 92, 9, 1191–1223.

Olierook, H. K., and N. E. Timms, 2016, Quantifying multiple Permian–Recent exhumation events during the break-up of eastern Gondwana: sonic transit time analysis of the central and southern Perth Basin: Basin Research, 28, 6, 796–826.

Osborne, M. J., and R. E. Swarbrick, 1997, Mechanisms for generating over-pressure in sedimentary basins: A reevaluation: AAPG Bulletin, 81, 6, 1023–1041.

Prasad, M., 2002, Acoustic measurements in unconsolidated sands at low effective pressure and overpressure detection: Geophysics, 67, 2, 405-412.

Pride, S. R., 2005, Relationships between seismic and hydrological properties: Hydrogeophysics, Springer, 253-290.

Queißer, M., and S. C. Singh, 2013, Full waveform inversion in the time lapse mode applied to CO_2 storage at Sleipner: Geophysical Prospecting, 61, 3,

537-555.

Ramm, M., 1992, Porosity-depth trends in reservoir sandstones: theoretical models related to Jurassic sandstones offshore Norway: Marine and Petroleum Geology, 9, 5, 553-567.

Ramm, M., A. W. Forsberg, and J. S. Jahren, 1997, Porosity–Depth Trends in Deeply Buried Upper Jurassic Reservoirs in the Norwegian Central Graben: An Example of Porosity Preservation Beneath the Normal Economic Basement by Grain-Coating Microquartz: AAPG Memoir, 69, 177-199.

Ramm, M., and K. Bjørlykke, 1994, Porosity/depth trends in reservoir sandstones: Assessing the quantitative effects of varying pore-pressure, temperature history and mineralogy, Norwegian Shelf data: Clay minerals, 29, 4, 475–490.

Rathore, J., E. Fjaer, R. Holt, and L. Renlie, 1995, P-and S-wave anisotropy of a synthetic sandstone with controlled crack geometry: Geophysical Prospecting, 43, 711–728.

Ravasi, M., and I. Vasconcelos, 2020, PyLops—A linear-operator Python library for scalable algebra and optimization: SoftwareX, 11, 100361.

Rider, M. H.,1986, The geological interpretation of well logs: Blackie and Son Limited.

Riis, F., and W. Fjeldskaar, 1992, On the magnitude of the Late Tertiary and Quaternary erosion and its significance for the uplift of Scandinavia and the Barents Sea, in R.M. Larsen, B. T. Larsen, H. Brekke, and E. Talleraas, eds., Structural and tectonic modelling and its application to petroleum geology: NPF Special Publication 1, 163–188.

Saenger, E. H., F. Enzmann, Y. Keehm, and H. Steeb, 2011, Digital rock physics: Effect of fluid viscosity on effective elastic properties: Journal of Applied

Geophysics, 74, 236–241.

Saul, M., and D. Lumley, 2015, The combined effects of pressure and cementation on 4D seismic data: Geophysics, 80, 2, WA135–WA148.

Scherbaum, F., 1982, Seismic velocities in sedimentary rocks—indicators of subsidence and uplift? Geologische Rundschau, 71, 2, 519–536.

Shapiro, S. A., 2003, Elastic piezosensitivity of porous and fractured rocks: Geophysics, 68, 2, 482–486.

Sharma, M. M., and A. N. Tutuncu, 1994, Grain contact adhesion hysteresis: A mechanism for attenuation of seismic waves: Geophysical Research Letters, 21, 21, 2323-2326.

Singh, S., R. K. Kandasami, T. G. Murthy, and M. R. Coop, 2023, On the modelling of stress-dilatancy behavior in weakly cemented sands: Soils and Foundations, 63, 4, 101328.

Sobolev, P., 2012, Cenozoic uplift and erosion of the Eastern Barents Sea-constraints from offshore well data and the implication for petroleum system modelling: Zeitschrift Der Deutschen Gesellschaft Fur Geowissenschaften, 163, 3, 309–324.

Storvoll, V., K. Bjørlykke, and N. H. Mondol, 2005, Velocity-depth trends in Mesozoic and Cenozoic sediments from the Norwegian Shelf: AAPG Bulletin, 89, 3, 359–381.

Suresh, S.,1998, Fatigue of materials: Cambridge University Press.

Tassone, D. R., S. P. Holford, I. R. Duddy, P. F. Green, and R. R. Hillis, 2014, Quantifying Cretaceous–Cenozoic exhumation in the Otway Basin, southeastern Australia, using sonic transit time data: Implications for conventional and unconventional hydrocarbon: AAPG Bulletin, 98, 1, 67–117.

Tatham, R. H., 1982, V_P/V_S and lithology: Geophysics, 47, 3, 336-344.

Tatham, R. H., and P. L. Stoffa, 1976, V p/V s; a potential hydrocarbon indicator: Geophysics, 41, 5, 837-849.

Tengattini, A., A. Das, G. D. Nguyen, G. Viggiani, S. A. Hall, and I. Einav, 2014, A thermomechanical constitutive model for cemented granular materials with quantifiable internal variables. Part I—Theory: Journal of the Mechanics and Physics of Solids, 70, 281–296.

Terzaghi, K., R. B. Peck, and G. Mesri, 1996, Soil mechanics in engineering practice, John Wiley & sons.

Thomsen, L., J. Castagna, and M. Backus, 1993, Weak anisotropic reflections: Offset-dependent reflectivity — Theory and practice of AVO analysis: Soc. Expl. Geophys, 103–111.

Thyberg, B., and J. Jahren, 2011, Quartz cementation in mudstones: sheet-like quartz cement from clay mineral reactions during burial: Petroleum Geoscience, 17, 1, 53–63.

Thyberg, B., J. Jahren, T. Winje, K. Bjørlykke, and J. I. Faleide, 2009, From mud to shale: Rock stiffening by micro-quartz cementation: First break, 27, 27–33.

Thyberg, B., J. Jahren, T. Winje, K. Bjørlykke, J. I. Faleide, and Ø. Marcussen, 2010, Quartz cementation in Late Cretaceous mudstones, northern North Sea: Changes in rock properties due to dissolution of smectite and precipitation of micro-quartz crystals: Marine and Petroleum Geology, 27, 8, 1752–1764.

Tillotson, P., J. Sothcott, A. I. Best, M. Chapman, and X. Y. Li, 2012, Experimental verification of the fracture density and shear-wave splitting relationship using synthetic silica cemented sandstones with a controlled fracture geome-

try: Geophysical Prospecting, 60, 3, 516-525.

Torset, S., R. M. Holt, and K. Duffaut, 2021, Integrating rock physics laboratory data and modelling to improve uplift characterization methodology: Geophysical Prospecting, 69, 3, 552–567.

Torset, S., and R. M. Holt, 2021, Stress-path-dependent effective medium model for granular media—Comparison with experimental data: Geophysics, 86, 1, MR39-MR52.

Torset, S., R. M. Holt, and K. Duffaut, 2021, Integrating rock physics laboratory data and modelling to improve uplift characterization methodology: Geophysical Prospecting, 69, 3, 552–567.

Trampert, J., P. Vacher, and N. Vlaar, 2001, Sensitivities of seismic velocities to temperature, pressure and composition in the lower mantle: Physics of the Earth and Planetary Interiors, 124, 3-4, 255-267.

Vernik, L., and J. Hamman, 2009, Stress sensitivity of sandstones and 4D applications: The Leading Edge, 28, 1, 90–93.

Virtanen, P., R. Gommers, T. E. Oliphant, M. Haberland, T. Reddy, D. Cournapeau, . . . J. Bright, 2020, SciPy 1.0: fundamental algorithms for scientific computing in Python: Nature methods, 17, no 3, 261–272.

Walderhaug, O., 1996, Kinetic modeling of quartz cementation and porosity loss in deeply buried sandstone reservoirs: AAPG Bulletin, 80, 5, 731–745.

Walton, K., 1987, The effective elastic moduli of a random packing of spheres: Journal of the Mechanics and Physics of Solids, 35, 2, 213–226.

Wang, H., W. Xu, M. Cai, Z. Xiang, and Q. Kong, 2017a, Gas permeability and porosity evolution of a porous sandstone under repeated loading and unload-

ing conditions: Rock Mechanics and Rock Engineering, 50, 8, 2071–2083.

Wang, W., V. Nardelli, and M. R. Coop, 2017b, Micro-mechanical behaviour of artificially cemented sands under compression and shear: Géotechnique Letters, 7, 3, 218-224.

Wang, Y., and S. Leung, 2008, Characterization of cemented sand by experimental and numerical investigations: Journal of geotechnical and geoenvironmental engineering, 134, 7, 992–1004.

Wang, Z., 2001, Y2K tutorial: Fundamentals of seismic rock physics: Geophysics, 66, 398–412.

Wang, Z., and A. M. Nur, 1989, Effects of CO_2 flooding on wave velocities in rocks with hydrocarbons: SPE Reservoir Engineering, 4, 429–436.

Weinzierl, W., and B. Wiese, 2021, Deep learning a poroelastic rock-physics model for pressure and saturation discrimination: Geophysics, 86, 1, MR53–MR66.

Wensaas, L., H. Shaw, K. Gibbons, P. Aagaard, and H. Dypvik, 1994, Nature and causes of overpressuring in mudrocks of the Gullfaks area, North Sea: Clay minerals, 29, 4, 439-449.

Winkler, K. W., 1983, Contact stiffness in granular porous materials: comparison between theory and experiment: Geophysical Research Letters, 10, 11, 1073–1076.

Worden, R. H., and S. D. Burley, 2003, Sandstone diagenesis: the evolution of sand to stone. Sandstone diagenesis: Recent and ancient, 1-44.

Xu, H., 2006, Calculation of CO_2 acoustic properties using Batzle-Wang equations: Geophysics, 71, F21–F23.

Yilmaz, Ö., 2001, Seismic data analysis: Processing, inversion, and interpretation

of seismic data: Society of Exploration Geophysicists.

Yin, H., 1992. Acoustic velocity and attenuation of rocks: Isotropy, intrinsic anisotropy, and stress induced anisotropy, PhD dissertation, Stanford University.

Yin, H., and J. Dvorkin, 1994, Strength of cemented grains: Geophysical Research Letters, 21, 10, 903–906.

Yu, J., K. Duffaut, and P. Avseth, 2023a, Stress sensitivity of elastic moduli in high porosity cemented sandstone — heuristic models and experimental data: Geophysics, 88, 4, 1-54.

Yu, J., K. Duffaut, and P. Avseth, 2023b, Understanding the synergistic impact of stress release and cementation on sandstone using sound waves-implications for exhumation estimation. Geophysics, 88, 6, 1-87.

Zattin, M., B. Andreucci, B. de Toffoli, D. Grigo, and F. Tsikalas, 2016, Thermochronological constraints to late Cenozoic exhumation of the Barents Sea Shelf: Marine and Petroleum Geology, 73, 97–104.

Zhang, L., J. Ba, and J. M. Carcione, 2021, Wave propagation in infinituple-porosity media: Journal of Geophysical Research: Solid Earth, 126, 4, e2020JB021266.

Zhang, L., J. Ba, J. M. Carcione, and C. Wu, 2022, Seismic wave propagation in partially saturated rocks with a fractal distribution of fluid-patch size: Journal of Geophysical Research: Solid Earth, 127, 2, e2021JB023809.

Zimmer, M. A., 2004, Seismic velocities in unconsolidated sands: Measurements of pressure, sorting, and compaction effects. Stanford University.

NTNU

Norwegian University of
Science and Technology